Alma Mater Studiorum - Università di Bologna

SCUOLA DI SCIENZE

Dipartimento di Chimica Industriale “Toso Montanari”

Corso di Laurea Magistrale in

Chimica Industriale

Classe LM-71 - Scienze e Tecnologie della Chimica Industriale

Synthesis and characterisation of electrospun gold on ceria catalysts

Tesi di laurea sperimentale

CANDIDATO

Filippo Ballarini

RELATORE

Chiar.ma Prof.ssa Stefania Albonetti

CORRELATORE

Dott. Alessandro Allegri

Dott. Emanuele Maccaferri

Chiar.ma Prof.ssa Laura Mazzocchetti

Anno Accademico 2019-2020

Abstract

Cerium oxide in catalysis can be used both as support and as a catalyst itself. Ceria catalyses many oxidations reactions, its excellent catalytic properties are due to its store oxygen storage capacity (OSC) and the reticular defects present on its surface. Different morphologies expose different reticular planes, and different reticular planes can expose different amounts of defects. The preparation method of cerium oxide can influence the surface area, morphology, and the number of defects in the sample. This work is focused on different preparation methods for gold nanoparticles supported on 1D nanostructures of cerium oxide prepared via electrospinning, their XRD, DRUV-Vis and Raman characterizations, and their catalytic performance on the oxidation reaction of HMF to FDCA.

Keywords
Valorisation of biomass
Catalytic oxidation of HMF
Supported Au nanoparticles
Cerium oxide
Electrospinning
Nanocomposites

Summary

1 Research purpose

Sustainable chemistry aims to minimise the environmental impact of processes, reducing waste production, avoiding the use of hazardous substances, and exploiting renewable sources.[1,2]

The use of biomasses has gained increasing interest due to their abundance and ubiquity combined with the fact that they can be converted into a wide variety of products, from fuels to platform molecules for the synthesis of chemical products. Several platform molecules derived from renewable sources have now been identified. Among these, 5-hydroxymethylfurfural (HMF), belonging to the furan family, was of great interest. In 2004, the U.S. Department of Energy identified 5- hydroxymethylfurfural (HMF) as one of the top ten key platforms molecules. Industrially speaking, HMF nowadays is produced in modest quantity, but its production is expected to rise in the next years.[1,3–5]

HMF can be obtained by dehydration of hexose sugars and has a high industrial interest; it is considered an important intermediate for the synthesis of a wide variety of alternative fuels and products, such as drugs, fungicides, polymers and molecules such as levulinic acid and 2,5-furandicarboxylic acid (FDCA), a possible substitute for terephthalic acid in plastic production.[6,7]

FDCA can be produced by oxidation of HMF but the processes currently used involve the use of homogeneous and heterogeneous catalysts under high pressure or temperature conditions.

Cerium oxide is an interesting material for catalyst production for its availability, its excellent catalytic properties are given by the interaction with the defective structure of its surface and its store oxygen capacity (OSC). Different morphologies expose different reticular planes, and different reticular planes can expose different amounts of defects. The preparation method of cerium oxide can influence the surface area, morphology, and the number of defects in the sample. In particular, ceria nanostructures with high aspect-ratio seem to have high activity capabilities.[8–12]This research aims to synthesize, characterise, and test on the oxidation of HMF to FDCA a range of gold nanoparticles supported on electrospun ceria nanofibers catalysts, to investigate the link between the preparation method, the obtained morphology, and the activity of the catalysts. In order to assess the catalytic properties of gold on ceria systems, different gold-based catalysts were prepared starting from different supports: commercial ceria powders, electro-spun ceria nanofibers with and without gold precursors and undergoing different thermal treatments (pyrolysis and calcination).

2 Introduction

In 2009 the United Nations Framework Convention on Climate Change in Copenhagen, Denmark, has ratified the Kyoto Protocol and is intended to reduce global emissions by 50% by 2050, comparing it to the relative emission level in 2006. Is also estimated that around 20% of CO_2 emissions are released from the chemical manufacture sector, one possible solution to this concern is to use non-edible biomass crops to produce biochemicals, especially those which exists in the form of non-food lignocellulosic materials such as grasses, woods (hard and soft), and crop residues (corn stover, wheat straw, sugar cane, bagasse, etc.), serves as renewable feedstock and could be considered as an alternative source of the chemicals and energy currently derived from petroleum.[13–16] Biomasses are a promising way to produce energy and chemicals from renewable resources, however, there are many concerns about the exploitation of lands and fields instead of using them for the production of food crops. HMF is considered a carbon-neutral feedstock for the production of fuels and other chemicals. In 2004, the U.S. Department of Energy identified 5- hydroxymethylfurfural (HMF) as a key platform chemical that can be the precursor to both chemical feedstocks and potential fuels, such as 2,5-dimethylfuran (40% higher energy density than ethanol). [3,15,17,18]

2,5-Hydroxymethylfurfural (HMF, shown in Figure 1), is an aromatic compound made out of a furan ring with both the aldehyde and the alcohol functional groups in positions 2 and 5. It was first discovered in 1875 as an intermediate product of the levulinic acid (LA) production from glucose. HMF is known in everyday life as a food improvement agent[19], it contributes to the smell of tomatoes, onions, and tobacco. HMF is also produced throughout food cooking or during food stocking[5,19,20], in fact, is used as an indicator of cooking grade, honey quality, or wine and grapes syrup stocking conditions. Industrially speaking, HMF nowadays is produced in modest quantity, but its production is expected to rise in the next years.[1,5]

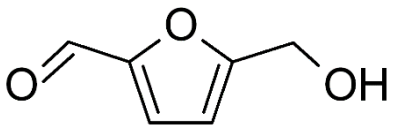

Figure 1: Structure of HM

1.1.1 *Synthesis of HMF*

HMF is produced from oligosaccharides, polysaccharides, and hexoses sugars (especially fructose and glucose, Figure 2) via three dehydration reactions. The complete synthetic route is not simple and presents many side reactions, such as the formation of insoluble humic acids or further degradation of HMF to levulinic acid (LA)/formic acid (FA) mixtures. These reactions create a lot of issue for HMF yield.[17]

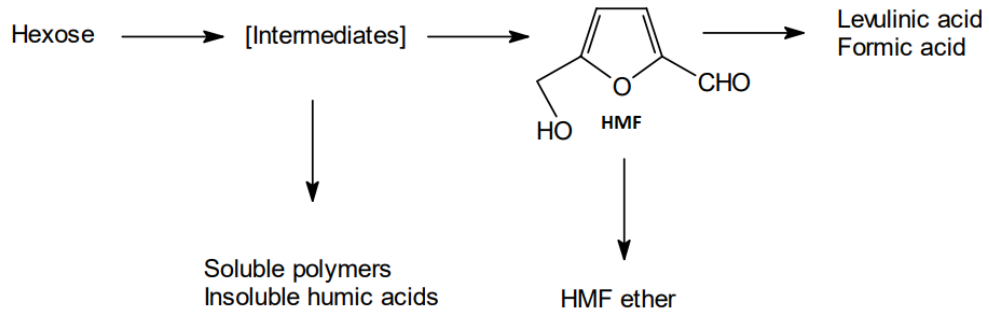

Figure 2: simple scheme of the production of HMF from sugars [17]

Since the 1980s research in the development of efficient methods for HMF production from carbohydrates were almost exclusively focused on the aqueous-based mineral acid-catalysed system. Various studies demonstrated the positive effect of organic solvents (e.g. sulfolane, DMF and ethers) on HMF yield;[15,17] one of the best results was obtained by Mercadier et al. and consisted of a 90% yield in DMF with resin Diaion PK-216 or 70% yield form glucose and polysaccharides in immonium and ammonium salts (also called ionic liquids). [16,21]

Biphasic systems have been tested during the 21st century too, in order to reduce the various selectivity or conversion issues of monophasic aqueous systems, but they suffer from scalability problems, due to the use of water and high boiling point aprotic solvents, including ionic liquids. The isolation of HMF from these solvents requires a large amount of organic solvent for the extraction and the lack of knowledge about solvent and catalyst recycling do not make the biphasic system ready for industrial-scale production yet. [1]

1.1.1.1 The mechanism of the fructose dehydration

Two different paths have been hypothesized to produce HMF (Figure 3) from dehydration of hexoses sugars, especially fructose and glucose:[17]

- Path "a" includes transformation of ring systems.
- Path "b" is an acyclic route.

The scientific evidence confirmed path "a" as the correct one,[22] because:

- The easier formation of HMF from fructose or a fructose part of sucrose.
- 2,5-Anhydro-D-mannose converts easily into HMF.
- When the reaction was carried out in D_2O starting from fructose, deuterium was absent in HMF. If 3-deoxyglycosulose (Figure 3, molecule "3") was formed during the reaction, one should expect a carbon-deuterium bond due to the keto-enol tautomerism (Figure 3, molecule "2").

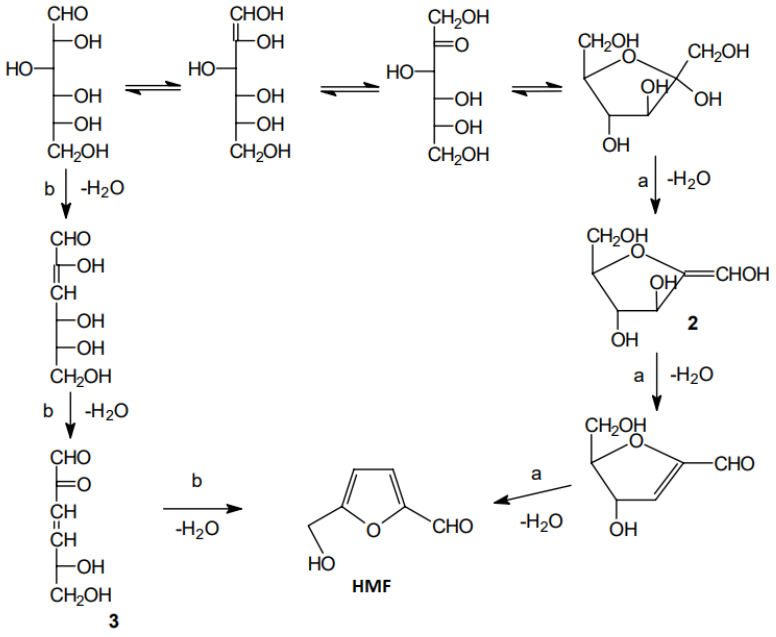

Figure 3: mechanisms for the fructose dehydration to HMF[17]

1.1.2 *Reactions on HMF and possible uses*

HMF is receiving increasing interest thanks to its possible applications as a platform molecule to produce products usually obtained from oil. HMF could be converted into a variety of compounds that will be used both as biopolymer precursors, biofuels and product with low environmental impact[7] (as shown in Figure 4). Some of these substances are:

- Caprolactam (Nylon 6 production)[23]
- Caprolactone (PCL production)[23]
- 1,6-Hexanediol (biomonomer)[24]
- Adipic acid (biomonomer)[25]
- 2-5 Dimethylfuran (biofuel)[26]
- 2,5-furandicarboxylic acid or "FDCA" (biomonomer for biopolyesters)[17,27–29]
- Levulinic Acid (chemical precursor)[30]
- 2,5-Furandimethanol "DHMF" (biomonomer and chemical for crown ethers)[7]
- Tetrahydro-2,5-furandimethanol "DHMTHF" (biomonomer, solvent)[6]

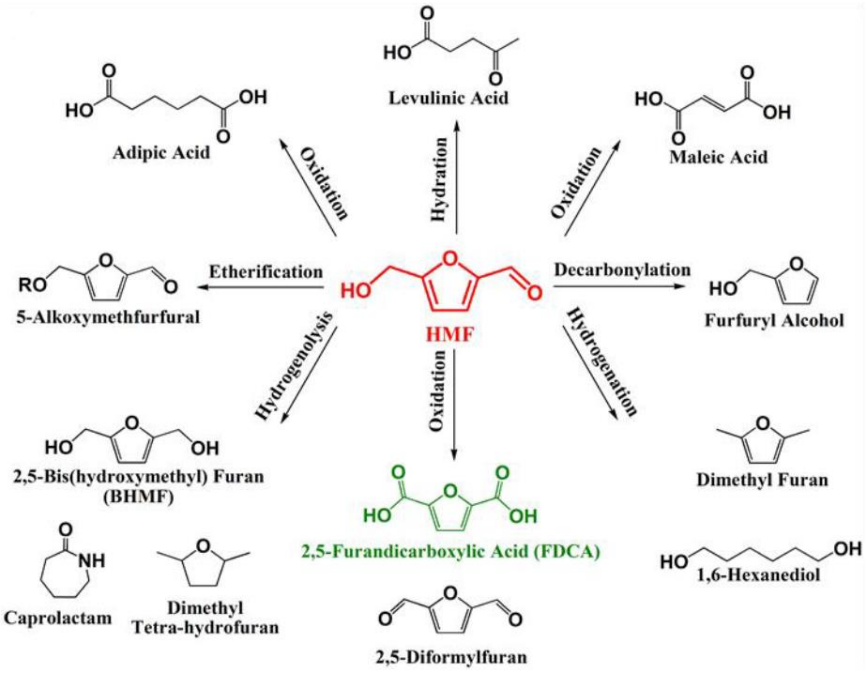

Figure 4: possible products from HMF reactions [29]

1.1.2.1 2,5-furandicarboxylic acid (FDCA)

2,5-furandicarboxylic acid (FDCA) cloud be used as a biobased monomer for polyester such as PEF (Polyethylene Furanoate), a polyester in which the petrochemical-derived terephthalic acid is substituted by FDCA.[17,29]

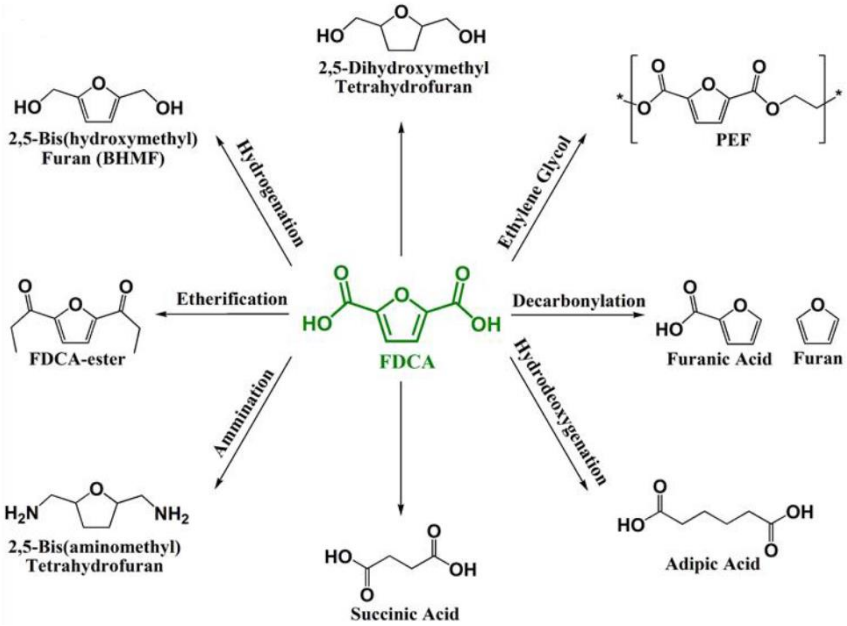

Figure 5: possible products from FDCA reactions[29]

The synthesis of HMF into FDCA is divided into two steps: aldehyde oxidation and alcohol oxidation, it proceeds for two different pathways (Figure 6), forming 2,5-diformylfuran (DFF) and 5-hydroxymethyl-2-furan carboxylic acid (HMFCA), only HMFCA seems to be detected in the literature tests in alkaline solutions, because the first group to be oxidised is the carboxylic group. [31,32] The intermediate is then further oxidized to 5-formyl-2-furancarboxylic acid (FFCA), which is finally transformed to FDCA. [29,33]

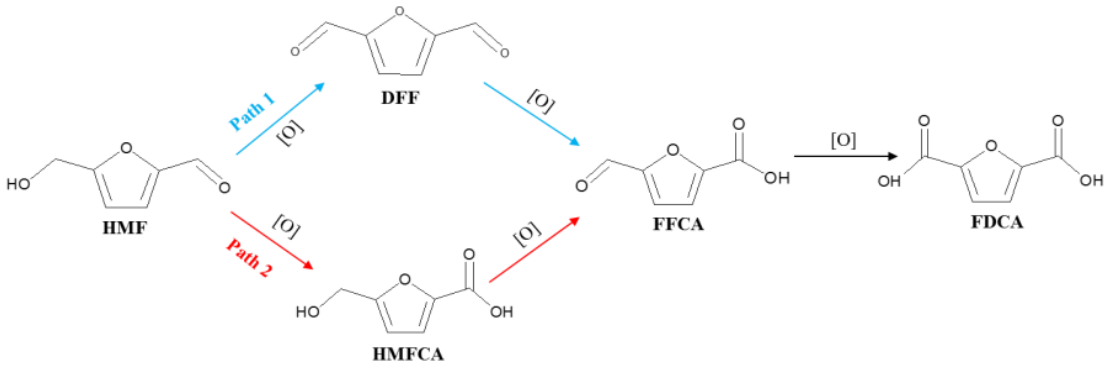

Figure 6: two possible reaction pathways for the oxidation of HMF to FDCA [29]

1.1.2.2 Levulinic acid (LA)

HMF is an intermediate product in the production of levulinic acid (LA) from sugar (Figure 7). LA is an interesting chemical precursor, it could be used in the synthesis of high-value product as solvents, biofuels, and biopolymers such as γ-Valerolactone (GVL), Methyl acrylate, succinic acid or diphenolic acid. [34,35]

The GVL is particularly interesting because it presents several applications:

- It is a non-toxic, degradable solvent and cheap industrial solvent.[36]
- It could be used as biofuel as it is or transformed in valeric esters, to produce both gasoline and diesel fuel (via tuning the alkyl chain of the ester, Figure 8) or alkenes.[37,38]
- It could produce biopolymers via reaction with amines as ammonia, ethanolamine, ethylenediamine or piperazine.[39]

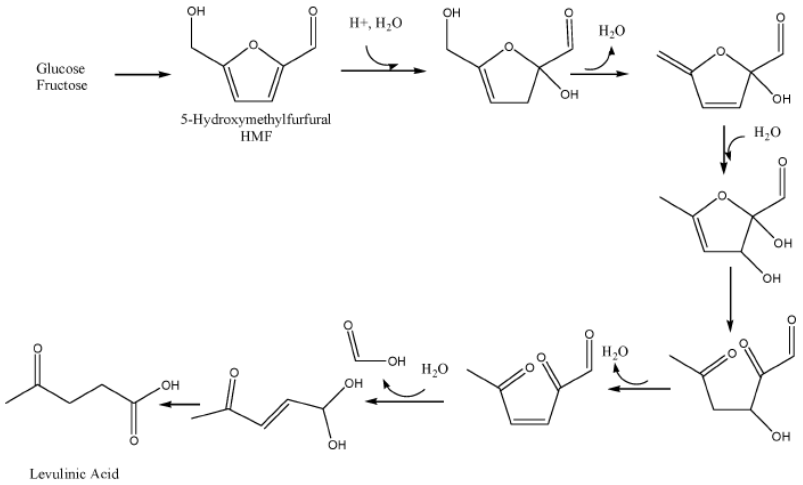

Figure 7: reaction route from HMF to LA [40]

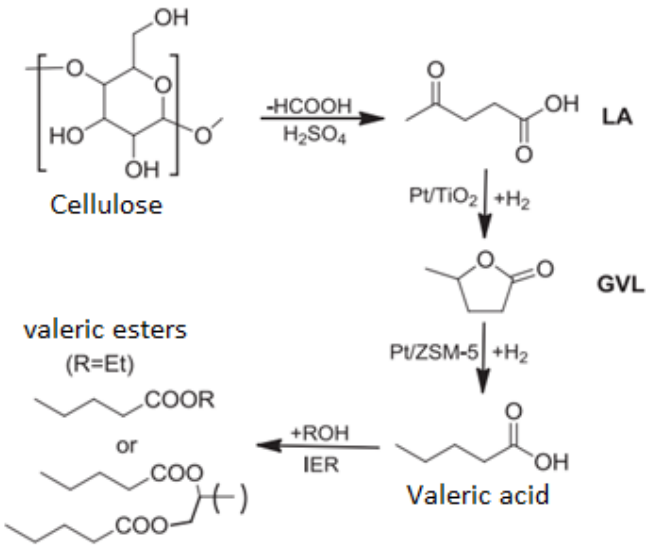

Figure 8: reaction route from cellulose to LA, GVL and valeric esters

1.1.2.3 2,5-dimethylfuran (DMF)

2,5-dimethylfuran (DMF) could be considered a good biofuel in alternative to conventional petrol-based gasoline, its calorific power (33,7 MJ/kg) is higher than the one of ethanol (26,9 MJ/kg) and comparable with gasoline (43,2 MJ/kg). DMF has a research octane number (RON) of 119 and a stoichiometric air/fuel ratio that is 33% less than standard gasoline (10,72 compared to 14,56), its thermal efficiency is considered comparable to gasoline. [18]

DMF is also used as a scavenger for singlet oxygen molecules and is used in its determination procedure in waters.[41] The reactions mechanism involves first a Diels-Alder and then an hydrolysis that gives diacetylethylene and hydrogen peroxide as final products.

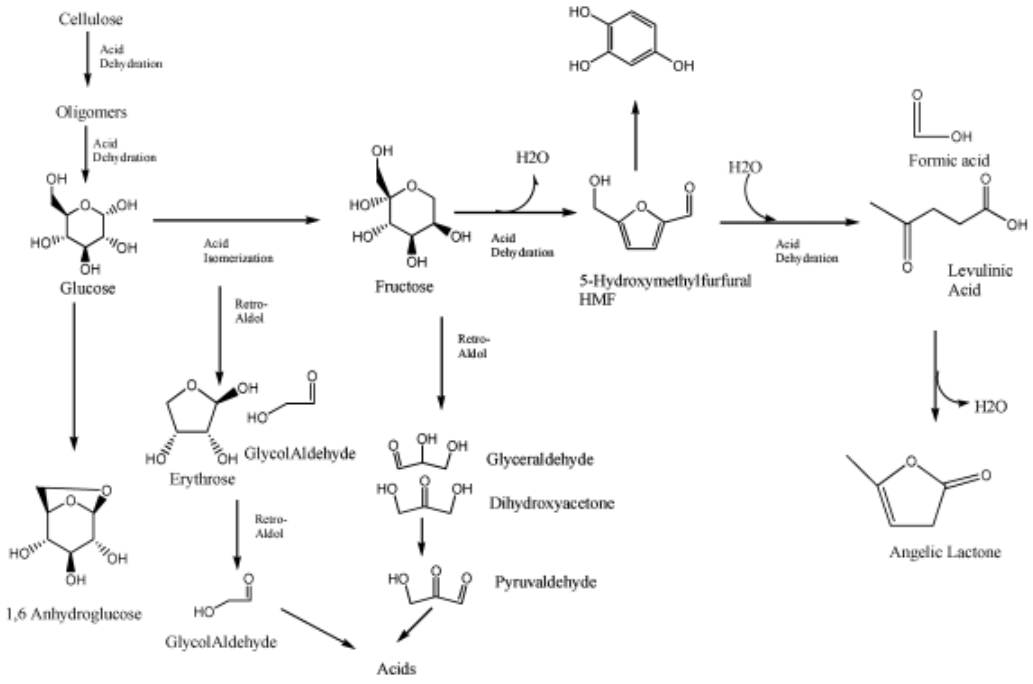

Figure 9: Cellulose decomposition pathways in supercritical water[40]

1.2 Oxidation of HMF with heterogeneous catalysts in the scientific literature

There are various choices to make to carry out the oxidation of HMF both in a laboratory and on an industrial scale:

- The type of catalyst
- Systems to recover the catalyst and products
- The metal for the active phase
- The support
- The oxidant
- pH

During the last decades, various systems have been tested for this reaction: heterogeneous catalysts, homogeneous catalysts, biocatalysts, electrochemical processes, and photocatalytic processes in both aqueous and biphasic systems. Heterogeneous catalysts are the most interesting, due to their stability and recyclability. Noble metals as Pt, Pd, Au, Ru have been reported in the literature for the oxidation of HMF.[29,42]

1.2.1 *The choice of the oxidant*

Different oxidants have also been tested for HMF oxidation such as oxygen, air, H_2O_2, and $KMnO_4$. Obviously, oxygen and air are often preferred because they are more available, cheaper, and environmentally friendly.[29,43]

1.2.2 *Au-based oxidation catalysts*

The choice of support for Au-based catalysts have a great impact on the reaction's performance in HMF oxidation to FDCA. E.g., using TiO_2 and CeO_2 as supports, Au-based catalysts showed nearly quantitative FDCA yields (yield of 99% at 65°C, 10 bar of air, reaction time of 8 h), in contrast, Au supported on carbon and Fe_2O_3 only reaches FDCA yields of 44% and 15% (under the same conditions) respectively.[29]

As shown in Figure 10, HMF has been first fast oxidized to HMFCA via the formation of a hemiacetal-1 intermediate. Being that no FFCA has been directly observed, the hypothesis is that it has been formed via oxidation of HMFCA, and then FFCA has been quickly transformed into FDCA through the production of a second intermediate product, hemiacetal 2. The rate-determining reaction step is the oxidation of HMFCA into FDCA. [29,32]

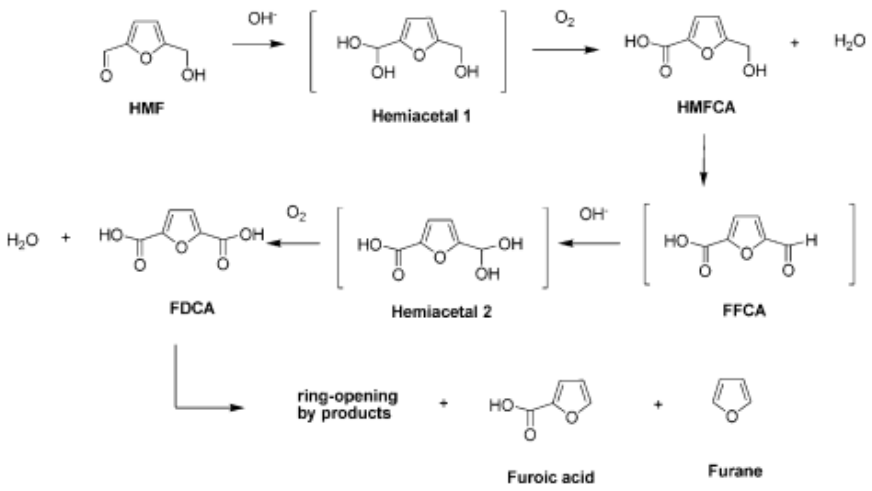

Figure 10: Oxidation pathway from HMF to FDCA, with possible intermediates and by-products[32]

Reductive pre-treatment of Au/CeO_2 has shown to increase the catalytic activity due to an increased amount of Ce^{3+} and oxygen vacancies for the hydride transferring and the O_2 activation during the oxidation of the alcohol group[29], in particular:

- The Lewis acid sites of Ce^{3+} and Au^{+} species of Au/CeO_2 could accept a hydride from the C–H bond in alcohol or in the corresponding alkoxide to form Ce–H and Au–H, with the formation of a carbonyl species.[31]
- The oxygen vacancies of CeO_2 can activate O_2 and form cerium-coordinated superoxide (Ce–OO) species, which evolves into cerium hydroperoxide by abstraction of hydrogen from Au-H. Cerium hydroperoxide then interacts with Ce–H, producing H_2O and recovering Ce^{3+} centres. Au–H donates H and changed back to the initial Au^{+} species.[44]

1.2.2.1 Reaction oxidation pathway in basic aqueous solution with Au or Pd catalyst

The reaction mechanism of the oxidation has been described by Davis et al. trough isotopic labelling, and it has been carried out in aqueous solution with molecular oxygen, Au catalyst (Au/TiO_2) and a base (NaOH). [44,45]

The aldehyde of HMF reacts via rapidly reversible hydration to a geminal diol through nucleophilic addition of a hydroxide ion to the carbonyl followed by proton transfer from water to the alkoxy ion intermediate (step 1, Figure 11), this step was proved thanks to the incorporation of two ^{18}O atoms in HMFCA when the reaction was performed in $H_2{}^{18}O$.

The second step is the dehydrogenation of the geminal diol intermediate, facilitated by the hydroxide ions adsorbed on the metal surface, to form the carboxylic acid HMFCA (step 2 Figure 11). The next step is the oxidation of the alcoholic group of HMFCA to produce FDCA. The base deprotonates the alcoholic group to form an alkoxy intermediate in solution. [46]

Hydroxide ions on the catalyst surface then facilitate the activation of the C–H bond in the alcoholic group to form the aldehyde 5-formyl-2-furancarboxylic acid (FFCA) (Step 3, Figure 11). The next two steps (steps 4 and 5, Figure 11) oxidize the aldehyde function of FFCA to form FDCA. These two steps are expected to proceed similarly to steps 1 and 2 for the oxidation of HMF to HFCA.

The reversible hydration of the aldehyde group (step 4, Figure 11) to a geminal diol incorporates two more ^{18}O atoms in FDCA, which means that the overall oxidation reaction of HMF in FDCA uses water as source of oxygen atoms, instead of the easily available molecular O_2, probably because of the participation of hydroxide in the catalytic process. Nevertheless, molecular oxygen was essential during oxidation by removing electrons deposited into the supported metal particles. [45]

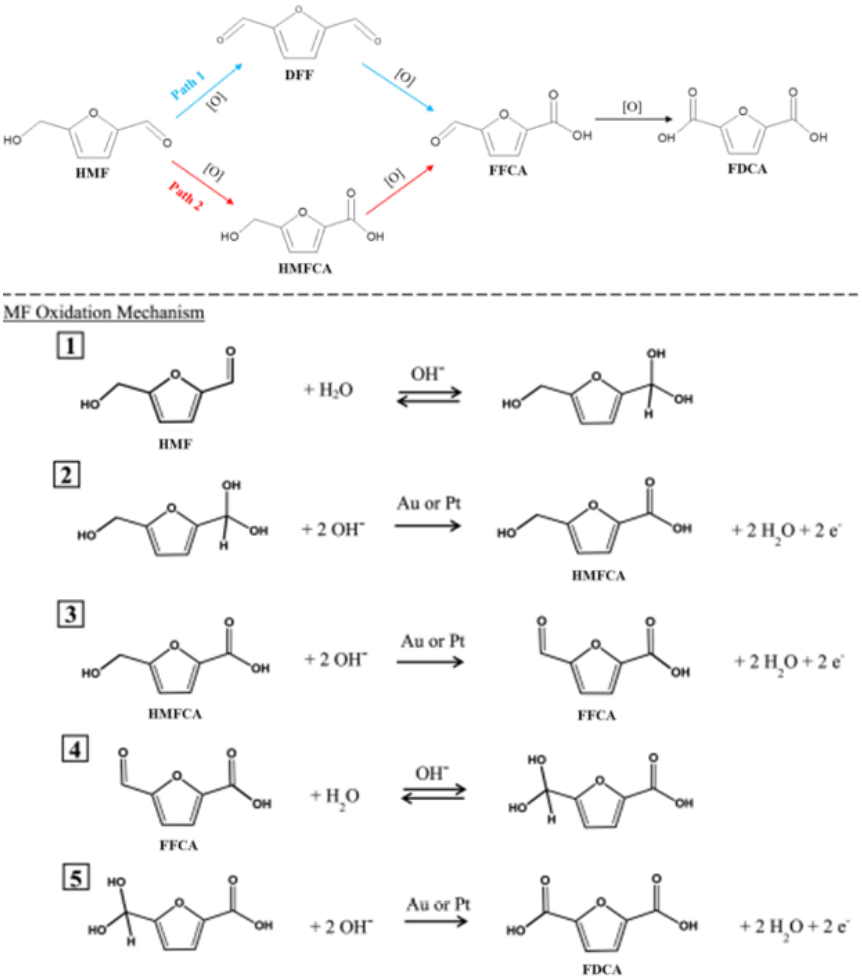

Figure 11: mechanism of HMF oxidation to FDCA in alkaline solution[45]

1.2.2.2 HMF oxidation over Au-based bimetallic catalysts

Various Au-based bimetallic catalyst shown also better properties than the corresponding monometallic catalyst. Au-Cu/TiO_2 catalysts prepared via colloidal solution showed an activity greater of two factors than the monometallic AU/TiO_2 catalyst, they presents also 100% HMF conversion and 99% FDCA yield under mild reaction conditions (10bar O_2, 4 equiv. NaOH, 95°C), good properties even under several uses, due to its resistance to poisoning and to leaching or agglomeration of Au nanoparticles.[28]

Another interesting bimetallic catalyst is Au-Pd/AC. The catalysts, with molar ratio Au:Pd of 8:2 on carbon support[47], shown significantly increased stability and activity even after several runs, compared to the monometallic Au/Pd/AC that has only a yield of 20% after 5 runs.

1.2.2.3 Base-free HMF oxidation over Au-based catalysts

Aerobic oxidation of HMF is conducted in the presence of base excess [29]but, for obvious economic and environmental reasons, base-free processes are very interesting. Au-based hydrotalcite supported catalyst (Au/HT) has been tested[48] without the base in mild aqueous conditions (95°C, P_{O2}= 1 bar, t=7 h), with a yield of 99% in FDCA. The Au deposited on other neutral or acidic supports (SiO_2) shown a low activity, as expected because of the lack of basic sites. However, even with Au on basic support as MgO gave an FDCA yield of 21%; the TEM analysis revealed larger Au nanoparticles on MgO (> 10 nm) than on HT hydrotalcite (3,2nm) this could be the main reason for the lower activity of the Au/MgO catalyst.

The catalysts Au/HT have been reinforced against leaching by Gao et al., the catalyst is supported on hydrotalcite and activated carbon (Au/HT-AC)[49]. This support is more resistant to Mg^{2+} leaching than Au/HT,[50] but needs for a longer reaction time to reach the complete conversion, its catalytic activity (FDCA Yield = 99.5%, T=100 °C, 5 bar O_2, t=12 h) comes from the availability of basic sites, its large surface area and the presence of hydroxyl and carbonyl groups on its surface.

Au-Pd alloys have been developed as a base free catalyst too, they have been supported on carbon nanotubes[49], NiO[51] and layered double hydroxide CaMgAl doped with La[52]. They show almost 100% yield in FDCA but need high oxygen pressure and high reaction time.

1.3 Cerium(IV) oxide

Cerium (IV) oxide or "ceria" is the oxide with the chemical formula: CeO_2. It is a metal oxide of great interest, due to its intrinsic oxygen storage capacity (OSC), the interactions with the defective structure on the surface, and the relative abundance of Cerium in the earth crust, comparable to copper and higher than the one of lead and tin.[8,53,54] CeO_2 is used in the automotive field to convert the exhaust gasses, like oxygen sensors, in membranes as a component in the fuel cells, in industrial chemical processes as catalyst support for water-gas shift and steam reforming or as catalyst itself. [55,56]

The crystal structure of cerium oxide is a face-centred cubic (fcc) fluorite type (Figure 12), the lattice is made of cerium cation, the interstitial octahedral sites are occupied by oxygen anions, each cerium cation is then coordinated by eight oxygen anions, while each oxygen by four cerium cations[11,53].

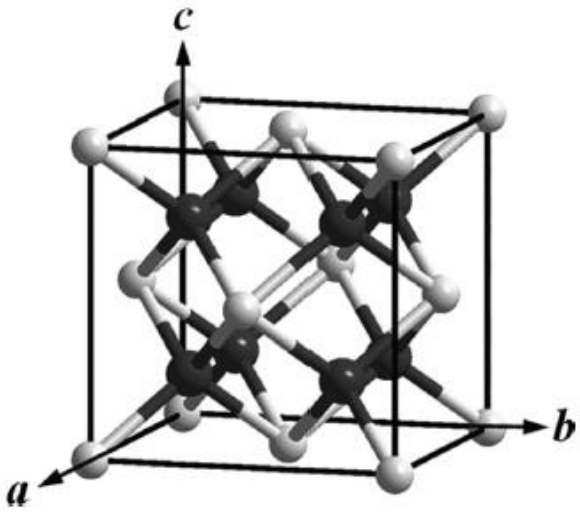

Figure 12: scheme of fcc structure of ceria[57]

The properties of ceria came from its ability to reversibly release oxygen atoms transferring two electrons[58] to two cerium +4 atoms and reducing them to cerium +3 atoms, forming a defective structure with chemical formula $CeO_{(2-x)}$ ($0<x<0.5$). The colour of the stoichiometric CeO_2 is pale yellow due to the charge transfer Ce(IV)–O(II), otherwise, the more defective $CeO_{(2-x)}$ structure has a dark blue or even black colour. In extremely reducing conditions cerium (IV) oxide can be transformed into cerium(III) oxide (chemical formula: Ce_2O_3)[53], with a complete changing in the crystalline structure from fcc to hexagonal sesquioxide, which is not stable in air and it slowly oxidised back to CeO_2.[59]

The different defects present in ceria structure could be differentiated between intrinsic and extrinsic. Intrinsic defects are disorders in the structure induced both thermally or by interaction with the surrounding atmosphere. Extrinsic defects are given by doping agents or impurities in the structure. [57,60–62]

The main types of intrinsic point defects in the lattice are Frenkel, oxygen vacancy, Schottky, and interstitial defects (Figure 13)[57,63]. These types of defects involve different atoms arrangements to maintain the charge balance in the structure: Frenkel defects are vacancies in the structure generated by oxygen ions of the lattice that moved from their positions to interstitial sites, this do not change the overall charge and stoichiometry of the lattice. In the oxygen vacancy defect, an oxygen ion is removed from its lattice positions, hence creating a vacant site and to maintain the charge balance in the lattice, two Ce(IV) ions reduce to Ce(III) ions. Schottky types are vacancies in the lattice structure of both cations and anions in stoichiometry amounts. The interstitial defect is the presence of two oxygens anions and one cerium cation in the interstitial sites that leaves three total vacancies in the lattice structure.

The predominant defects observed in reduced ceria are anion Frenkel pairs and oxygen anion vacancies and are outlined below respectively using the Kröger - Vink notation:

$$O_O^X + 2Ce_{Ce}^X \rightarrow V_O + 2Ce'_{Ce} + \frac{1}{2}O_{2(g)}$$

$$O_O^X \leftrightarrow O_i'' + V_{\ddot{O}}$$

In the Kröger - Vink notation O_O^X and O_i'' indicates oxygen ions in the lattice and in the interstitial position respectively, V_O indicates an oxygen vacancy created at the lattice site. Ce_{Ce}^X is a cerium ion in its lattice position and Ce'_{Ce} is a Cerium (III) atom.

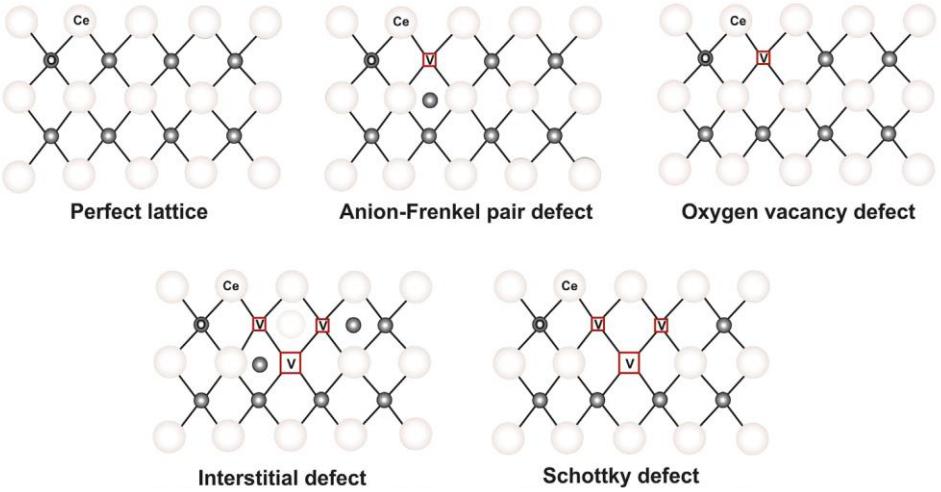

Figure 13: Possible types of point defects in CeO2 lattice. Key: Oxygen=dark grey circles, cerium= white circles, and vacant site=red square with "V."

The fact that the oxygen atoms lie on the same crystal plane allows them to spread as quickly as greater the number of vacancies present in the structure.[57] The main low-Miller index planes are: (100), (110) and (111). Different nanostructures preferentially expose different faces, such as simple nanoparticles of ceria shaped as octahedra with broken off edges preferentially expose the face (111), the nano-cubes preferentially show the plane (100) (Figure 14), while nanorods tend to expose the planes (110) and (100). The particularity of the plans (110) and (100) is the higher number of vacancies given by their lower formation energy compared to the plane (111)[11]. Sudipta et al. have measured the content of defects in different ceria nanostructures and it was found to follow the order nanorod > nanocubes > nano polyhedra. [64,65]

The high reactivity given by the vacancies combined with the high aspect ratio structures can be exploited for the production of catalysts. However, in the case of catalysts supported on ceria, one must not only take into account the number of vacancies present on the support, but he has also to consider how the morphology influences both the dispersion of the metal and the metal-support interactions. [66,10,67,68,65]

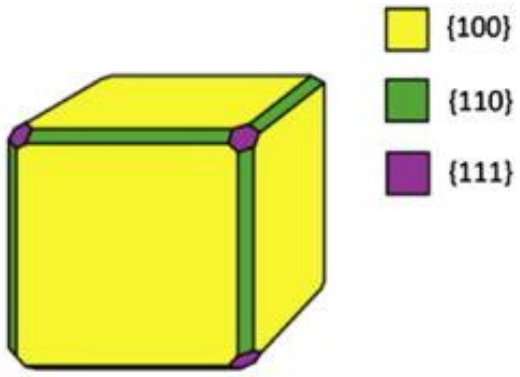

Figure 14: exposed faces in a non-ideal ceria nanocube

1.3.1 *Types of nanostructures*

The various ceria nanostructures are differentiated according to their aspect ratio.

Zero dimensions (0D) structures have similar dimensions in the three spatial directions, an example of these structures are octahedral nano, nano-spheres, and nano-cubes (Figure 15). The lowest energy structure is the octahedral one. Both octahedra and cubes often take truncated forms on both corners and edges. That is why ideal nanostructures, such as nanocubes, should only have plans (100), but experimentally there are both plans (110) and (111) (Figure 16). [10]

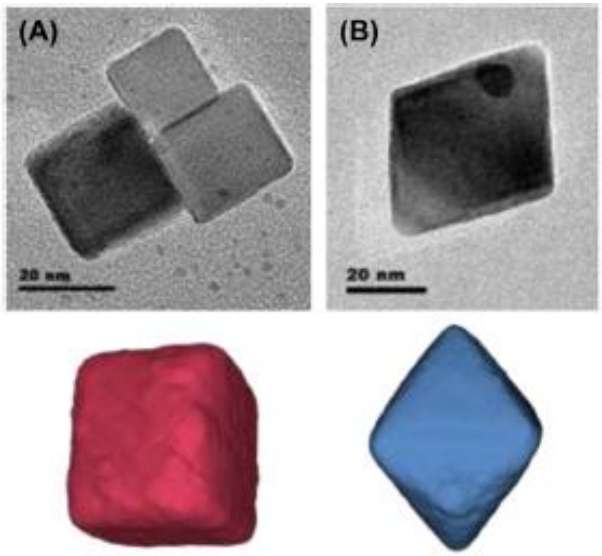

Figure 15: TEM images and corresponding 3D model of the nanocube (A) and nano octahedron (B)[69]

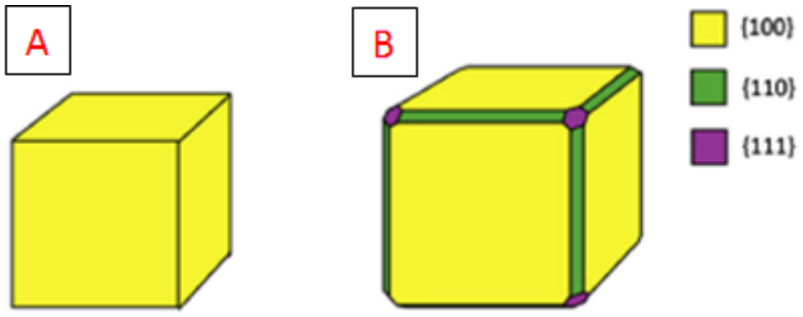

Figure 16: simplified models of an ideal nanocube (A) and real nanocube (B) with the crystal planes exposed[69]

One dimension (1D) structures are particularly elongated in one spatial dimension; these structures have a high length-diameter ratio. The 1D category includes nanorods (Figure 17), nanotubes, wire-in-nanotubes, nanobelts, and nanofibres (Figure 18).

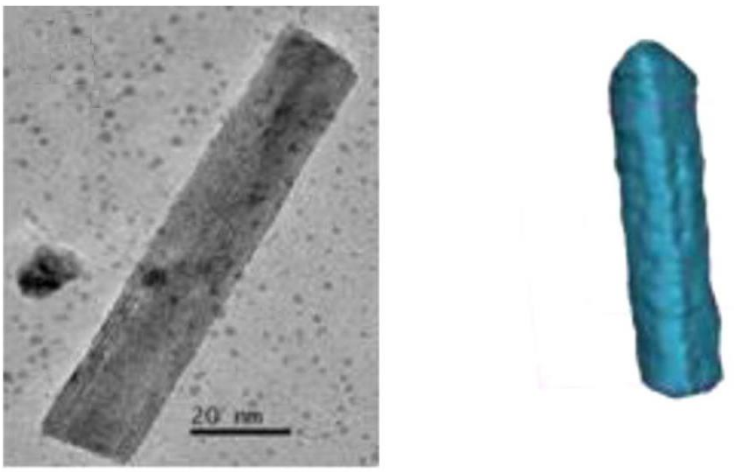

Figure 17: TEM images and a 3D model of a nanorod[69]

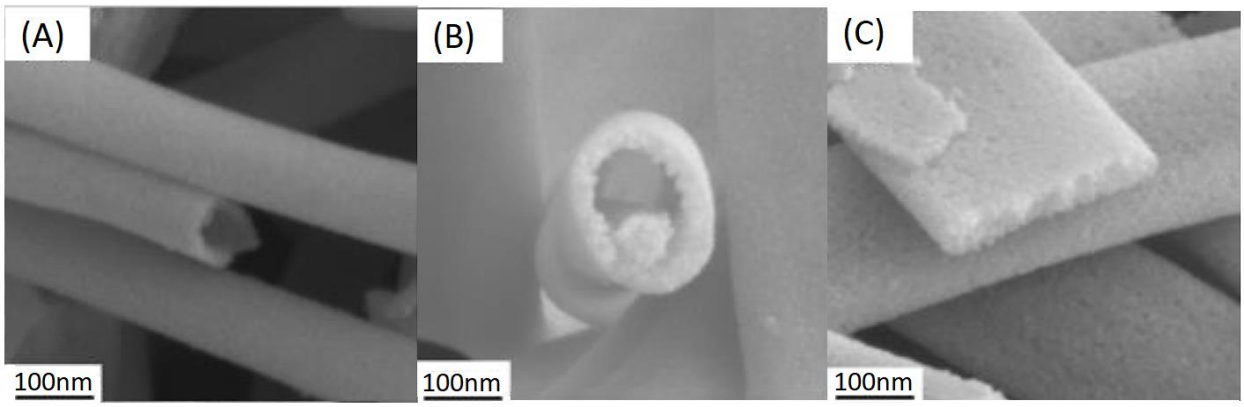

Figure 18: TEM images of a nanotube (A), a wire-in-nanotubes (B) and a nanobelt (C)[70]

Two dimensions (2D) structures such as nanosheets (Figure 19), can be assembled with different shapes if needed, they can be square, round or elongated in one direction. Often their synthesis takes place starting from a reorganization of nanocrystals.[71]

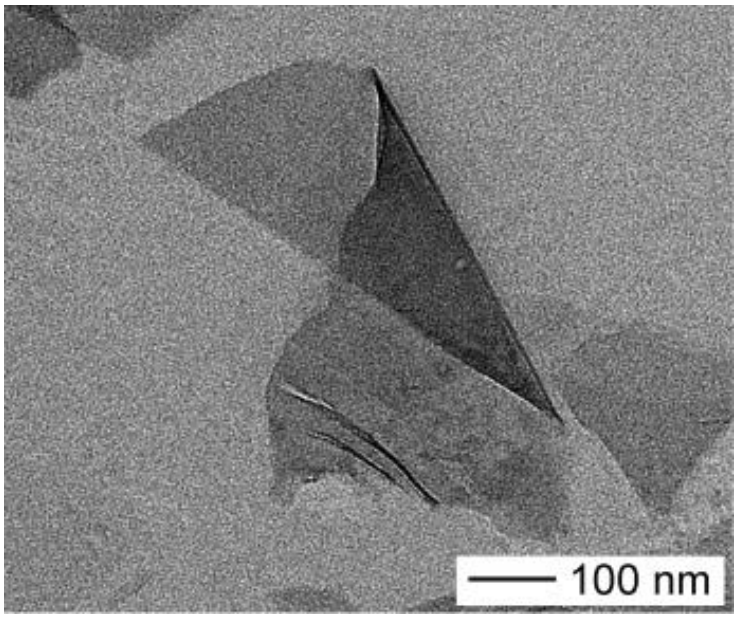

Figure 19: TEM images of a nanosheet[71]

Three dimensions (3D) structures have nanometric cavities and high values of width, length and thickness even of micrometric scale. Hollow microspheres typically have a porous surface structure (Figure 20 A). More particular structures are the nanospheres that assume a flower-like conformation, the overall structures are micrometric while the pores have a nanometric size (Figure 20 B). This structure is particularly interesting because it manages to maintain the advantages of both micrometric and nanometric materials: the separation is easy because the overall structure is large microns, the petal structure prevents further aggregation, an interconnected structure and a high number of pores ensures a high surface area value. [72,73]

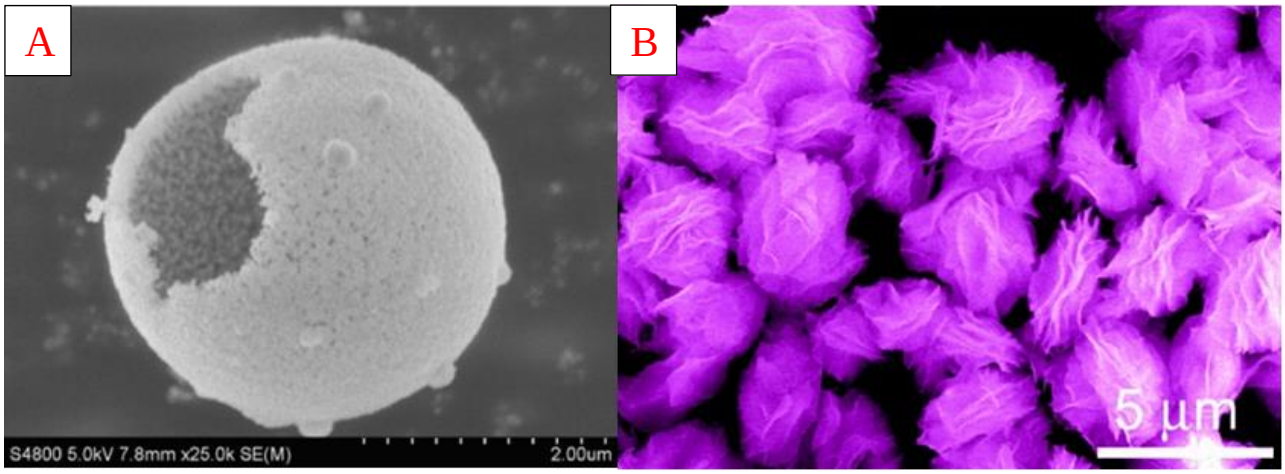

Figure 20: SEM images of a hallow ceria nanosphere (A) and several micrometric flowerlike ceria structures[72,73]

1.3.2 *Factors that influence the morphology of ceria*

Different synthesis methods have been developed to produce different ceria nanostructures: A variety of methods exist for the preparation of CeO2 nanostructures, including sol-gel approaches[74], solid-state reactions[75], mechanical–chemical processing[76], solvothermal methods[77], spray pyrolysis[78], spray freeze drying[79], ball milling[80], hydrothermal[81], electrospinning[82], and precipitation techniques[83].

The morphological structure depends on the thermodynamic and kinetic conditions in which the material is formed. The most stable structure is formed under thermodynamic conditions. While the synthesis of structures at a higher energy level takes place through the control of the nucleation and accretion processes in the various directions. The factors that influence the obtainment of the different morphologies are common to all the synthetic methodologies and are pressure, temperature, pH, solvent, presence of additives, concentration, presence of templating agents and characteristics of the precursors.

1.4 CeO_2 1D structures production via electrospinning

This work is focused on the production and the study of ceria nanostructures used as catalyst support and prepared using electrospinning techniques.

Electrospinning is a reliable technique to ideally form a continuous 1D structure of polymers or metal oxides with controllable diameter and morphology, such as nanofibers, nanotubes, wire-in-nanotubes, nanobelts, etc. [82]

The first electrospinning setup was patented in 1934, but the term "electrospinning" and a more detailed mechanistic understanding of the technique comes only during the 1990s with a more consistent number of publications about it. The electrospinning is essentially an extrusion of a polymeric solution from a charged needle or charged spinneret, the electric field formed between the spinneret and a collector surface stretch the material, while the solvent evaporates during the flying time. Tuning the geometry of the spinnerets, the components of the solution, the flow, the applied charge etc. and applying other operations steps (e.g., calcination, non-solvent bath, etc.) is possible to obtain 1D structures with different geometries.

1.4.1 *The electrospinning apparatus*

The main parts of a basic electrospinning apparatus are (Figure 21)[82]:

- a syringe as solution reservoir
- a pump for feeding the solution to be electrospun
- a spinneret (e.g., the metallic needle on the syringe)
- a high voltage power supply (DC) which supplies a high voltage (usually 1‑50 kV) to the spinneret and, if possible, an opposite charge to the collector
- a collector that collects the nanofibers; the collector could be either grounded or charged by the power supplier with an opposite charge to the one applied to the spinneret.

When the high voltage supply is turned on, an electrostatic field is created between the spinneret and the grounded (or charged) collector. If the repulsive electrostatic forces overcome the surface tension between the liquid molecules, a polymer jet is generated and it is subjected to shear stress during its path to the collector. Both repulsive and coulombic electrostatic forces distort the shape of the liquid droplet in the proximity of the spinneret into a conical meniscus called "Taylor cone". This structure is first transformed into a straight segment which is progressively stretched until forming fibres having a diameter in the nanometer scale.

Simultaneously, the solvent present in the polymeric jet evaporates, allowing to collect dry nanofibres on the collector (Figure 21-A).

The polymer molecular weight, as well as solution concentration, should be selected carefully to carry out a stable electrospinning process and to obtain good quality nanofibres. The polymer solution must possess a sufficient viscosity to prevent the breakage of the travelling jet and avoid the formation of small droplets instead of nanofibres (electrospray, Figure 21-B).

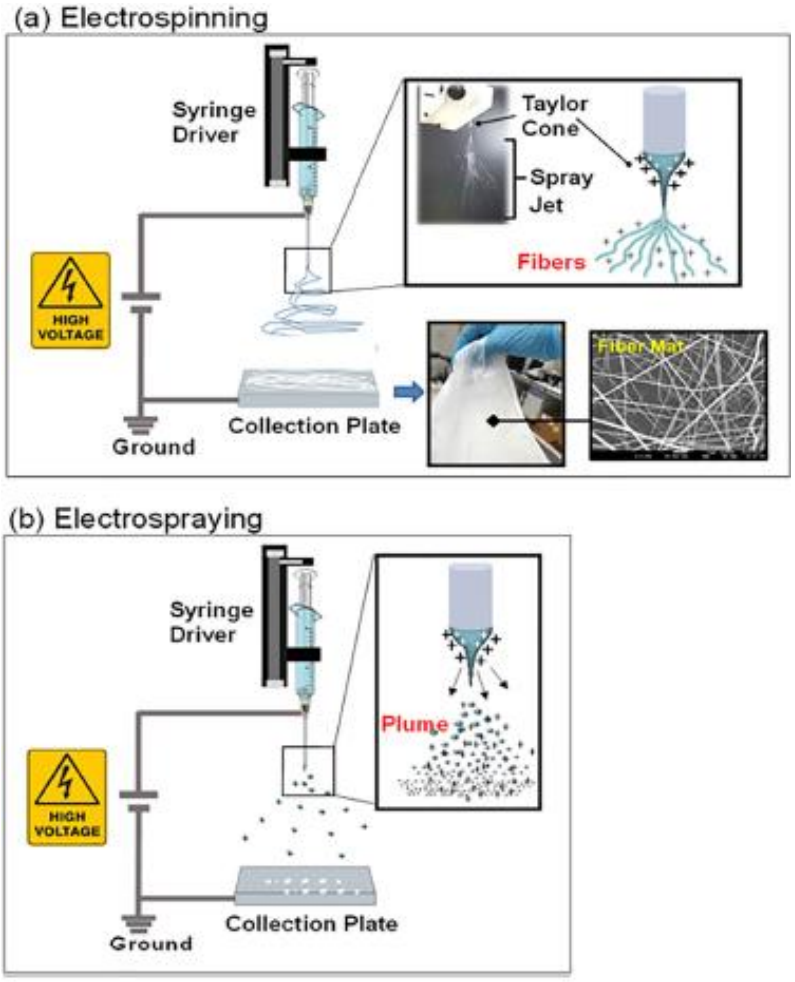

Figure 21: a possible spinning setup use for electrospinning (A) or electrospray (B)

Different parameters must be taken into account to obtain the desired nanofibrous morphology:

- Solution parameters (viscosity, surface tension, electrical conductivity)
- Process parameters and type of apparatus
- Environmental parameters

1.4.1.1 Solution parameters

The viscosity determines the concentration range of the solution to obtain continuous and beaded-free fibres. Low polymer concentrations usually form drops and beads associated with the fibre due to insufficient polymer entanglement. Increasing the polymer viscosity reduces the dripping and tends to form fibre with a greater diameter, both the polymer concentrations and molecular weight can be tuned to obtain the desired viscosity and fibrous morphology

The surface tension is less sensitive to the polymer concentration but is strongly dependent on the composition and the polarity of the solvent. It must be reduced in order to let the polymer be starched by the electrostatic force and create homogeneous fibres at low voltages. The surface tension can be reduced by changing the composition of the solution or adding a surfactant to it. A high surface tension could deform the polymer jet and even create droplets, leading to electrospray.

The electrical conductivity is proportional to the ionic strength of the solution; it indicates the lower limit of the voltage to overcome the surface tension. The electrical conductivity at constant temperature depends on the type of polymer, pH, presence of salts, ionic surfactants, or organometallic salts as ceramic precursors.

1.4.1.2 Process parameters and type of apparatus

The electric field strength must be higher than a critical threshold value, over this value the electric force is greater than the surface tension and the fibre can be stretched. Both the electric field and the spinneret-collector distance has to be fixed to avoid wagging or dripping. Usually, the electric field required is lower than 4 kV/cm.[84]

The feed rate is essential to control both the productivity and the diameter of the final fibre, as well as the process stability over time. By fixing this parameter, it is possible to obtain nanofibers with diameters between 5 and 100nm.

A basic electrospinning apparatus produces random non-nonwoven fabrics, that can be employed as a catalyst, filters, and coating. For structural application aligned nanofibers could be required because their mechanical properties, in that case, **the collector geometry, multiple**

spinnerets distribution and **deposition approaches** (e.g., a submerged collecting surface in a non-solvent medium and the following stretching of the fibres) can be used to align the fibres[85]

The **spinnerets used** can be a normal needle or can have a more complicated geometry to combine different spinning solution to produce a single composite material. Dual or coaxial spinnerets needle allow the combining of two different polymer solutions at the same time. Changing the geometry of the system is possible to create core-shell, bi-component, hollow, and porous NFs, (e.g.) core-shell NFs can be created via coaxial electrospinning of two different solutions, injecting the first one in the inner capillary (core) and the other one in the outer capillary (shell) at the same time to create composites fibres. [82]

1.4.1.3 Environmental parameters

The ambient temperature, humidity, and air velocity in the electrospinning chamber are key factors to control the diameter, morphology, and uniformity of fibre diameters. Fast evaporation conditions produce smaller NFs but, if the conditions rise too much, they can cause problems with the flux of material in the spinneret.

The humidity plays a fundamental role in the process. If it is higher than a threshold value it can alter the charge distribution on the growing NFs and lead to a bigger diameter, it could also create undesired corona discharges. A lower relative humidity level can lead to the formation of a porous surface texture by speeding up the solvent evaporation process.

Soft templating methods and polymer blends have been used to obtain the desired surface texture and internal porosity. High volatile solvents or selective solvent extraction have been exploited to remove specifically some component of an extruded NFs and create the desired number of pores on it. Other methods to selectively remove a component can be used too, e.g., immersion/precipitation in a non-solvent bath or a cryogenic liquid.

1.4.2 *1D metal oxide structures synthesis via electrospinning*

1D nanostructures, such as nanotubes (NTs), nanobelts (NBs), nanofibers (NFs), and wire-in-tubes (WTs), have gained special academic attention due to their special structure and large surface-to-volume ratio, which can apply in catalysis, batteries production and gas sensing technologies. However, they are not always easy to prepare, e.g., tem\tes contained in the fibres must be removed using a special organic solvent or further calcination steps to form a hollow structure. [86]

1D structures made from metal oxides are produced via electrospinning techniques from a solution containing their precursors (e.g. $Ce(NO_3)_3 \cdot 6H_2O$), a polymer (e.g., Polyvinyl alcohol) or a polymer blend, and co-solvents to control the viscosity and the ending surface texture (e.g. water or isopropanol). The product is then heat-treated in order to form the desired metal oxide phase, remove the unwanted components (as the polymer used) and obtain the correct surface morphology.

NTs prepared using a coaxial electrospinning technique requires an extremely complicated and expansive dual capillary nozzle. Furthermore, the diameter of the NTs prepared by coaxial electrospinning methods is rather large, which results in a low surface area.

New techniques have been developed to obtain the desired morphology using a simple spinning setup and few synthesis steps.

Kyriaki et Al. managed to optimise a facile spinning-calcination procedure to obtained nanobelts or nanotubes from the same spinning solution, containing N,N-Dimethylformamide (DMF), Polyvinylpyrrolidone (PVP), cerium nitrate and, chloroauric acid and using a simple mono-spinneret setup (Figure 22). Nanobelts samples have been prepared through one-step calcination, exploiting the Kirkendall effect, which pushes the cerium atoms to diffuse away from the centre of the fibres, a belt-like structure was formed, the width of the belts was lower increasing the temperature ramp. The nanotubes were prepared using a two-step heating ramp, exploiting the gas expansion energy given by the vapours of the solvent and the gasses from the degradation of both PVP and cerium precursors.[86]

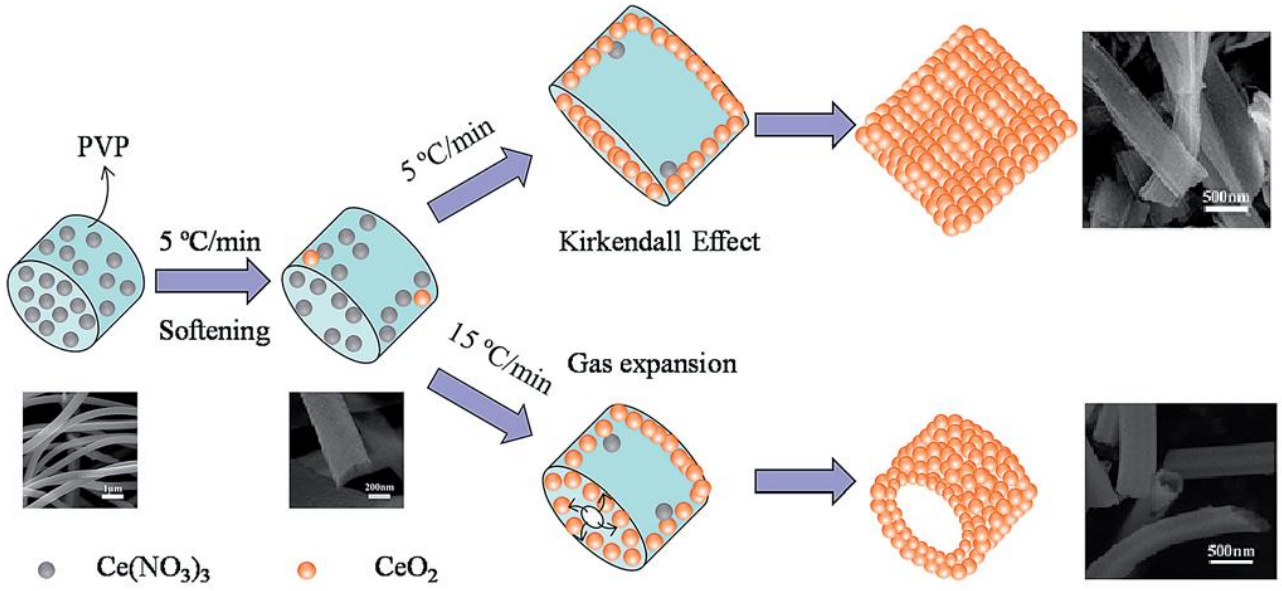

Figure 22: Scheme of the calcination procedure to obtain nanobelts or nanotubes[86]

Dengfeng et al.[70] produced three different cerium oxide morphologies (Figure 23) using a single spinneret setup and a rotating grounded collector and a simple one-step calcination process, using different PVP in DMF solutions on the same spinning setup they influenced the final morphologies.

The solutions were composed of PVP and cerium nitrate in DMF solvent and prepared using three different PVP with increasing molecular weight (K40, K50 and K90), in the solution with the highest PVP molecular weight they used as solvent a mixture DMF:EtOH in 1:1 ratio.

After spinning the three solutions they obtained a similar nanofibers structure, then all the samples have been calcinated in a muffle at 600°C for 3h.

SEM images of the samples after calcination revealed a nanotube structure for the sample with the lowest PVP molecular weight and a nanobelt structure for the sample with the intermediate PVP molecular weight. They proposed that this difference was caused by the more intense combustion of the PVP with the intermediate molecular weight, which resulted in a higher gasses pressure that buckled the structure into a flattened nanobelt, rather than a regular nanotube (Figure 24). The calcination of the third sample revealed a wire-in-tube structure, they assumed that due to the different boiling point of the two solvents ($T_{eb\text{-}ethanol}$=78 °C, $T_{eb\text{-}DMF}$ =152°C), ethanol boiled first and the cerium nitrate on the surface was the first to degrade and left a rigid shell. Then, the inner gel-like core of the tube, composed of DMF and cerium nitrate,

started shrinking because of the DMF evaporation and the degradation of PVP and ceria precursor. This process left the thin wire structure encapsulated into the main nanotube.

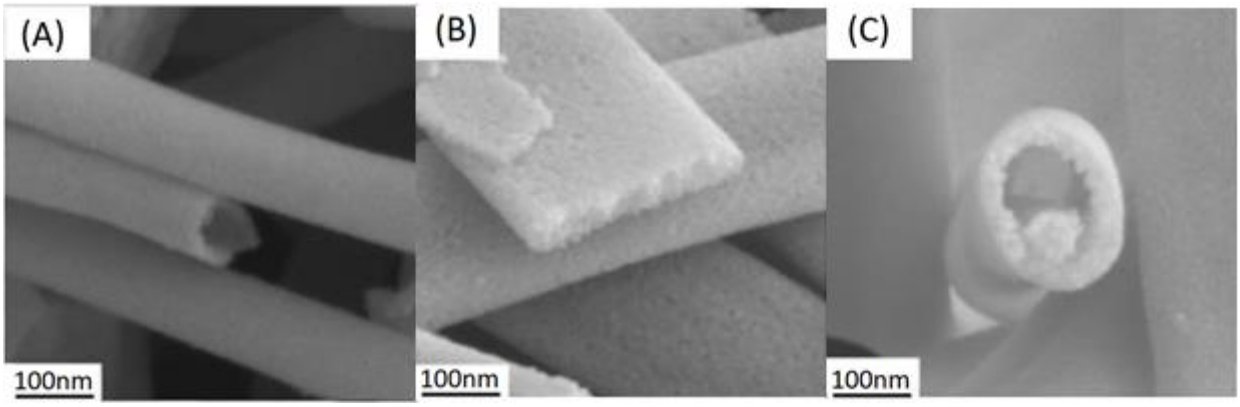

Figure 23: TEM images of a nanotube (A), a nanobelt (B) and a wire-in-nanotubes (C)[70]

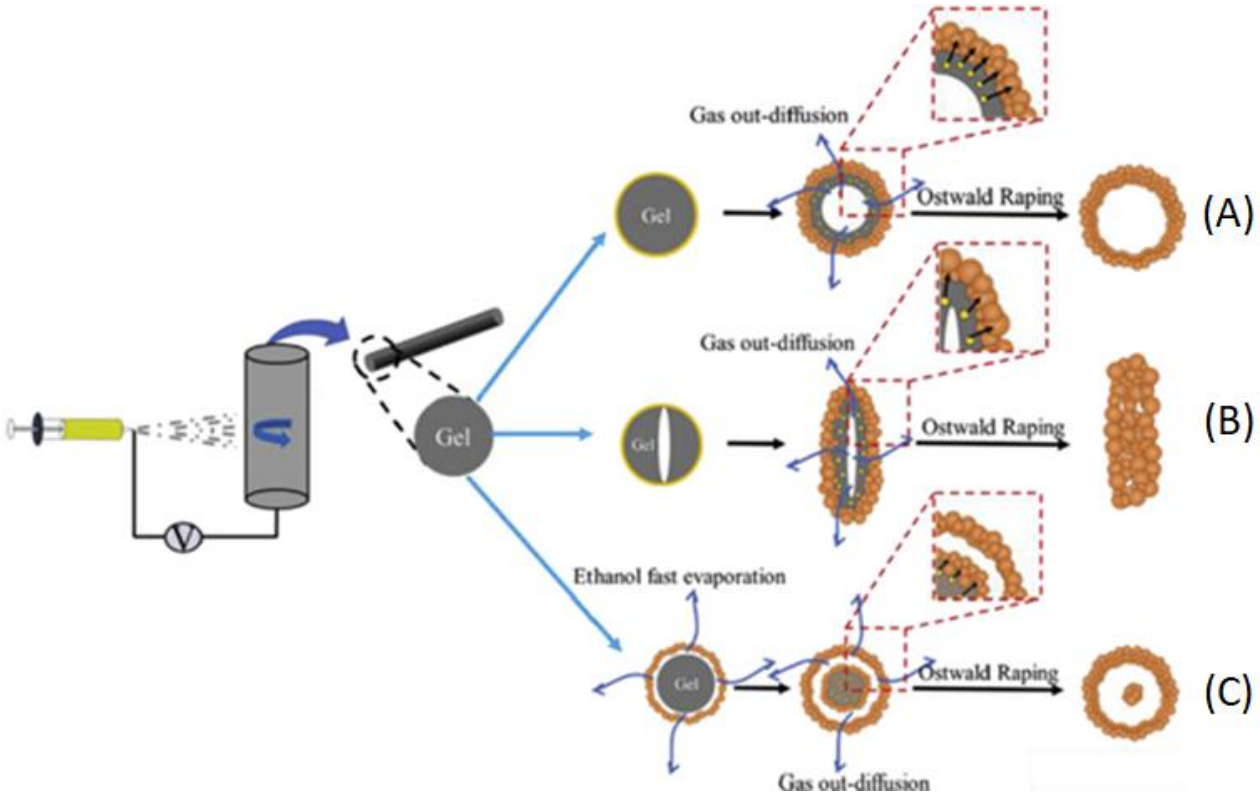

Figure 24: Scheme of the processes involved in the production of nanotubes(A), nanobelts(B) a wire-in-nanotube (C)[70]

1.4.3 *CeO_2 structures decorated with gold*

A metal phase can be added to the fibres in different ways[82]: by mixing a desired metal nanoparticles solution with the electrospinning solution, by adding a metal precursor (e.g., chloroauric acid) in the spinning solution, pre-forming the ceramic oxide NFs and then adding the metal NPs via wet laying or deposition precipitation.

The method where the metal or its precursor is added in the spinning solution is called "one-pot synesis", these processes are cost-saving compared to the others. During the calcination step, the catalyst migrates from the inner parts of the fibre to its surface. Additional reduction steps may be required to obtain the desired metal phase.

Metal nanoparticles or a metal precursor can be used both in the one-pot synthesis method. [86]

Both the one pot and two pot synthesis have been used To decorate CeO_2 with Au NPs, the one-pot systems have been performed both using already made Au NPs or $HAuCl_4$ and PVP polymer as precursor inside the electrospinning solution.[82]

1.5 References:

1. Heo, J. B., Lee, Y.-S. & Chung, C.-H. Raw plant-based biorefinery: A new paradigm shift towards biotechnological approach to sustainable manufacturing of HMF. *Biotechnology Advances* **37**, 107422 (2019).
2. Anastas, P. T., Bartlett, L. B., Kirchhoff, M. M. & Williamson, T. C. The role of catalysis in the design, development, and implementation of green chemistry. *Catalysis Today* **55**, 11–22 (2000).
3. Bozell, J. J. & Petersen, G. R. Technology development for the production of biobased products from biorefinery carbohydrates—the US Department of Energy's "Top 10" revisited. *Green Chem.* **12**, 539–554 (2010).
4. López, C. Chemical Routes for the Transformation of Biomass into Chemicals.
5. AVA Biochem: commercialising renewable platform chemical 5-HMF. https://www.degruyter.com/document/doi/10.1515/gps-2014-0029/html.
6. Lima, S., Chadwick, D. & Hellgardt, K. Towards sustainable hydrogenation of 5-(hydroxymethyl)furfural: a two-stage continuous process in aqueous media over RANEY® catalysts. *RSC Adv.* **7**, 31401–31407 (2017).
7. van Putten, R.-J. *et al.* Hydroxymethylfurfural, A Versatile Platform Chemical Made from Renewable Resources. *Chem. Rev.* **113**, 1499–1597 (2013).
8. Chemistry of the Elements - 2nd Edition. https://www.elsevier.com/books/chemistry-of-the-elements/greenwood/978-0-7506-3365-9.
9. Gritschneder, S. & Reichling, M. Structural elements of CeO2(111) surfaces. *Nanotechnology* **18**, 044024 (2006).
10. Trovarelli, A. & Llorca, J. Ceria Catalysts at Nanoscale: How Do Crystal Shapes Shape Catalysis? *ACS Catal.* **7**, 4716–4735 (2017).
11. Zhang, D., Du, X., Shi, L. & Gao, R. Shape-controlled synthesis and catalytic application of ceria nanomaterials. *Dalton Transactions* **41**, 14455–14475 (2012).
12. Menegazzo, F., Signoretto, M., Fantinel, T. & Manzoli, M. Sol-immobilized vs deposited-precipitated Au nanoparticles supported on CeO2 for furfural oxidative esterification. *Journal of Chemical Technology & Biotechnology* **92**, 2196–2205 (2017).
13. An Economic Impact Analysis of the US Biobased Products Industry: A Report to the Congress of the United States of America | Industrial Biotechnology. https://www.liebertpub.com/doi/10.1089/ind.2015.29002.jsg.

14. Dalai, A. K. & Bassi, A. Bioenergy and Green Engineering. *Energy Fuels* **24**, 4627–4627 (2010).
15. Teong, S. P., Yi, G. & Zhang, Y. Hydroxymethylfurfural production from bioresources: past, present and future. *Green Chem.* **16**, 2015–2026 (2014).
16. Ionic Liquid-Mediated Formation of 5-Hydroxymethylfurfural—A Promising Biomass-Derived Building Block | Chemical Reviews. https://pubs.acs.org/doi/10.1021/cr100171a.
17. Lewkowski, J. Synthesis, chemistry and applications of 5-hydroxymethylfurfural and its derivatives. *Archive for organic chemistry* 17–54 (2001).
18. Combustion and Emissions of 2,5-Dimethylfuran in a Direct-Injection Spark-Ignition Engine | Energy & Fuels. https://pubs.acs.org/doi/abs/10.1021/ef901575a.
19. PubChem. 5-Hydroxymethylfurfural. https://pubchem.ncbi.nlm.nih.gov/compound/237332.
20. Shapla, U. M., Solayman, M., Alam, N., Khalil, M. I. & Gan, S. H. 5-Hydroxymethylfurfural (HMF) levels in honey and other food products: effects on bees and human health. *Chem Cent J* **12**, 35 (2018).
21. Development of a continuous catalytic heterogeneous column reactor with simultaneous extraction of an intermediate product by an organic solvent circulating in countercurrent manner with the aqueous phase - ScienceDirect. https://www.sciencedirect.com/science/article/pii/092058619500026C.
22. Antal, M. J., Mok, W. S. L. & Richards, G. N. Mechanism of formation of 5-(hydroxymethyl)-2-furaldehyde from d-fructose and sucrose. *Carbohydrate Research* **199**, 91–109 (1990).
23. Ritz, J., Fuchs, H., Kieczka, H. & Moran, W. C. Ullmann's Encyclopedia of Industrial Chemistry. (2013) doi:10.1002/14356007.a05_031.pub2.
24. Xiao, B. *et al.* Synthesis of 1,6-hexanediol from HMF over double-layered catalysts of Pd/SiO2 + Ir–ReOx/SiO2 in a fixed-bed reactor. *Green Chem.* **18**, 2175–2184 (2016).
25. A direct route to adipic acid esters. *Chemical Engineering* https://www.chemengonline.com/direct-route-adipic-acid-esters/ (2020).
26. Akmaz, S., Esen, M., Sezgin, E. & Koc, S. N. Efficient manganese decorated cobalt based catalysts for hydrogenation of 5-hydroxymethylfurfural (HMF) to 2,5-dimethylfuran (DMF) biofuel. *The Canadian Journal of Chemical Engineering* **98**, 138–146 (2020).
27. Ait Rass, H., Essayem, N. & Besson, M. Selective aqueous phase oxidation of 5-hydroxymethylfurfural to 2,5-furandicarboxylic acid over Pt/C catalysts: influence of the base and effect of bismuth promotion. *Green Chem.* **15**, 2240 (2013).

28. Li, Q. *et al.* Selective oxidation of 5-hydroxymethylfurfural to 2,5-furandicarboxylic acid over Au/CeO 2 catalysts: The morphology effect of CeO 2. *Catalysis Science & Technology* **9**, (2019).
29. Hameed, S., Lin, L., Wang, A. & Luo, W. Recent Developments in Metal-Based Catalysts for the Catalytic Aerobic Oxidation of 5-Hydroxymethyl-Furfural to 2,5-Furandicarboxylic Acid. *Catalysts* **10**, 120 (2020).
30. Girisuta, B., Janssen, L. P. B. M. & Heeres, H. J. A kinetic study on the decomposition of 5-hydroxymethylfurfural into levulinic acid. *Green Chem.* **8**, 701–709 (2006).
31. Lolli, A. *et al.* Hard-template preparation of Au/CeO2 mesostructured catalysts and their activity for the selective oxidation of 5-hydroxymethylfurfural to 2,5-furandicarboxylic acid. *Microporous and Mesoporous Materials* **226**, 466–475 (2016).
32. Casanova, O., Iborra, S. & Corma, A. Biomass into chemicals: aerobic oxidation of 5-hydroxymethyl-2-furfural into 2,5-furandicarboxylic acid with gold nanoparticle catalysts. *ChemSusChem* **2**, 1138–1144 (2009).
33. Electrocatalytic oxidation of 5-hydroxymethylfurfural to 2,5-furandicarboxylic acid on supported Au and Pd bimetallic nanoparticles - Green Chemistry (RSC Publishing). https://pubs.rsc.org/--/content/articlelanding/2014/gc/c4gc00401a/unauth#!divAbstract.
34. Kamm, B. Biorefineries – their scenarios and challenges. *Pure and Applied Chemistry* **86**, 821–831 (2014).
35. Werpy, T. & Petersen, G. *Top Value Added Chemicals from Biomass: Volume I -- Results of Screening for Potential Candidates from Sugars and Synthesis Gas*. https://www.osti.gov/biblio/15008859-top-value-added-chemicals-from-biomass-volume-results-screening-potential-candidates-from-sugars-synthesis-gas (2004) doi:10.2172/15008859.
36. Shen, X., Xia, D., Xiang, Y. & Gao, J. γ-valerolactone (GVL) as a bio-based green solvent and ligand for iron-mediated AGET ATRP. *e-Polymers* **19**, 323–329 (2019).
37. γ-Valerolactone Ring-Opening and Decarboxylation over SiO2/Al2O3 in the Presence of Water | Langmuir. https://pubs.acs.org/doi/10.1021/la101424a.
38. Tang, X. *et al.* Production of γ-valerolactone from lignocellulosic biomass for sustainable fuels and chemicals supply. *Renewable and Sustainable Energy Reviews* **40**, 608–620 (2014).
39. Green Polymer Precursors from Biomass-Based Levulinic Acid - ScienceDirect. https://www.sciencedirect.com/science/article/pii/S187661961200037X.

40. Synthesis of Transportation Fuels from Biomass: Chemistry, Catalysts, and Engineering | Chemical Reviews. https://pubs.acs.org/doi/abs/10.1021/cr068360d.
41. Singlet oxygen in surface waters. 3. Photochemical formation and steady-state concentrations in various types of waters | Environmental Science & Technology. https://pubs.acs.org/doi/abs/10.1021/es00146a005.
42. Sajid, M., Zhao, X. & Liu, D. Production of 2,5-furandicarboxylic acid (FDCA) from 5-hydroxymethylfurfural (HMF): recent progress focusing on the chemical-catalytic routes. *Green Chem.* **20**, 5427–5453 (2018).
43. Wang, K.-F., Liu, C., Sui, K., Guo, C. & Liu, C.-Z. Efficient Catalytic Oxidation of 5-Hydroxymethylfurfural to 2,5-Furandicarboxylic Acid by Magnetic Laccase Catalyst. *ChemBioChem* **19**, 654–659 (2018).
44. Davis, S. E., Zope, B. N. & Davis, R. J. On the mechanism of selective oxidation of 5-hydroxymethylfurfural to 2,5-furandicarboxylic acid over supported Pt and Au catalysts. *Green Chem.* **14**, 143–147 (2012).
45. Davis, S. E. *et al.* Kinetics and mechanism of 5-hydroxymethylfurfural oxidation and their implications for catalyst development. *Journal of Molecular Catalysis A: Chemical* **388–389**, 123–132 (2014).
46. Reactivity of the Gold/Water Interface During Selective Oxidation Catalysis | Science. https://science.sciencemag.org/content/330/6000/74.abstract?casa_token=OcX2ZXWsf4YAAAAA:Ns-qarrNTsnMb85Vnuf0HXTbG44jHRoEaIOop4XTCYxSypF2g-GOJwFH_5uw2-5ldTmBsRlKsGR3.
47. Villa, A., Schiavoni, M., Campisi, S., Veith, G. M. & Prati, L. Pd-modified Au on carbon as an effective and durable catalyst for the direct oxidation of HMF to 2,5-furandicarboxylic acid. *ChemSusChem* **6**, 609–612 (2013).
48. Gupta, N. K., Nishimura, S., Takagaki, A. & Ebitani, K. Hydrotalcite-supported gold-nanoparticle-catalyzed highly efficient base-free aqueous oxidation of 5-hydroxymethylfurfural into 2,5-furandicarboxylic acid under atmospheric oxygen pressure. *Green Chem.* **13**, 824–827 (2011).
49. Han, X. *et al.* Base-free aerobic oxidation of 5-hydroxymethylfurfural to 2,5-furandicarboxylic acid over a Pt/C–O–Mg catalyst. *Green Chem.* **18**, 1597–1604 (2016).
50. Zope, B. N., Davis, S. E. & Davis, R. J. Influence of Reaction Conditions on Diacid Formation During Au-Catalyzed Oxidation of Glycerol and Hydroxymethylfurfural. *Top Catal* **55**, 24–32 (2012).

51. Bonincontro, D. *et al.* AuPd-nNiO as an effective catalyst for the base-free oxidation of HMF under mild reaction conditions. *Green Chem.* **21**, 4090–4099 (2019).
52. Highly Efficient and Stable Bimetallic AuPd over La-Doped Ca–Mg–Al Layered Double Hydroxide for Base-Free Aerobic Oxidation of 5-Hydroxymethylfurfural in Water | ACS Sustainable Chemistry & Engineering. https://pubs.acs.org/doi/abs/10.1021/acssuschemeng.7b00573.
53. Sun, C., Li, H. & Chen, L. Nanostructured ceria-based materials: synthesis, properties, and applications. *Energy Environ. Sci.* **5**, 8475–8505 (2012).
54. Kašpar, J., Fornasiero, P. & Graziani, M. Use of CeO2-based oxides in the three-way catalysis. *Catalysis Today* **50**, 285–298 (1999).
55. Mogensen, M. B., Sammes, N. M. & Tompsett, G. A. Physical, chemical and electrochemical properties of pure and doped ceria. *Solid State Ionics* **129**, 63–94 (2000).
56. Shanmugam, V., Zapf, R., Hessel, V., Pennemann, H. & Kolb, G. Nano-architectured CeO2 supported Rh with remarkably enhanced catalytic activity for propylene glycol reforming reaction in microreactors. *Applied Catalysis B: Environmental* **226**, 403–411 (2018).
57. Agarwal, S., Mojet, B. L., Lefferts, L. & Datye, A. K. Chapter 2 - Ceria Nanoshapes-Structural and Catalytic Properties. *Catalysis by Materials with Well-Defined Structures* 31–70 (2015) doi:10.1016/B978-0-12-801217-8.00002-5.
58. Nolan, M., Parker, S. C. & Watson, G. W. The electronic structure of oxygen vacancy defects at the low index surfaces of ceria. *Surface Science* **595**, 223–232 (2005).
59. *Preperative Inorganic Chemistry, Volume 2 Brauer*.
60. Li, S. *et al.* Catalytic Performance of Gold Supported on Mn, Fe and Ni Doped Ceria in the Preferential Oxidation of CO in H2-Rich Stream. *Catalysts* **8**, 469 (2018).
61. Kumar, S. & Ojha, A. K. Ni, Co and Ni–Co codoping induced modification in shape, optical band gap and enhanced photocatalytic activity of CeO2 nanostructures for photodegradation of methylene blue dye under visible light irradiation. *RSC Adv.* **6**, 8651–8660 (2016).
62. Hoa, N. K., Rahman, H. A. & Rao Somalu, M. Preparation of Nickel Oxide-Samarium-Doped Ceria Carbonate Composite Anode Powders by Using High-Energy Ball Milling for Low-Temperature Solid Oxide Fuel Cells. *Materials Science Forum* vol. 840 97–102 https://www.scientific.net/MSF.840.97 (2016).
63. Li, P., Chen, X., Li, Y. & Schwank, J. W. A review on oxygen storage capacity of CeO2-based materials: Influence factors, measurement techniques, and applications in reactions related to catalytic automotive emissions control. *Catalysis Today* **327**, 90–115 (2019).

64. Seal, S. *et al.* Engineered defects in cerium oxides: tuning chemical reactivity for biomedical, environmental, & energy applications. *Nanoscale* **12**, 6879–6899 (2020).
65. Mai, H.-X. *et al.* Shape-Selective Synthesis and Oxygen Storage Behavior of Ceria Nanopolyhedra, Nanorods, and Nanocubes. *J. Phys. Chem. B* **109**, 24380–24385 (2005).
66. Baudin, M., Wójcik, M. & Hermansson, K. Dynamics, structure and energetics of the (111), (011) and (001) surfaces of ceria. *Surface Science* **468**, 51–61 (2000).
67. Swartz, S. L. Catalysis by Ceria and Related Materials Edited by Alessandro Trovarelli (Università di Udine, Italy). Catalytic Science Series. Volume 2. Series Edited by Graham J. Hutchings. Imperial College Press: London. 2002. vviii + 508 pp. $78.00. ISBN: 1-86094-299-7. *J. Am. Chem. Soc.* **124**, 12923–12924 (2002).
68. Wu, Z., Li, M. & Overbury, S. On the structure dependence of CO oxidation over CeO 2 nanocrystals with well-defined surface planes. *Journal of Catalysis - J CATAL* **285**, 61–73 (2012).
69. Mann, A. K. P., Wu, Z. & Overbury, S. H. Chapter 3 - The Characterization and Structure-Dependent Catalysis of Ceria with Well-Defined Facets. in *Catalysis by Materials with Well-Defined Structures* (eds. Wu, Z. & Overbury, S. H.) 71–97 (Elsevier, 2015). doi:10.1016/B978-0-12-801217-8.00003-7.
70. Yan, D. *et al.* Morphology-activity correlation of electrospun CeO2 for toluene catalytic combustion. *Chemosphere* **247**, 125860 (2020).
71. Aqueous-Phase Synthesis of Single-Crystal Ceria Nanosheets - Yu - 2010 - Angewandte Chemie International Edition - Wiley Online Library. https://onlinelibrary.wiley.com/doi/abs/10.1002/anie.201001521.
72. 3D Flowerlike Ceria Micro/Nanocomposite Structure and Its Application for Water Treatment and CO Removal | Chemistry of Materials. https://pubs.acs.org/doi/pdf/10.1021/cm062471b.
73. Yang, Z., Liu, L., Liang, H., Yang, H. & Yang, Y. One-pot hydrothermal synthesis of CeO 2 hollow microspheres. *Journal of Crystal Growth* **312**, 426–430 (2010).
74. Baqer, A. A. *et al.* Effect of polyvinylpyrrolidone on cerium oxide nanoparticle characteristics prepared by a facile heat treatment technique. *Results in Physics* **7**, 611–619 (2017).
75. Dhall, A. & Self, W. Cerium Oxide Nanoparticles: A Brief Review of Their Synthesis Methods and Biomedical Applications. *Antioxidants (Basel)* **7**, (2018).
76. Ozaki, T. *et al.* Redox Behavior of Surface-Modified CeO2−ZrO2 Catalysts by Chemical Filing Process. *Chem. Mater.* **12**, 643–649 (2000).

77. Liu, X.-M., Gao, W.-L. & Zhang, J. Facile synthesis of monodispersed CeO2 nanostructures. *Journal of Physics and Chemistry of Solids* **72**, 1472–1476 (2011).
78. D'Angelo, A. M., Liu, A. C. Y. & Chaffee, A. L. Oxygen Uptake of Tb–CeO2: Analysis of Ce3+ and Oxygen Vacancies. *J. Phys. Chem. C* **120**, 14382–14389 (2016).
79. El-Hafiz, D. R. A., Ebiad, M. A. & Mohamed, L. S. Spray Freeze Drying as a Smart Method in Preparation of Ultra-Fine CeO2-MOX Materials. *Chemistry and Materials Research* **6**, 112–125 (2014).
80. Yadav, T. P., Mukhopadhyay, N. K. & Srivastava, O. N. Synthesis of Nano-Decagonal Quasicrystalline Material by Mechanical Alloying. *Advanced Science Letters* **20**, 1219–1223 (2014).
81. Zdravković, J. *et al.* Comparative study of CeO2 nanopowders obtained by the hydrothermal method from various precursors. *Ceramics International* **41**, 1970–1979 (2015).
82. Polychronopoulou, K. & Jaoudé, M. A. Nano-architectural advancement of CeO2-driven catalysis via electrospinning. *Surface and Coatings Technology* **350**, 245–280 (2018).
83. Hassanzadeh-Tabrizi, S. A., Mazaheri, M., Aminzare, M. & Sadrnezhaad, S. K. Reverse precipitation synthesis and characterization of CeO2 nanopowder. *Journal of Alloys and Compounds* **491**, 499–502 (2010).
84. Theron, S. A., Zussman, E. & Yarin, A. L. Experimental investigation of the governing parameters in the electrospinning of polymer solutions. *polymer* **45**, 2017–2030 (2004).
85. Carnell, L. S. *et al.* Aligned Mats from Electrospun Single Fibers. *Macromolecules* **41**, 5345–5349 (2008).
86. Liu, Y., Chen, H.-S., Li, J. & Yang, P. Morphology adjustment of one dimensional CeO2 nanostructures via calcination and their composite with Au nanoparticles towards enhanced catalysis. *RSC Adv.* **5**, 37585–37591 (2015).

2 Experimental section

2.1 Catalysts preparations

In this research have been prepared both catalyst samples supported on commercial ceria in powders and on nanofibers. The samples prepared and tested in this work are listed in Table 1 and resumed in Figure 25. The commercial supports used are ceria Evonik Degussa Gmbh and Solvay Rhodia Actalys HSA5, these supports have respectively low and high surface area, as reported from BET analysis in Table 1. The gold-containing catalysts supported on the Evonik Degussa Gmbh ceria have been labelled "Au/CeO_2 -C" while the catalyst supported on Ceria Solvay Rhodia Actalys HSA5 have been labelled "Au/CeO_2 -HS" ("high surface"). All Au-containing samples are 1.5% (wt./wt.) Au over the support.

The nanofibers have been spun with and without chloroauric acid in the spinning solution. The fibres without chloroauric acid and the commercial sample have been subjected to a Deposition Precipitation (DP) procedure, the DP is a well-known method in our laboratory to prepare catalyst with metal nanoparticles on inorganic supports (description of the DP procedure in chapter 2.1.1).

The nanofibers "as-spun" (after spinning) have been subjected to different calcination process in order to obtain the desired oxidic phase before the DP process. The heating ramp during the calcination in air was gentle, with a rate of 0.2°C/min and a isotherm maintenance at 300°C or 550°C for three hours, this was meant to not compromise the nanofibers structure during the PVP combustion.[1] The sample of nanofibers supports obtained (without the gold precursor) have been labelled CeO_2-NF_300 or CeO_2-NF_550 depending on the temperature chosen for the isotherm maintenance. The samples of catalysts obtained after gold deposition on these supports have been called "Au/CeO_2-NF _300" or "Au/CeO_2-NF_550".

$HAuCl_4$ has been used as metal precursor in a different batch of fibres, where it has been added to the spinning solution. The resulted material after spinning has been labelled "Au/NF as spun". In this sample, the PVP was still present, and the gold and the cerium were still in their precursor states. The "Au/NF as spun" have been used two prepare two different samples of catalyst following two different treatment: in the first one, the fibres have been calcined at 300°C (sample called "Au/CeO_2 -NF_C"). In the second one, the fibres have been thermal treated under N_2 flow and then calcined in air, both the treatments have been performed at 300°C (samples labelled "Au/CeO_2 -NF_P" after the heat treatment in N_2 and "Au/CeO_2 -

NF_PC" after the calcination in air). The detailed spinning procedure has been reported in chapter 3.3.

All the catalysts used have a metal loading of 1.5%wt, but, at the end of the DP, the solution of the first batch of nanofibers calcined at 550°C (sample Au/CeO_2 -NF_550) was still slightly magenta, suggesting the presence of some gold residue. Thus, the gold remaining in the solution was dissolved with a few drops of royal water and then determined by emission spectroscopy via ICP. The obtained result permit to calculate the experimental load of gold on sample Au/CeO2 -NF_550 as 1.43%wt., unlike the 1.5%wt. expected.

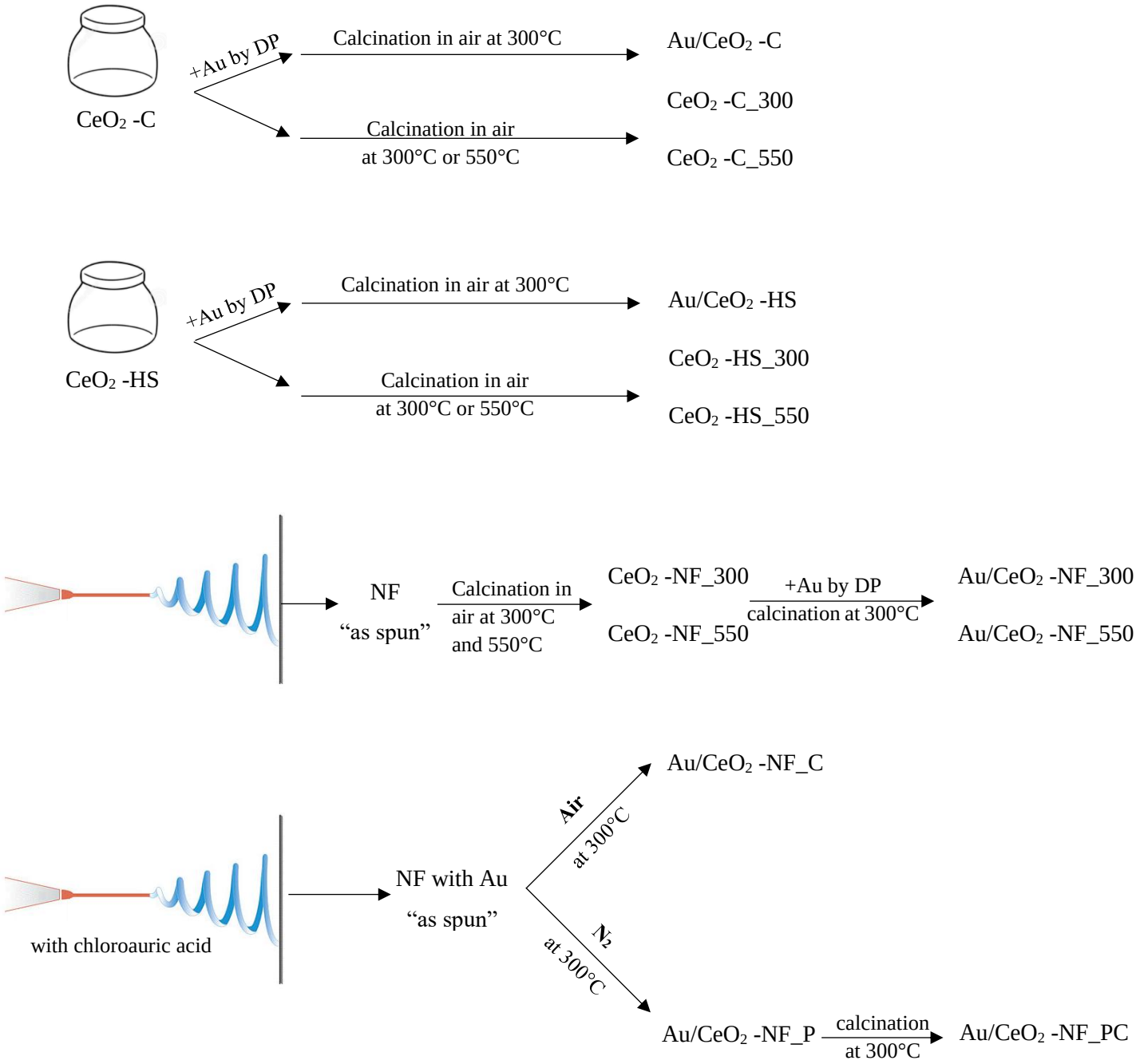

Figure 25: Resume of the preparations of the catalysts

Support	Sample name	Notes:
Ceria Evonik Degussa GmbH	CeO_2 -C	Commercial ceria support, low surface
	CeO_2 -C_300	Commercial ceria support, low surface, calcined at 300°C
	CeO_2 -C_550	Commercial ceria support, low surface, calcined at 550°C
	Au/CeO_2-C	Au supported on low surface commercial ceria, synthesised via DP, calcined at 300C°
Ceria Solvay Rhodia Actalys HSA5	CeO_2 -HS	Commercial ceria support, high surface
	CeO_2 -HS_300	Commercial ceria support, high surface calcined at 300°C
	CeO_2 -HS_550	Commercial ceria support, high surface, calcined at 550°C
	Au/CeO_2 -HS	Au supported on high surface commercial ceria, synthesised via DP, calcined at 300C°
Electrospun nanofibers	CeO_2 -NF_300	Ceria nanofiber support, calcined at 300°C
	CeO_2-NF_550	Ceria nanofiber support, calcined at 550°C
	Au/CeO_2-NF _300	Au supported on nanofiber support calcined at 300°C, synthesised via DP
	Au/CeO_2-NF _550	Au supported on nanofiber support calcined at 550°C, synthesised via DP
Electrospun nanofibers (spun with chloroauric acid)	Au/CeO_2-NF_C	Prepared by electrospinning using a solution containing $HAuCl_4$ and calcinating the fibres at 300°C in air
	Au/CeO_2-NF_P	Prepared by electrospinning using a solution containing $HAuCl_4$ followed by thermal treatment at 300°C in N_2
	Au/CeO_2-NF_PC	Prepared by electrospinning using a solution containing $HAuCl_4$ followed by thermal treatment at 300°C in N_2 and calcination in air at 300°C

Table 1: Surface area and data of catalysts and supports

2.1.1 *Procedure for Deposition Precipitation (DP) of gold nanoparticles on ceria supports*

The procedure used to perform the Deposition Precipitation (DP) on the supports is a well-known procedure for the preparation of gold supported catalysts[2]. The DP was performed by preparing a suspension of 0,75g of ceria in 112.5g of distilled water and a solution of $HAuCl_4$ with a concentration of 1mM, both brought to pH 8 using NaOH 0,1M. The solution of chloroauric acid was slowly added drop by drop into the ceria solution which was kept under vigorous stirring and pH 8 throughout the process to allow the deposition of hydroxide gold on the ceria support. At the end of the dripping process, the resulting solution was heated to 65 ºC for two hours under stirring and then, placed in an ultrasonic bath for 15 minutes. This last step was avoided during the DP process on nanofibers, in order to not compromise the nanostructure of the support. The solid was then separated from solution via filtration, washed several times with distilled water to eliminate residual chlorides, dried overnight in the stove at 110°C and finally calcined at 300°C or 550°C in a muffle, following a heating ramp of 2°C/min.

2.2 Instrumentation, reagents and methods

2.2.1 *Electrospinning setup*

The electrospinning setup used is composed of three main parts: a high voltage power supply, an infusion pump, and a grounded metallic plate as collector, covered with parchment paper, this type of paper was selected because the spun material doesn't stick to it, and was possible to remove it from the surface without damaging it (exposed from left to right in Figure 26). A glass syringe with a volume of 5 mL has been used to store the spinning solution during the process, the syringe has been mounted on the top of the pump and was equipped with a steel needle with an internal diameter of 0.51mm. The high voltage power supply has been used to charge the needle of the syringe (Figure 27), meanwhile, the collector was grounded in order to collect as many fibres as possible. The generator is a DC power supply FUG HCP and the pump is made by kdScientific.

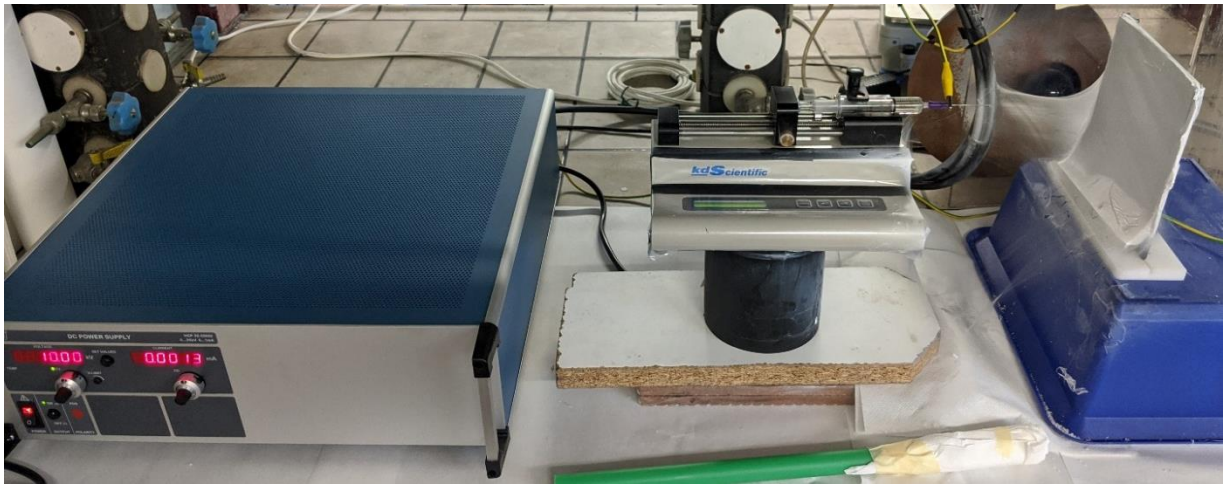

Figure 26: photo of the electrospinning setup: the high voltage power supply, the infusion pump and the collector (from left to right)

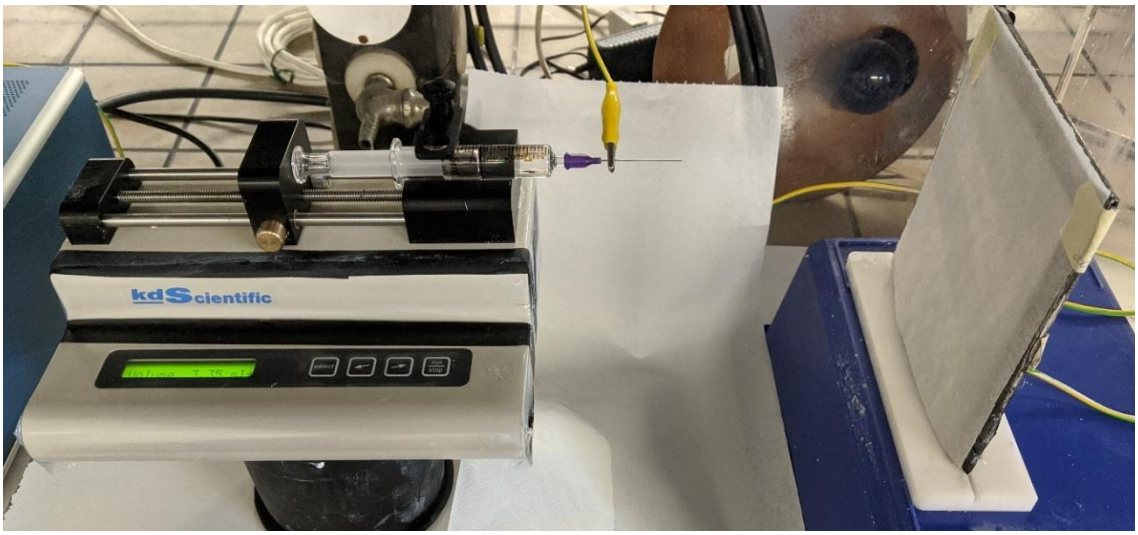

Figure 27 the syringe mounted on the top of the pump in the electrospinning setup.

2.2.2 *Transmission electron microscopy (TEM)*

Using TEM microscopy is possible to obtain extremely accurate images with a resolution of few nanometres. Exploiting the transmission of electrons through thin samples and their wave-nature is possible to tune the size of the electron beam using magnets as "magnetic lenses" to collimate the electrons on the sample or magnify the beam on the detector.

The sample was first dispersed in isopropyl alcohol and sonicated for 15 min. The solution is deposited on a perforated carbon film supported by a gold grid. The preparation was then dried at 80 °C. The Transmission Electron analyses were performed with a FEI TECNAI F20 microscope operating at 200 keV. The instrument is also equipped with Energy Dispersive X-ray Spectrometry (EDS) and the STEM accessory. The TEM images were taken in the phase contrast mode and Selected Area electron diffraction (SAED). STEM pictures were recorded using a High Angle Annular Dark Field (HAADF) detector.

2.2.3 *Surface area BET*

The instrument used to measure the surface area is a BET Fisons Sorpty 175. This technique uses the theory of BET (by the developers Brunauer, Emmett and Teller); the area is measured by determining the amount of gas of the monomolecular layer of nitrogen absorbed on the sample.

The amount of physically adsorbed gas on the sample is measured by the thermal conductivity difference of the gas before and after the absorption.

The most favourable conditions for the adsorption of a gas on the surface of the solid occur at the temperature of liquid nitrogen (77 K), so, the sample is pre-treated under vacuum at 120°C, in order to remove water or other volatile compounds, then the whole vial is submerged by liquid nitrogen and the measurement is carried out when it reaches the thermal equilibrium.

$$BET\ Surface = \frac{\frac{V_m}{V_0} \cdot N_A \cdot A_{N_2}}{g}$$

- V_0= molar volume of the gas
- N_a= Avogadro constant
- A_{N2}= diameter of the nitrogen molecule
- g= mass of the sample

2.2.4 *Diffuse reflectance spectroscopy (DRUV-vis)*

DRUV-VIS spectroscopy is a well-known technique used for both qualitative and quantitative measures. The spectrometer used is a Lambda-19 from Perkin Elmer and is equipped for both measure absorption and transmittance of liquid samples or reflectance measure on solid samples using an integrating sphere from Ulbricht.

2.2.5 *X-ray diffraction (XRD)*

All catalysts and supports were characterized by X-Ray Diffraction (XRD) analysis. Analyses were carried out at room temperature using a diffractometer Philips X'Pert X'Celerator and using the radiation from a Cu anode (emission wavelength Kα equal to 1,5718 nm). The acquisitions were made in increments of 0,050 °/s within the range of 20 e 80 2θ and 0,084°/s between 36 e 41 2θ.

Figure 28 outlines the main components of an X-ray diffractometer. When an X-ray is sent to a powder sample it is diffracted at different angles by the atoms forming in the crystalline structure of the soli. These diffracted rays create constructive or destructive interferences depending on which crystal planes they hit, but only the constructive interferences lead to a signal at the detector, every signal is reported at the diffraction angle it is detected.

We are able to understand the crystal structure of the sample Using Bragg's law, which relates distance between two crystal planes with the angle to have a detected signal using a fixed wavelength, the distance is unique for every crystal structure:

$$n \cdot \lambda = 2d\sin(\theta)$$

- n = positive integer number
- λ = wavelength of the incident wave
- θ = diffraction angle
- d = distance of two adjacent planes

This technique could be used to calculate the dimensions of the crystallites through the Scherrer equation:

$$\phi = \frac{k\lambda}{\beta \cos\theta}$$

- Φ is the average size of crystallites.
- K is the shape factor and is a dimensionless number.
- λ is the X-ray wavelength.
- β is the line broadening at half the maximum intensity (FWHM), after subtracting the instrumental line broadening in radians.
- ϑ is the Bragg angle of the centre of the peak.

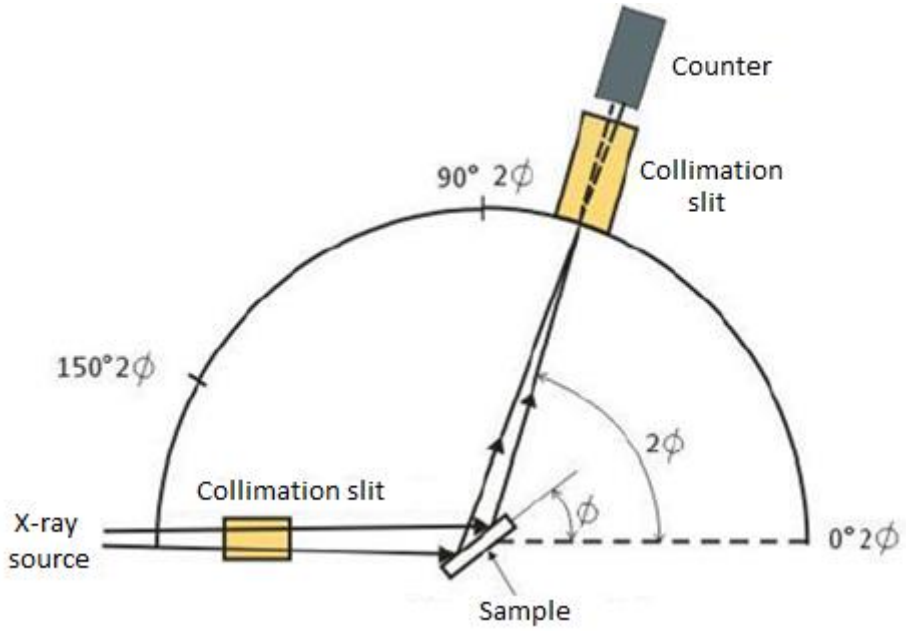

Figure 28: scheme of an XRD instrument

2.2.6 *Raman Spectroscopy*

Raman is a spectroscopic technique used to determine vibrational modes of molecules, it can provide local symmetry breaking and vibrational changes in the bonding pattern and molecular fingerprint. This technique relies upon the Raman scattering effect, that is the inelastic scattering of photons coming from a monochromatic source, typically a laser in the range Nir, visible or UV or an X-ray source.

When a monochromatic beam of light hits the surface of a solid, part of the radiation is diffused, with the three possible modes (Figure 29). Most of the light is scattered elastically: the system passes from a certain vibrational level of the fundamental electronic state to a higher energy level, but then falls almost instantly into the original vibrational level, emitting radiation with a wavelength equal to that of the original incident beam (Rayleigh scattering). A very small proportion of light can be inelastically diffused when the system passes to an excited state and then falls into a vibrational level different from the previous one: if the final vibrational level is higher than the initial one, a radiation with a wavelength greater than that of the incident beam is generated in the process (Raman scattering of Stokes type, or, if the final vibrational level is lower energy than the initial one a radiation is generated with a wavelength less than that of the incident beam (Raman scattering type anti-stokes). The reciprocal of the difference in wavenumber between the incident light and diffuse light by Raman effect is called "Raman shift" and is expressed in cm^{-1}, the original beam has a Raman shift equal to 0 cm^{-1}. The anti-stokes components are however less intense than the corresponding Stokes components, because at room temperature there are obviously few phonons that can be combined with incident photons; increasing the temperature the intensity of the anti-stokes components increases compared to that of the corresponding Stokes components.

When a sample is illuminated in a Raman spectrometer (Figure 30) with a laser beam the light from the illuminated spot is collected with a lens and sent through a monochromator. The elastically scattered radiation at the wavelength corresponding to the laser line is filtered out by either a notch filter, edge pass filter, or a bandpass filter, while the rest of the light reaches the detector. The Raman spectrometer used is a Renishaw Ramanscope 1000 instrument equipped with a Leica DMLM and the light source is a green laser with a wavelength equal to 514nm.

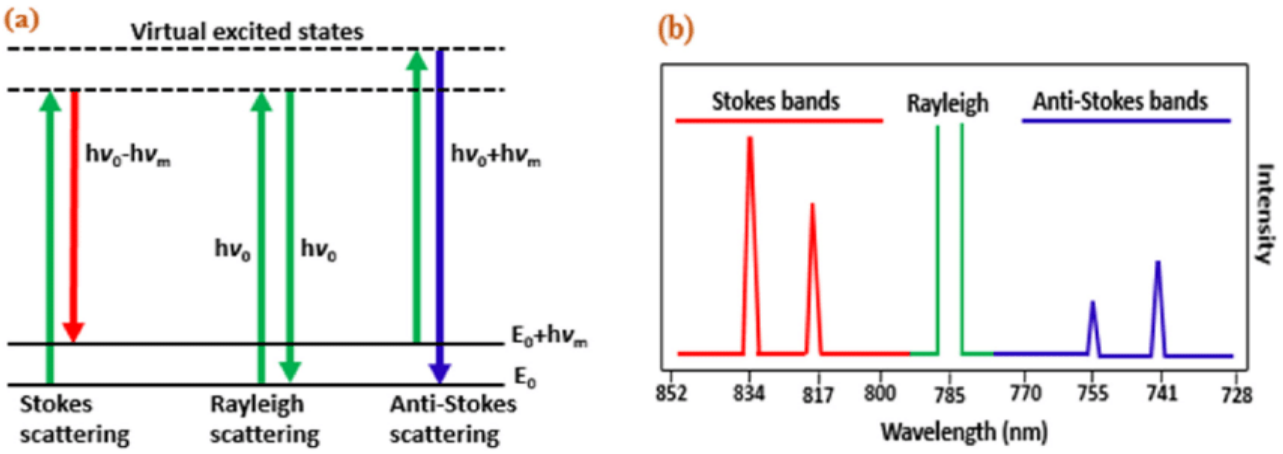

Figure 29: Scheme of the energy level involved in Raman scattering (a) and the resulting signals (b)

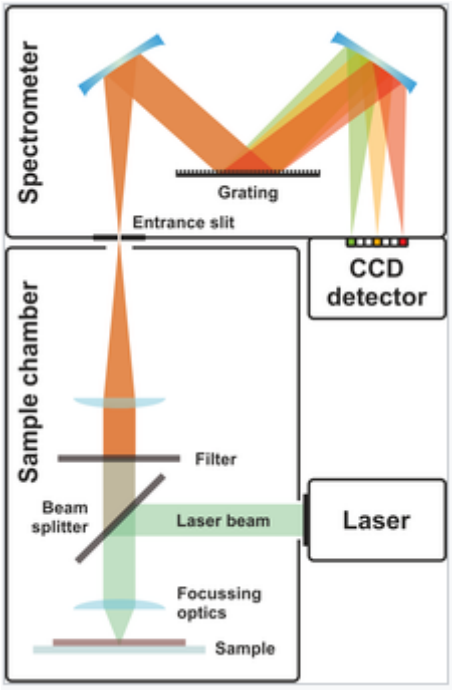

Figure 30: scheme of a Raman spectrometer

2.2.7 *Thermogravimetric analysis and differential thermal analysis (TGA/DTA)*

Thermogravimetric analysis (TGA) is a technique in which the mass of a sample is monitored against time or temperature during controlled heating with a precise heating ramp and in a controlled atmosphere (Figure 31). The instrument used was a TA instrument SDT Q 600. The resulting curve from the remaining mass of the sample against time or temperature can provide information regarding thermal stability or other changes in the sample structure, phase transitions, absorption/desorption phenomena, intermediate products formed and the composition of solid residue.

The Derivative Thermogravimetry (DTG) is the first derivative of a TGA analysis over time or temperature. In the majority of cases subsequent decomposition processes give overlapping decomposition stages, a certain decomposition reaction is not yet finished when the other one commences at a higher temperature. In most cases, a reliable qualitative and quantitative evaluation of the TG curve is impossible without having its first derivative DTG curve. The DTG curve is calculated fro the original DTA curve against time (-dm/dt) or temperature (-dm/dT).

The Differential thermal analysis (DTA) is a technique that measures the temperature difference between a sample and a thermally inert reference material while both the sample and the reference materials are subjected to the same controlled temperature program. This technique provides the heat flow involved in every changes or reaction that take place in the sample.

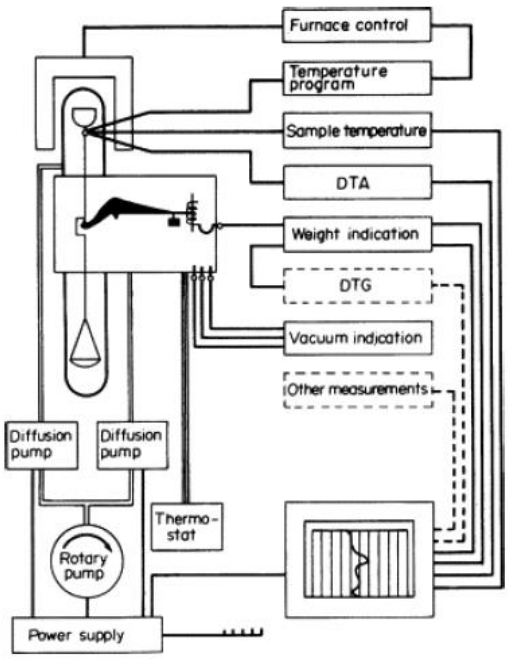

Figure 31: general scheme of a thermogravimetric instrument

2.2.8 *Attenuated total reflectance (ATR)*

ATR is an analytical technique that exploits the phenomenon of total internal reflection to recognise a chemical compound, its functional groups and its fingerprint absorbance or reflectance pattern, in liquid or solid samples without further preparation (Figure 32). Using a material with a higher reflective index, in order to collect the IR beam at the other side of the crystal, otherwise, the radiation would be absorbed by the sample. If the reflective index of the crystal is higher than the sample, an IR beam that enters from a side of the crystal can be reflected several times in it creating only an evanescent wave in the sample that penetrates between 0.5 and 2 µm and reach the sensor placed to the other side of the crystal. The ATR crystals usually are made of diamond, germanium, zinc selenide, or silicon. The ATR has been purchased from Bruker Alpha.

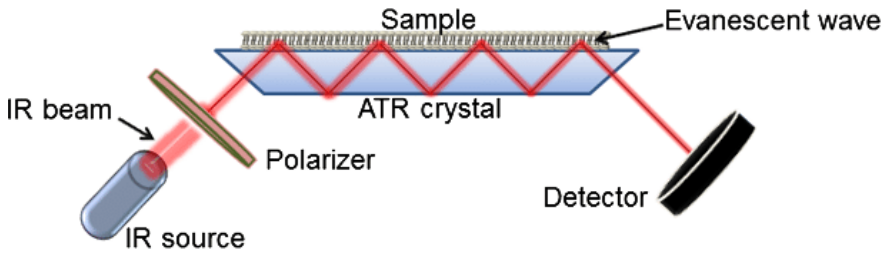

Figure 32: scheme of an ATR measure

2.2.9 *Scanning electron microscope (SEM)*

A SEM microscope can provide images of the surface of a sample with a high resolution, thanks to the interactions between the sample and the electrons generated by the thermionic effect from a tungsten cathode of an electron gun.

The samples need some preparation before being subjected to the high energy electron beam while placed in the vacuum chamber of the microscope, this preparation consists of cutting a small piece of the sample, placing it on an older with conductive adhesive and, if the sample is not conductive, coated with a conductive material such as a thin layer of noble metals. The SEM used is a FESEM Carl Zeiss Sigma NTS, GmbH Öberkochen, Germany.

2.2.10 *Reagents*

In Table 2 are shown the chemical reagents used during the project for the oxidation reaction experiments, the calibration curve solutions for HPLC and the preparation of the catalysts.

Chemical compound	Formula	Physical state	M.W. (g/mol)	Purity (%)	Supplier	Abbreviation used
Sodium hydroxide	NaOH	White pellets	39.99	>98	Sigma-Aldrich	-
5-(Hydroxymethyl)furan-2-carbaldehyde	$C_6H_6O_3$	White solid	126.11	99.99	AVA Biochem	HMF
5-Hydroxymethyl-2-furancarboxylic acid	$C_6H_6O_4$	White solid	142.11	99.99	Toronto Research Chemicals	HMFCA
Furan-2,5-dicarbaldehyde	$C_6H_4O_3$	Yellow solid	124.09	99.99	Toronto Reserch Chemicals	DFF
5-Formyl-2-furancarboxylic Acid	$C_6H_4O_4$	Grey solid	140.09	99.99	Toronto Reserch Chemicals	FFCA
Furan-2,5-dicarboxylic acid	$C_6H_4O_5$	Brown solid	156.093	99.99	Toronto Research Chemicals	FDCA
Tetrachlorauric acid trihydrate	$HAuCl_4 \cdot 3H_2O$	Yellow liquid	393.833	99.995	Sigma-Aldrich	-
Ethanol	C_2H_6O	Colourless liquid	46.069	99	FDCA	EtOH
Cerium nitrate hexahydrate	$Ce(NO_3)_3 \cdot 6H_2O$	White solid	326.13	99.995	Sigma-Aldrich	-
1-ethenylpyrrolidin-2-one	$(C_6H_9NO)_n$	White solid	$1,3*10^6$	99	Sigma-Aldrich	PVP
Cerium(IV) oxide	CeO_2	Yellow powder	172.115	99.95	Evonik	Low surface support or "CeO_2-C"
Cerium(IV) oxide	CeO_2	Yellow powder	172.115	99.95	Solvay	High surface support "CeO_2-HS"

Table 2: Chemical compound used.

2.2.11 *Reactor*

The reactor used for catalytic testing is a steel Parr autoclave 5500 series compact reactor. The body and the head of the steel reactor are joined with a Teflon gasket and kept closed by two screw clamps. The scheme of the reactor and the reactor are shown in Figure 33 and Figure 34.

A manometer, a rotor for agitation, a safety disc (V4), a pressure gauge, a thermocouple and three pin valves (V1, V2 and V3) are placed in the reactor head. V1 and V2 are equipped with a Swagelok connector, V1 serves as feed valve, it has been used to purge and to feed the reactor with oxygen. Both V1 and V2 are connected to the same dip tube in the reaction mixture.

The pressure gauge, the thermocouple and the rotor engine are electronically connected to a Parr 4848 reaction controller that serves both as pressure indicator, temperature controller and agitation controller. The heating is provided by a heating mantle which is connected with the controller that adjusts the heating depending on the temperature measured by the thermocouple.

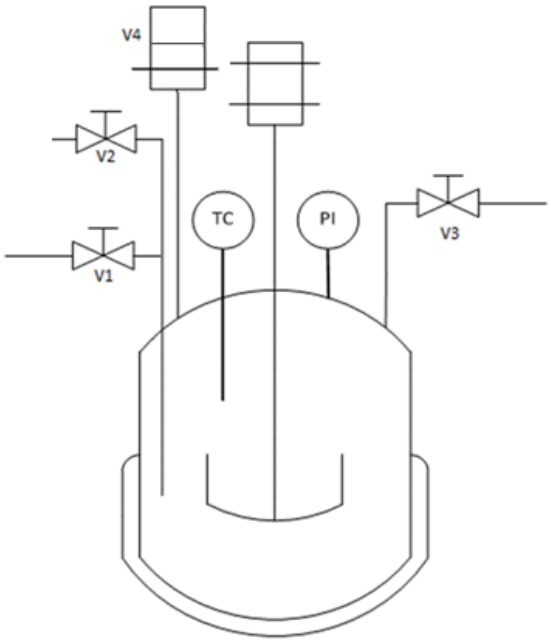

Figure 33: Scheme of the rector used in the project

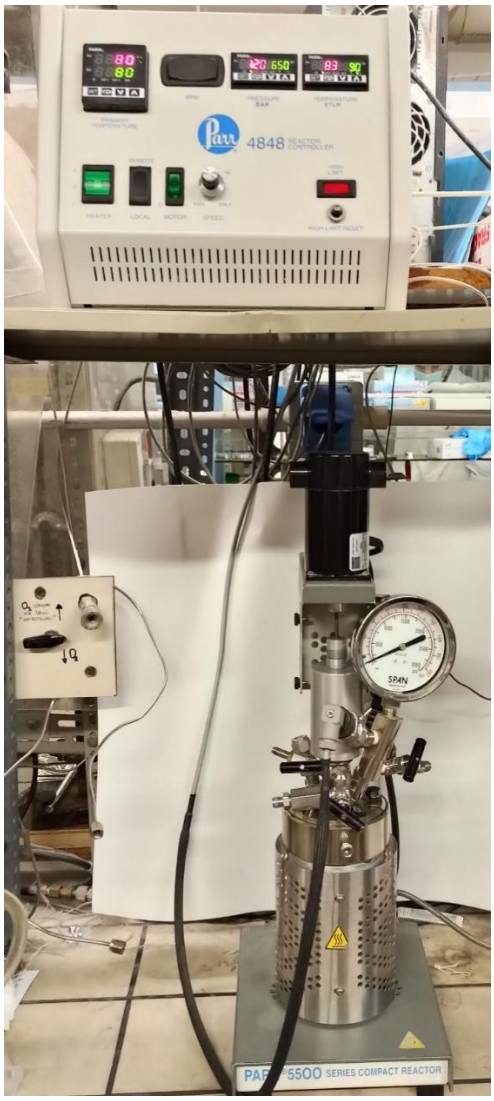

Figure 34: Photo of the reactor and the controller used (from the bottom to the top)

2.2.12 *Reaction procedure*

The reactions were performed in a batch reactor using 53 mg of catalyst, 55.5mg of HMF, 70.4 mg of NaOH and 25g of distilled water. The loading of the reactor was performed to minimize the contact time between NaOH and HMF. After the loading the reactor was sealed with two clamps and six screws, purged three times with oxygen and loaded with 10bars of oxygen. The reactor is then placed in a heating mantle and heated to the desired temperature. At the end of the reaction time the reactor is cooled in an iced bath, unloaded, and opened. The reaction mixture is then centrifugated for 15 minutes at 4500rpm to separate the solid catalyst, filtered with a syringe and diluted 1:10 to be analysed via HPLC.

2.2.13 *High-performance liquid chromatography (HPLC)*

HPLC is a widely used and well-known form of chromatography used in chemistry and analysis to separate, quantify organic compounds in a solution. This system relays on the different affinity of different components in a mixture to the stationary phase (a packed material contained in the chromatography column) and the mobile phase (the solvent used in the process), in order to separate them at different reaction time at the end of the column. The flow of solvent that carries a small volume of sample is pushed in the column by a pump, at the end of the column are present one or more detectors to identify and measure the amount of the different analytes.

The chromatographic analysis have been carried out in an Agilent Technologies 1260 Infinity with an autosampler device. The column used was a BioRAD AMINEX HPX 87H (300 x 7.8mm).

The analysis were performed injecting 5µL of the sample into the mobile phase: a solution of ultra-pure water and sulphuric acid 5mM with a flow of 0.5 mL/min, while the stationary phase was made of styrene-divinylbenzene resin with a porous structure able to separate the molecules according to their hydrodynamic size. The resin was also functionalized with an 8% link H+ to further separate the molecules thanks to an ion-exchange mechanism. A Diode Array Detector (DAD) was used as detector at the wavelength: 251, 264 and 284nm. An example of chromatograph is reported in Figure 35 and a resume of the retention times and the intensity used for the analysis of each species is reported in Table 3. As is possible to notice from Figure 35, the different species have different response factors at different wavelengths, so the response factors were calculated accordingly during calibration. The information reported from

HPLC analysis has been used to calculate the HMF conversion, the yields in the products and the carbon loss for each reaction performed.

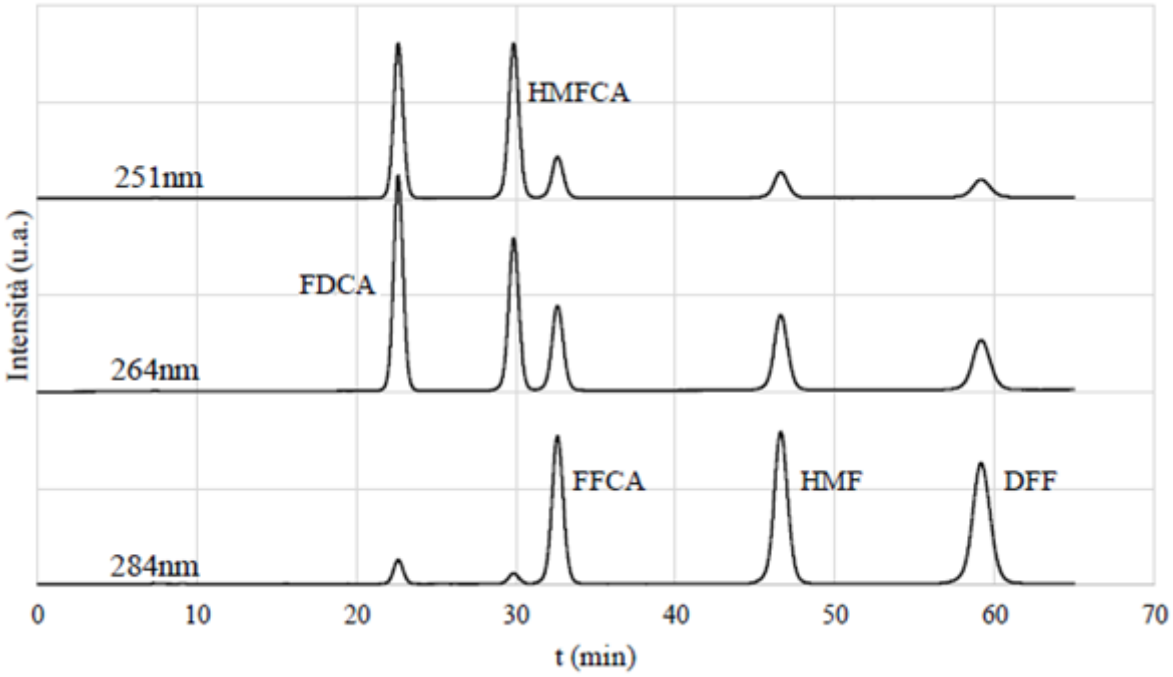

Figure 35: Chromatogram of a mixture of HMF and its oxidation products

Chemical specie	t_R (min)	λ (nm)
HMF	46	284
DFF	60	284
HMFCA	30	251
FFCA	32.5	284
FDCA	22.5	264

Table 3: Retention times and wavelengths used for each species analysed

Not all the post-reaction mixtures were injectable in the HPLC, in alkaline solution HMF tends to form insoluble humins with a brownish colour. A high concentration of humins in the solution could obstruct the chromatographic column. Every solution was judge visually before the injection to decide whether or not it could be injected. An example of degradation of HMF over time is reported in Figure 36.

Figure 36: Degradation of HMF on time in presence of sodium hydroxide, from 0 min on the left vial to 10 min of reaction on the right vial

2.2.14 *Data analysis of post-reaction mixtures*

Here have been reported the formula used to analyse the HPLC data of the post-reaction mixture:

$$Conversion\ (X_A) = \frac{n_{A,IN} - n_{A,OUT}}{n_{A,ouT}} x100$$

$$Yield\ (Y_B) = \frac{n_{B/coeff}}{n_{A,IN/Coeff}} x100$$

$$Selectivity\ (S_B) = \frac{n_{A,IN} - n_{A,OUT}}{n_{A,ouT}} x100$$

$$Carbon\ Loss = 100 - \sum_{i=1}^{n} S_n$$

3 Results and discussion

Cerium oxide is an interesting material for catalyst production for its availability, its excellent catalytic properties are given by its store oxygen capacity (OSC), which depends on the number of reticular defects present on the surface. Different morphologies expose different reticular planes, and different reticular planes can expose different amounts of defects. The preparation method of the cerium oxide can influence the surface area, morphology, and the number of defects in the sample. In particular, ceria nanostructures with high aspect-ratio seem to have high activity capabilities.[3–7]

This research aims to synthesize, characterise, and test on the oxidation of HMF to FDCA a range of gold nanoparticles supported on electrospun ceria nanofibers catalysts, to investigate the link between the preparation method, the obtained morphology, and the activity of the catalysts. In order to assess the catalytic properties of gold on ceria systems, different gold-based catalysts were prepared starting from different supports: commercial ceria powders, electro-spun ceria nanofibers with and without gold precursors and undergoing different thermal treatments (pyrolysis and calcination).

In order to assess the catalytic properties of gold on ceria systems, different gold-based catalysts were prepared starting from different supports: commercial ceria in grain, ceria electro-spun nanofibers with and without gold precursors and followed by different heating treatment (pyrolysis and calcination). These systems have been used for comparison with the nanofibers sample in the different characterizations and the oxidation reaction of HMF to FDCA (Figure 37[8]).

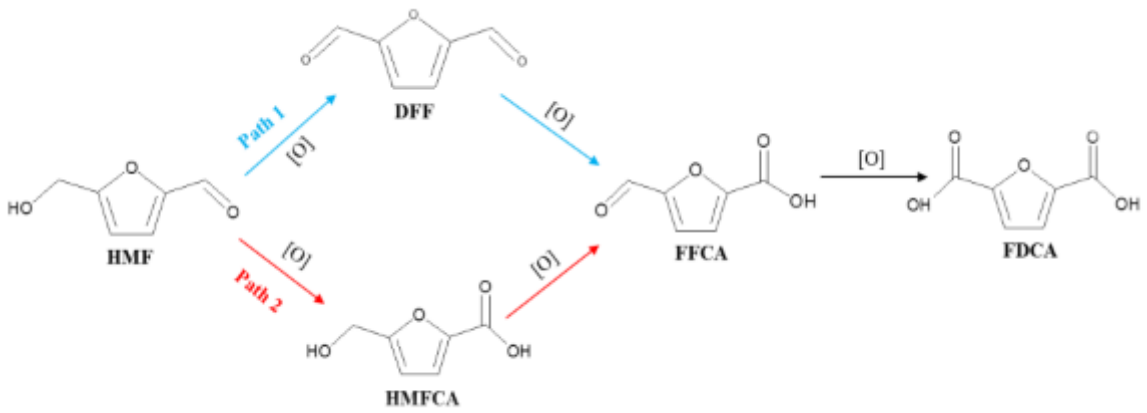

Figure 37: reaction path for the oxidation of HMF to FDCA

The synthesis has been followed by different characterizations on the materials: SEM, TEM, XRD, ATR, TGA, BET, DRUV-VIS and Raman analysis. The results are reported in the following chapters.
The samples prepared and tested are listed in Table 4 with the results of the Brunauer – Emmett – Teller (BET) analysis. The BET method was used to measure the surface area of the samples of supports and catalysts. All the preparations described in sections 2.1 and 3.3 are resumed in Figure 38 and Table 4.

The commercial supports used are ceria Evonik Degussa Gmbh and Solvay Rhodia Actalys HSA5, these supports have respectively low and high surface area, as reported from BET analysis in Table 4, the preparations are resumed in Figure 38. The catalysts supported on the Evonik Degussa Gmbh ceria have been labelled "Au/CeO_2 -C" while the catalyst supported on Ceria Solvay Rhodia Actalys HSA5 have been labelled "Au/CeO_2 -HS" ("high surface").

The spun nanofibers have been subjected to different calcination process in order to obtain the desired oxidic phase before the DP process. The heat treatment in air to obtain the fibres was more gently, with a ramp of 0.2°C/min and a isotherm maintenance at 300°C or 550°C for three hours, this was meant to not compromise the nanofibers structure during the PVP combustion.[1] The sample of nanofibers supports obtained have been labelled CeO_2-NF_300 or CeO_2-NF_550 depending on the temperature chosen for the isotherm maintenance. Gold-containing samples of catalysts obtained after DP have been called "Au/CeO_2-NF _300" or "Au/CeO_2-NF_550".

Two more catalyst samples have been obtained adding the $HAuCl_4$ in the spinning solution. The sample labelled "Au/CeO_2-NF_C" has been obtained calcinating in air the spun fibres at 300°C, while the sample "Au/CeO_2-NF_PC" has been prepared by subjecting the fibres first to a thermal treatment in N_2 at 300°C and then to calcination in air at 300°C. All Au-containing samples have a content of metal of 1.5% (wt./wt.) over the support.

As reported in Table 4, the different heat treatment on the nanofiber samples had a strong influence on the surface area, in particular, is possible to notice Ostwald ripening after calcinating the sample at 550°C, which caused a marked diminishing in the surface area value of the sample. Despite the strong influence on the calcination temperature on the nanofibers, no relevant changes in the surface area have been detect in both the commercial ceria caused by the calcination treatment at 300°C and 550°C, probably, during their industrial production, these commercial ceria have already been subjected to calcination. No relevant changes in the surface area have been detected before and after the DP process.

Support	Sample	Surface area [m^2/g]	Notes:
Ceria Evonik Degussa GmbH	CeO_2 -C	45	Commercial ceria support, low surface
	CeO_2 -C_300	44	Commercial ceria support, low surface, calcined at 300°C
	CeO_2 -C_550	50	Commercial ceria support, low surface, calcined at 550°C
	Au/CeO_2-C	46	Au supported on low surface commercial ceria, synthesised via DP, calcined at 300C°
Ceria Solvay Rhodia Actalys HSA5	CeO_2 -HS	150	Commercial ceria support, high surface
	CeO_2 -HS_300	140	Commercial ceria support, high surface calcined at 300°C
	CeO_2 -HS_550	160	Commercial ceria support, high surface, calcined at 550°C
	Au/CeO_2 -HS	140	Au supported on high surface commercial ceria, synthesised via DP, calcined at 300C°
Electrospun nanofibers	CeO_2 -NF_300	83	Ceria nanofiber support, calcined at 300°C
	CeO_2 -NF_550	21	Ceria nanofiber support, calcined at 550°C
	Au/CeO_2-NF _300	77	Au supported on nanofiber support calcined at 300°C, synthesised via DP
	Au/CeO_2-NF _550	29	Au supported on nanofiber support calcined at 550°C, synthesised via DP
Electrospun nanofibers (spun with chloroauric acid)	Au/CeO_2-NF _C	76	Prepared by electrospinning using a solution containing HAuCl4 and calcinating the fibres at 300°C in air
	Au/CeO_2-NF _P	N/A	Prepared by electrospinning using a solution containing $HAuCl_4$ followed by thermal treatment at 300°C in N_2
	Au/CeO_2NF_PC	96	Prepared by electrospinning using a solution containing $HAuCl_4$ followed by thermal treatment at 300°C in N_2 and calcination in air at 300°C

Table 4: Surface area and data of catalysts and supports tested

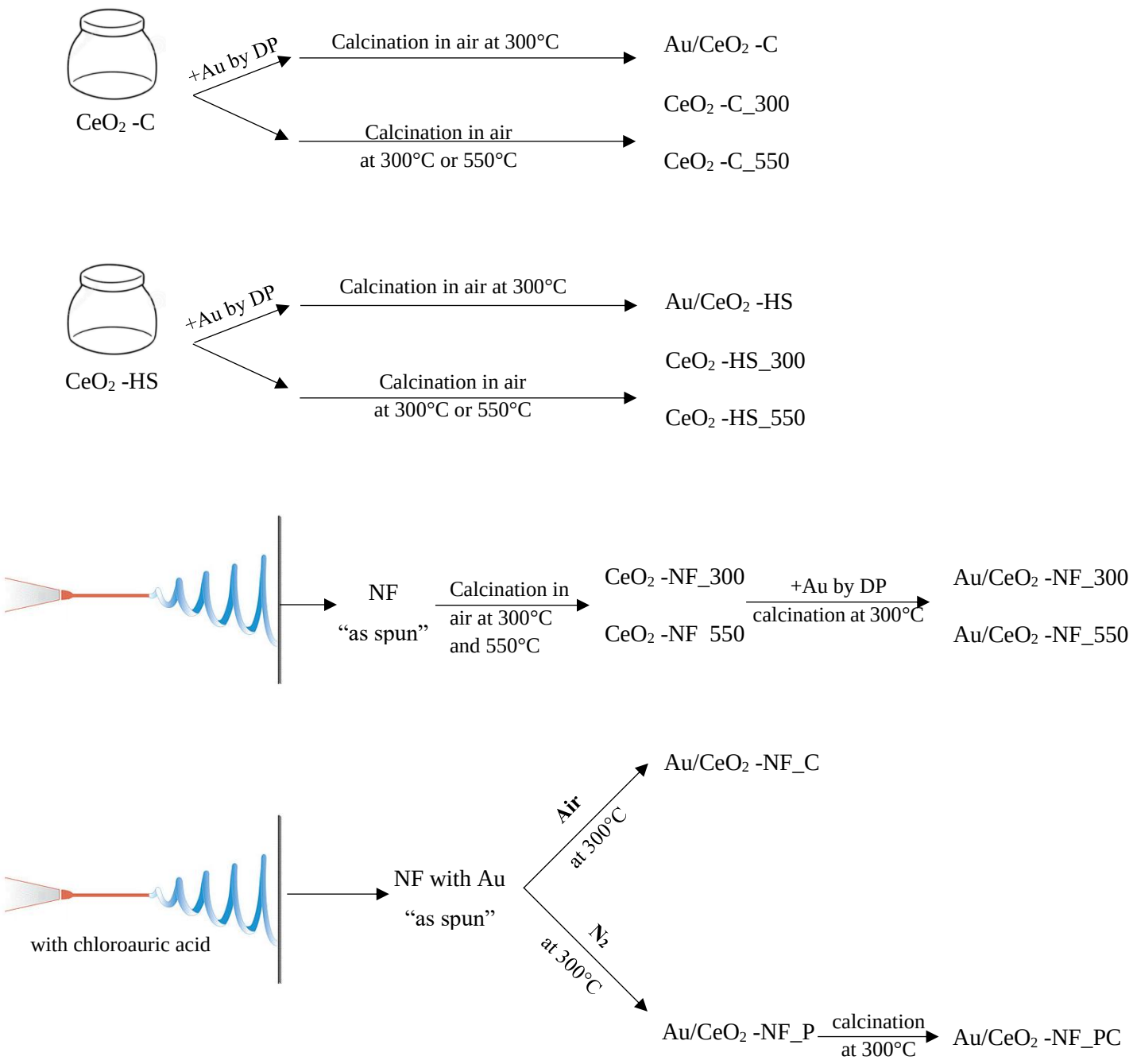

Figure 38: Resume of the preparations of the catalysts

3.1 Study of catalyst based on commercial ceria ("CeO_2-C")

3.1.1 *XRD analysis of CeO_2-C samples*

The XRD analysis on CeO_2 support samples calcined at 300°C and 550°C and on Au/CeO_2-C sample (Figure 39) show the characteristic peaks of the fluorite-type structure of crystalline ceria, in particular, the peaks at 29, 33, 47.5, 57 and 59 *2θ* are given respectively by the crystalline orientation planes: (111), (200), (220), (311) and (222). The least intense peaks at 59, 70 and 76 *2θ* are given respectively by the crystalline planes (400), (331) and (420), which are less exposed by the samples,[9–12] peaks of other possible impurities have not been detected.

The correspondent peaks of the different samples have comparable relative intensities, it can therefore be deduced that the calcination at 300°C or 550°C and the DP procedure on the commercial supports do not significantly affect the crystalline structure of the samples.

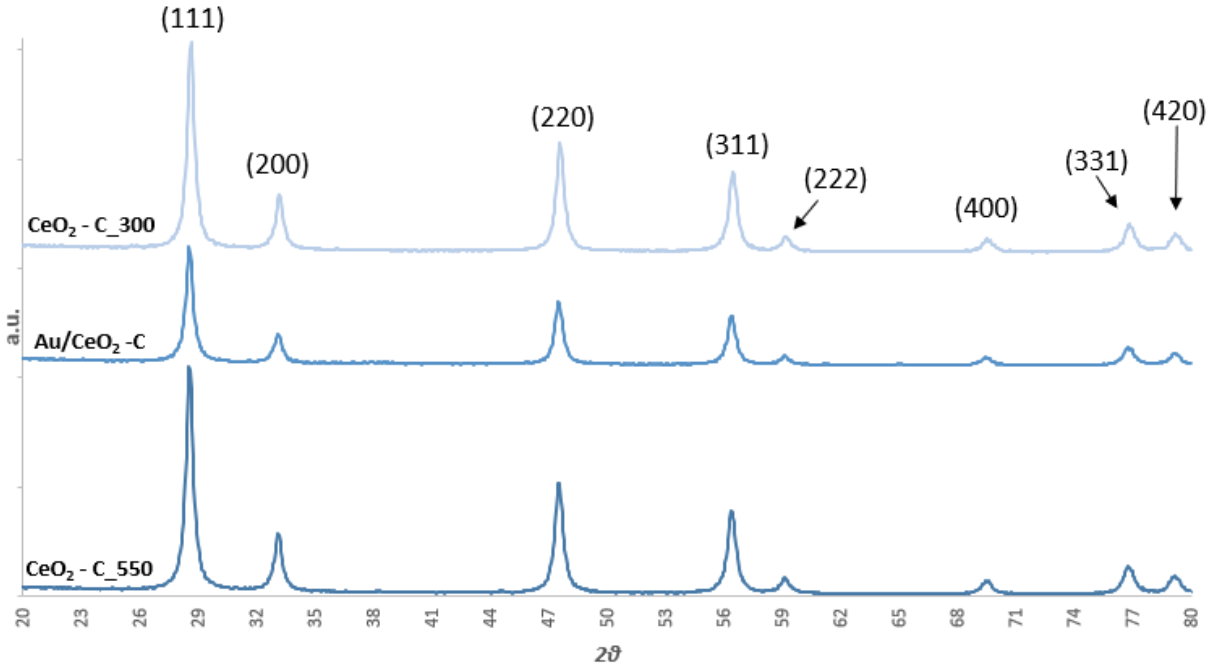

Figure 39: XRD pattern comparison of commercial CeO_2- C based samples

The average size of the crystallites has been calculated through the Scherrer equation for all the different planes (Figure 40) and is average value is 19nm, there is no preferential growing in the reticular planes exposed, both this evidence and the absence of relevant changing in the surface area with the calcination, suggest that the commercial CeO2-C ceria have already been calcined during its industrial production.

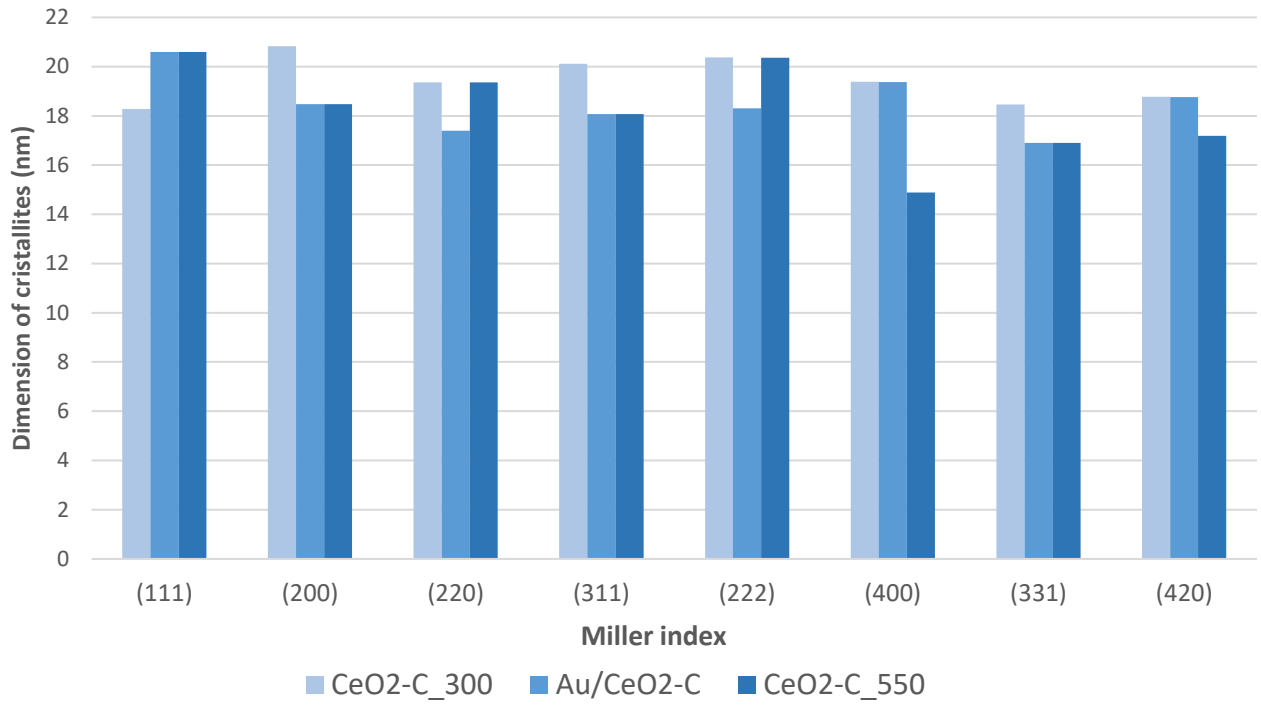

Figure 40: dimensions of crystallites for CeO_2-C based samples

Comparing the relative intensities of the XRD peaks of a sample with the relative intensities of a tabulated reference (code: 00-043-1002) could highlight crystal faces that are preferentially exposed. No remarkable differences have been noted in the difference between the relative intensities of the CeO_2-C peaks and the tabulated ones (Figure 41), the main differences are in the peaks (220) and (311), which are slightly under-exposed. The smallest different have been recorded in the sample CeO_2_550, the one calcined at the highest temperature, which shows a difference in this peak of only 2%.

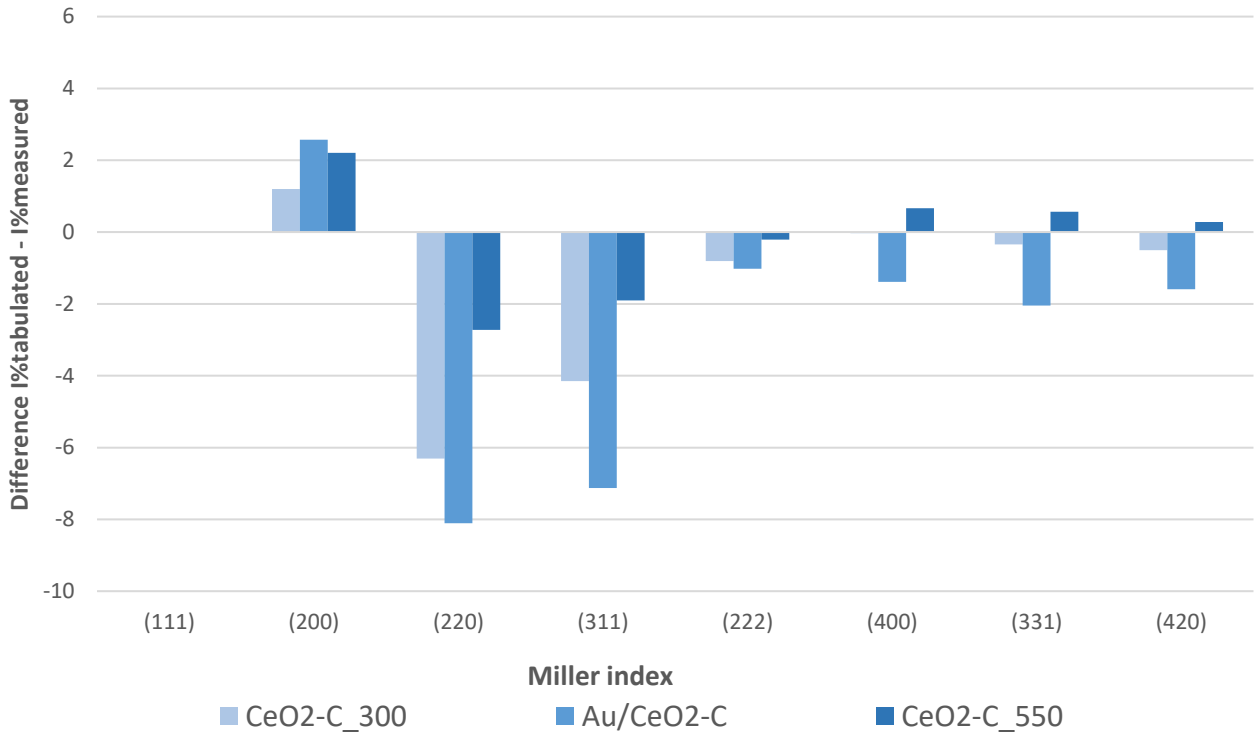

Figure 41: Differences between tabulated relative intensities of ceria XRD peaks and peaks for CeO_2-C based samples (tabulated intensities reference code: 00-043-1002)

A further XRD analysis was carried out in the range 36 - 41 2θ on the catalyst sample Au/CeO_2-C, indeed the diffraction peak of the plane (111) of the gold nanoparticles can be detected in this range[13] (Figure 42). The estimated average diameter of the Au nanoparticles has been calculated through the Scherrer equation and is equal to 6nm.

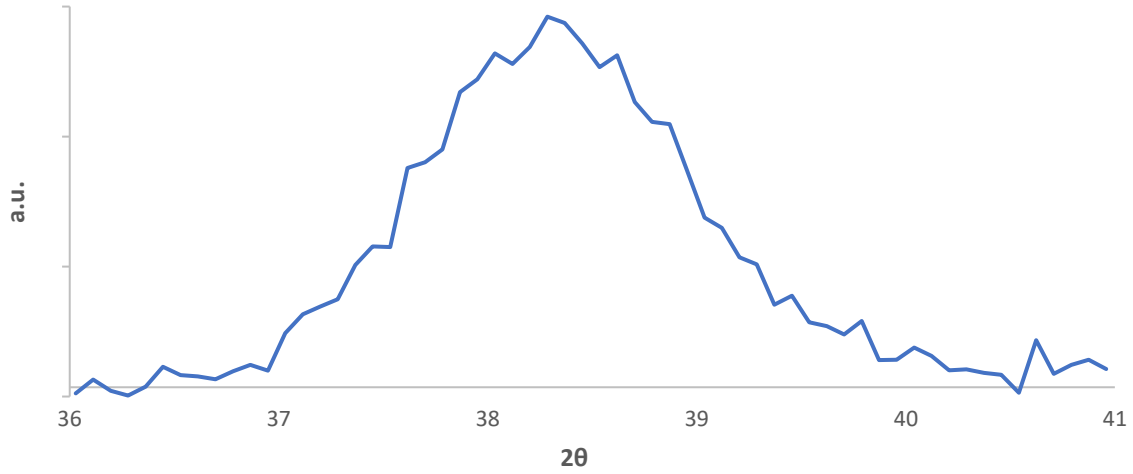

Figure 42: XRD between 36 and 41 2θ of sample Au/CeO_2-C

3.1.2 *Raman analysis of CeO_2-C samples*

Raman spectra of ceria and catalyst samples were performed with a green laser at 514nm. Several peaks are visible in the Raman spectra of the ceria at 258 cm^{-1}, 462 cm^{-1}, 595 cm^{-1} and 1180 cm^{-1}. The most intense peak is at 462 cm^{-1} and is characteristic of cerium oxide, it is due to symmetrical stretching F_{2g} of O-Ce-O bonds in the fluorite-like structure of ceria, the peaks at 258 cm^{-1} and 1180 cm^{-1} are peaks given by second-order harmonics, due to a transverse acoustic vibrational mode called 2TA and a longitudinal optical vibrational mode called 2LO respectively, these three peaks are characteristic of the cerium oxide. The signal at 595 cm^{-1} is the defect-induced band (often called "D-band"), this band is particularly interesting because it depends on defects in the crystalline structure (characteristic peaks of the commercial low surface sample highlighted in Figure 43)[13–17].

A Raman analysis in UV could provide quantitative information on the defectiveness of the sample before and after calcination, since the ratio between the intensity of the D-band and that of the peak at 462 cm-1 would result in a value proportional to the concentration of defects in the sample, due to multiphonon excitation effects14,16,17.

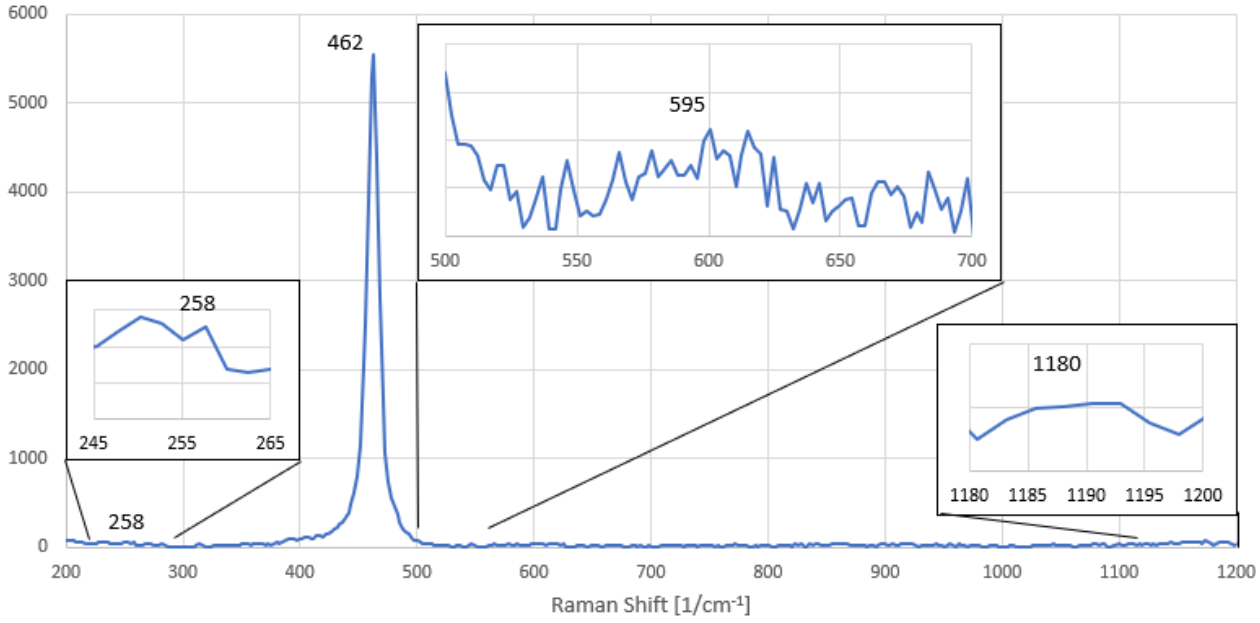

Figure 43: Raman spectrum of commercial ceria Evonik Degussa Gmbh "Ceo2-C", characteristic peaks of ceria highlighted

The support CeO_2-C as bought, calcined at 300°C, 550°C and subjected to DP to synthesize the Au/CeO_2-C sample, clearly shows at the Raman the main peak of the oxide cerium and very weakly the two secondary peaks 2TA and 2LO (Figure 44). The main difference between the

spectra is the slight shift to low cm^{-1} to the main peak in the sample Au/CeO_2-C, this shift is due to the presence of gold[14], the D-band is visible only in the sample Au/CeO_2-C, and it is probably due only to the strong fluorescence of the sample which is clearly visible also in the rest of the spectrum and It was not possible to correct it completely.

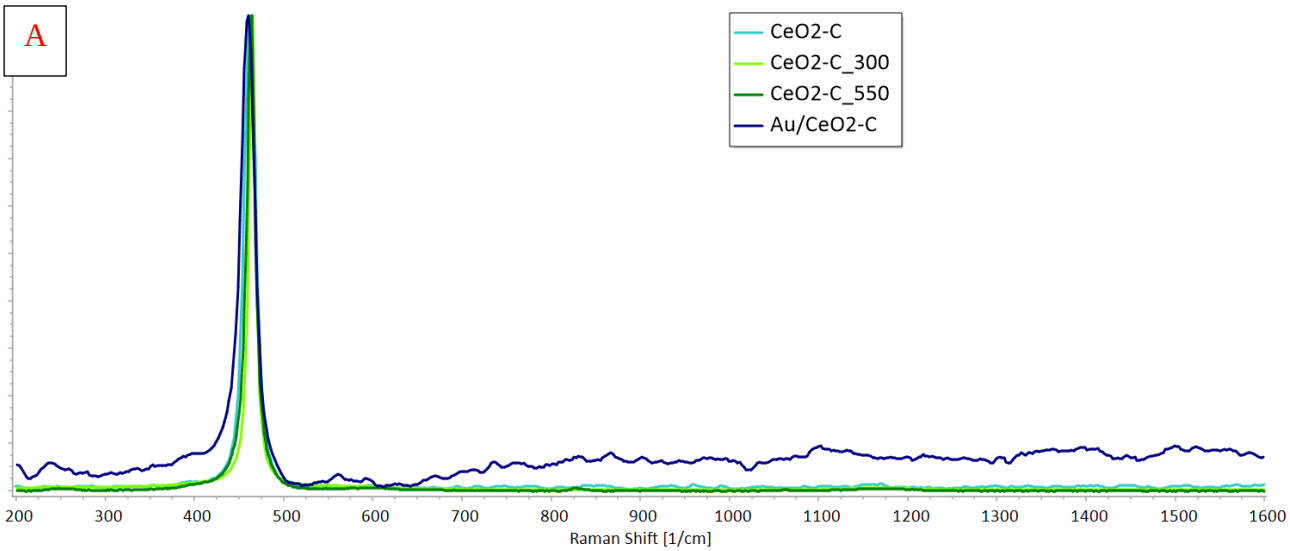

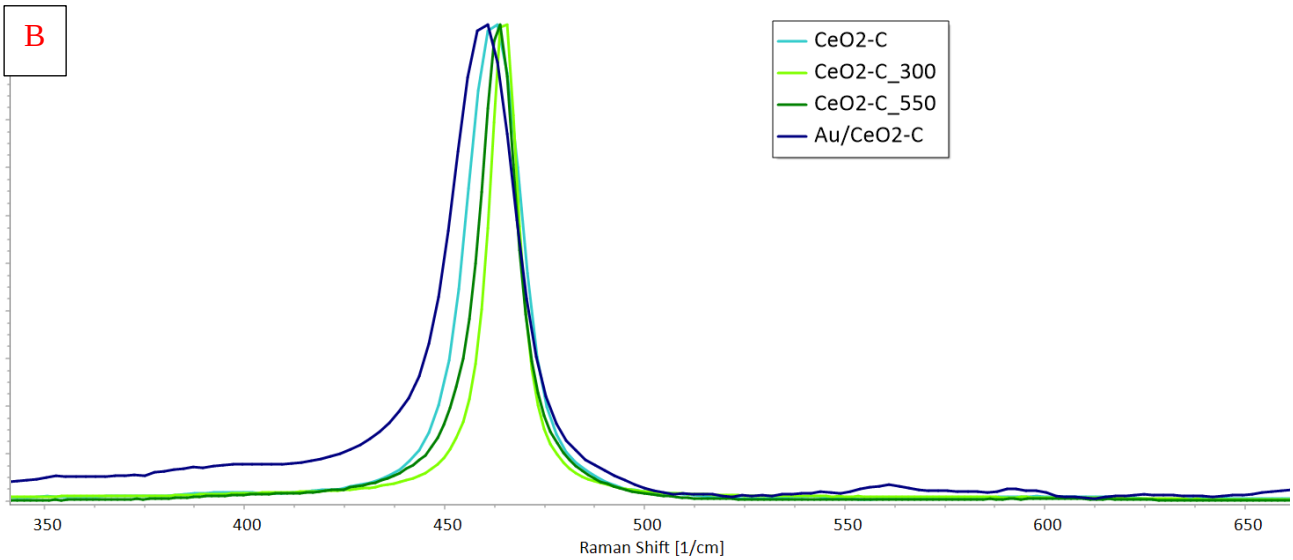

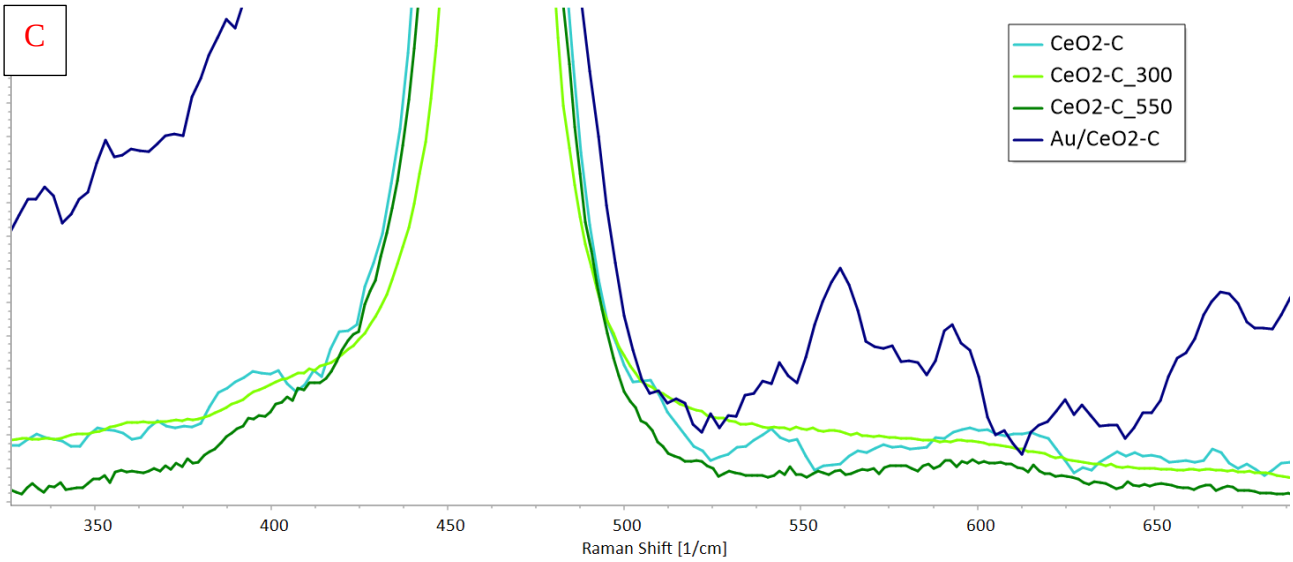

Figure 44: Raman spectra six Ceo2-C samples: complete spectra from 200 to 1600 cm^{-1} (A), zoom between 350 and 650 cm^{-1} (B) and on the D-band region (C)

3.1.3 *DRUV-Vis analysis of CeO_2-C samples*

Cerium oxide without any dopant agent exhibits three different absorption bands at 235, 277 and 325nm, these absorptions correspond to $Ce^{3+} \leftarrow O^{2-}$ charge transfer, electron transition $Ce^{4+} \leftarrow O^{2-}$ from the valence band to the conduction band, from orbital 2p of oxygen to 4f of cerium, and an interband transitions.[6,18,19]

The bands at 235 and 277nm are particularly interesting because they can be associated with the intrinsic defectiveness of ceria support, the first band is proportional to the presence of Ce^{3+} ions, the second one to Ce^{4+} ions. Since they are related, the highest is the absorption related to Ce^{3+} ions, the lower is the one due to Ce^{4+} ions in the support. The DRUV-Vis analysis of commercial samples are reported in Figure 45 and Figure 46, however, is not possible to notice relevant differences in the defectiveness of the commercial CeO_2-C samples in the bands at 235 and 277nm (Figure 46).

From the DRUV-Vis analysis, it is possible to observe the surface plasmonic resonance band characteristic of gold nanoparticles too. The band centred around 560nm and can provide, for comparison, information on both the size and dimensional polydispersity of gold nanoparticles.[6,18,20,21] This band will be used in the further chapters for the comparisons with the other samples.

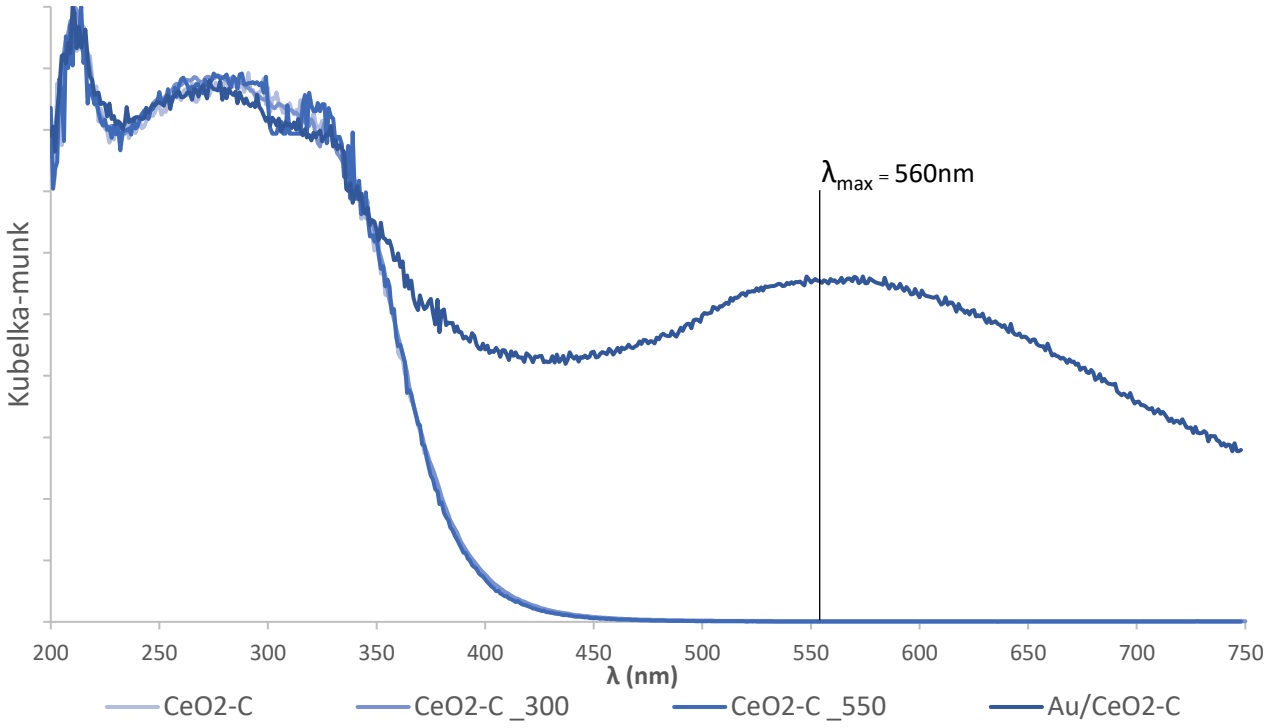

Figure 45: DRUV-Vis on CeO_2-C samples

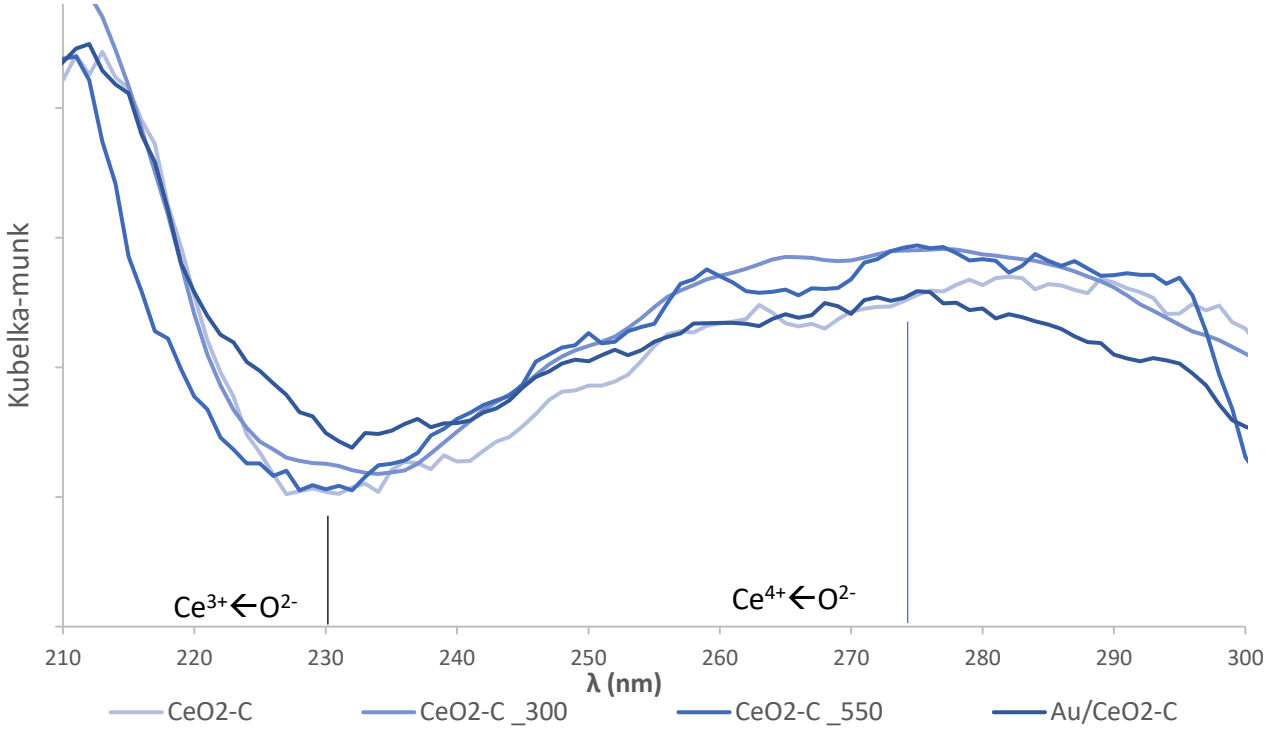

Figure 46: DRUV-Vis on CeO_2-C samples, between 210 and 300nm

3.1.4 *Catalytic tests on CeO_2-C samples*

The results for the catalytic test at 70°C for commercial low surface sample are reported over time in the following Table 5 and Figure 47 and compared to the reaction blanks in the same condition. The two reaction blanks were performed in the same conditions, 4 hours of reaction time and using the same reagents, one without any solid phase and the second one with the calcined support without gold particles. Both the blanks show comparable results, with an almost completely decomposition of HMF and a very small formation of oxidation products. The colours of the two post-reaction solution was a cloudy dark brown, this and the high carbon loss are due to humins and heavy products formed by parasitic reactions on HMF.[22] The presence of Au in the catalyst changed the reaction performance completely, leading to complete conversion of HMF and a high formation of HMFCA and FDCA. The yield of FDCA was growing with reaction time from 20% yield after one hour of reaction to 67% after 4 hours. The carbon loss was almost negligible and equal to 10% only after 1 hour. No carbon loss was recorded at a higher reaction time.

These results, in accordance with the literature[23], show the pattern of the consecutive reaction of the oxidation of HMF to FDCA: almost no HMF is detected in the post-reaction solution with catalyst. The HMFCA is detected instead because the oxidation of its alcohol group is the rate-determining step of the process[23]. Almost all the FFCA produced after this step is converted into FDCA, the final product of the reaction chain. No DFF has been detected because its formation is disfavoured in alkaline solutions.[10,23]

time (h)	X HMF (%)	Y HMFCA (%)	Y FFCA (%)	Y FDCA (%)	Carbon Loss (%)	Notes:
4	94	28	6	4	57	Blank reaction, in absence of any support or catalyst
4	91	19	3	2	67	Blank reaction, in presence of CeO_2-C calcined at 300°C (CeO_2-C_300)
1	100	68	2	20	10	
2	100	59	0	41	0	
4	100	32	1	67	0	

Table 5: Catalytic test results over time of the Au/CeO_2-C catalyst, conditions: HMF: NaOH 1:4, 70 °C

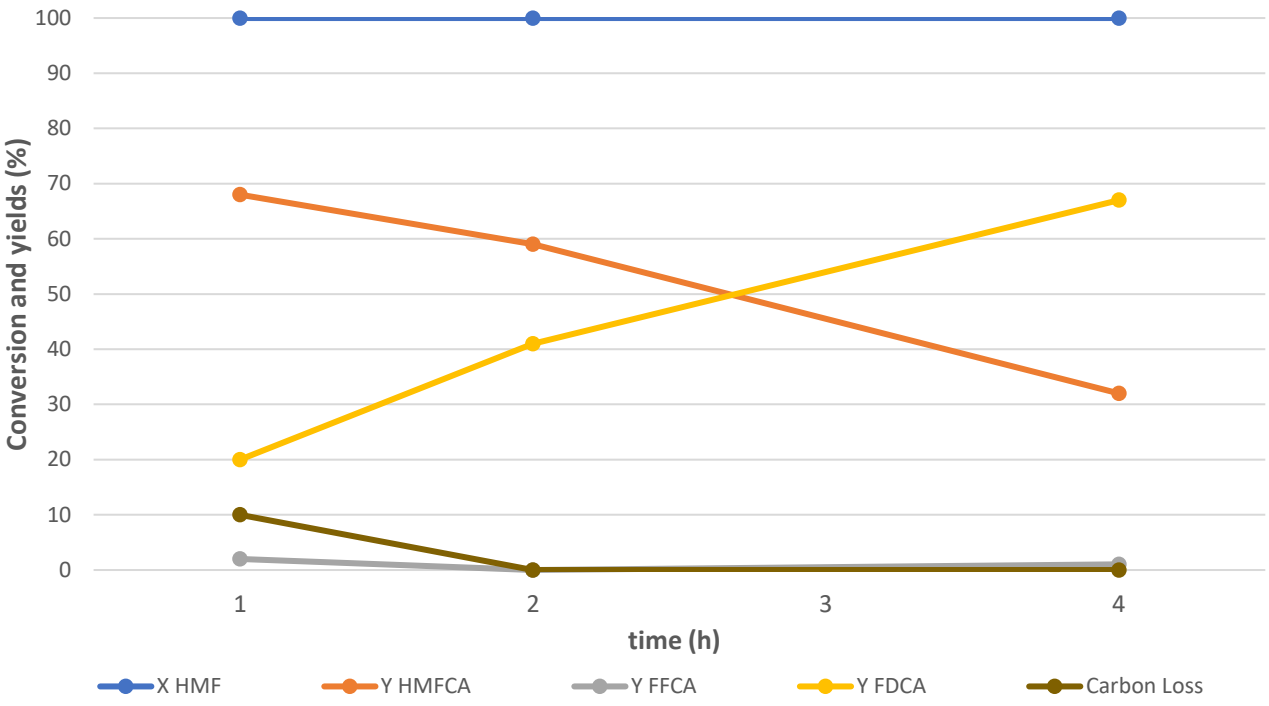

Figure 47: Conversion and products yields over time for the Au/CeO_2-C catalyst, T= 70 °C

In Table 6 and Figure 48 are reported the results for the reaction with the same catalyst at 80°C against reaction time. These results show the same pattern previously obtained for the reactions performed at 70°C, but with a greater yield in FCDCA, the final product of the oxidation, so the temperature has a positive influence on the reaction rate in the desired products. The carbon loss seems to not be influenced by the temperature change.

time (h)	X HMF (%)	Y HMFCA (%)	Y FFCA (%)	Y FDCA (%)	Carbon Loss (%)
1	100	70	2	18	10
2	100	35	0	65	0
4	100	3	0	96	1

Table 6: Catalytic test results over time of the Au/CeO_2-C catalyst, conditions: HMF: NaOH 1:4, 80 °C

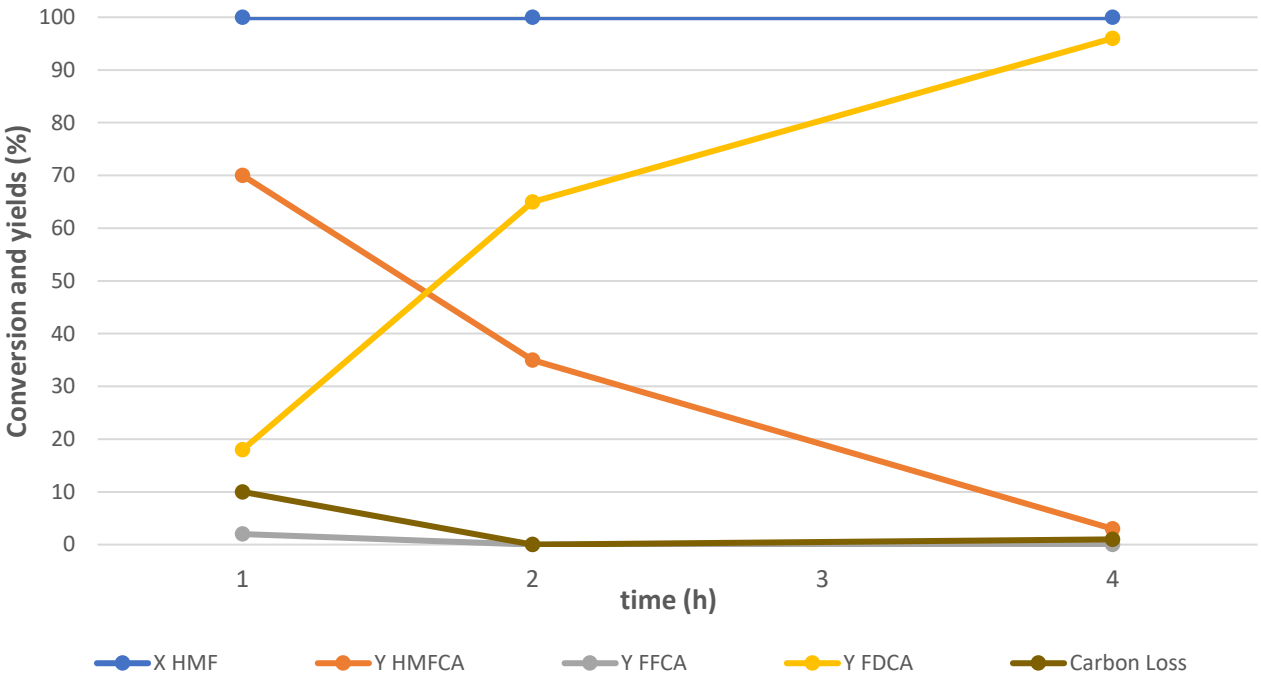

Figure 48: Conversion and products over time for the Au/CeO_2-C catalyst, T= 80 °C

3.2 Study of catalyst based on commercial ceria ("CeO_2-HS")

3.2.1 *XRD analysis of CeO_2-HS samples*

The characteristic peaks of ceria have been recorded in the samples supported on high surface ceria via XRD analysis (Figure 49). The peaks of the high surface support are shown to be particularly widened compared to those of the commercial support, the widening is particularly noticeable in the adjacent peaks at 56.2 and 59.1 and at 76.7 and 79.1 *2θ*, which are partially overlapped.

The widening is due to the smaller size of the crystallites, which have been calculated through the Scherrer equation and have an average size of 5 nanometres versus the 18nm average size of the samples CeO_2-C; the smaller dimension of the crystallites is the cause of the high surface area of the samples CeO_2-HS.

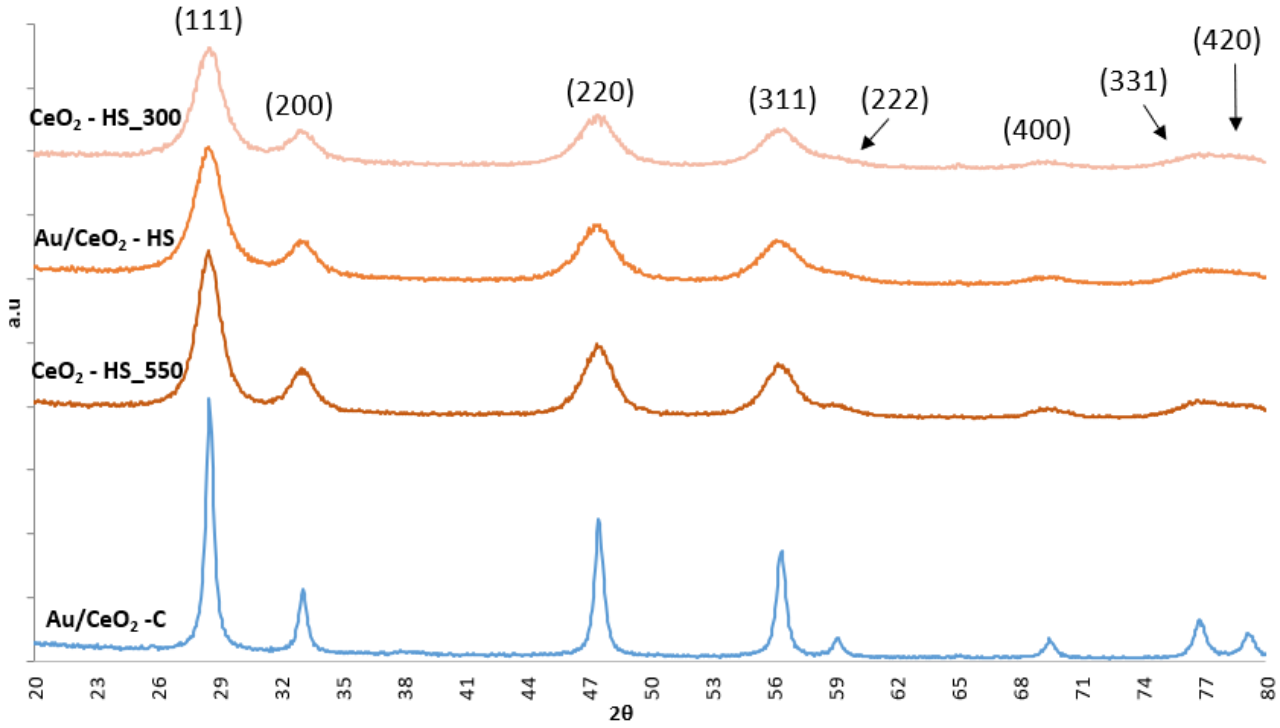

Figure 49: XRD pattern comparison of CeO_2 samples based on high area commercial

The Scherrer equation has been used to calculate the dimension of the crystallites for each XRD peak to highlight possible preferential growing on the crystal planes (Scherrer results in Figure 50). No preferential growing has been detected, is possible to notice that the crystallites of the samples CeO_2-HS_550 are slightly bigger, this is due to Ostwald ripening caused by the higher

calcination temperature of the sample. The lack of the results at 79.2 *2θ* for the samples CeO_2-HS_300 and Au/ CeO_2-HS are only artefacts due to the peak overlapping.

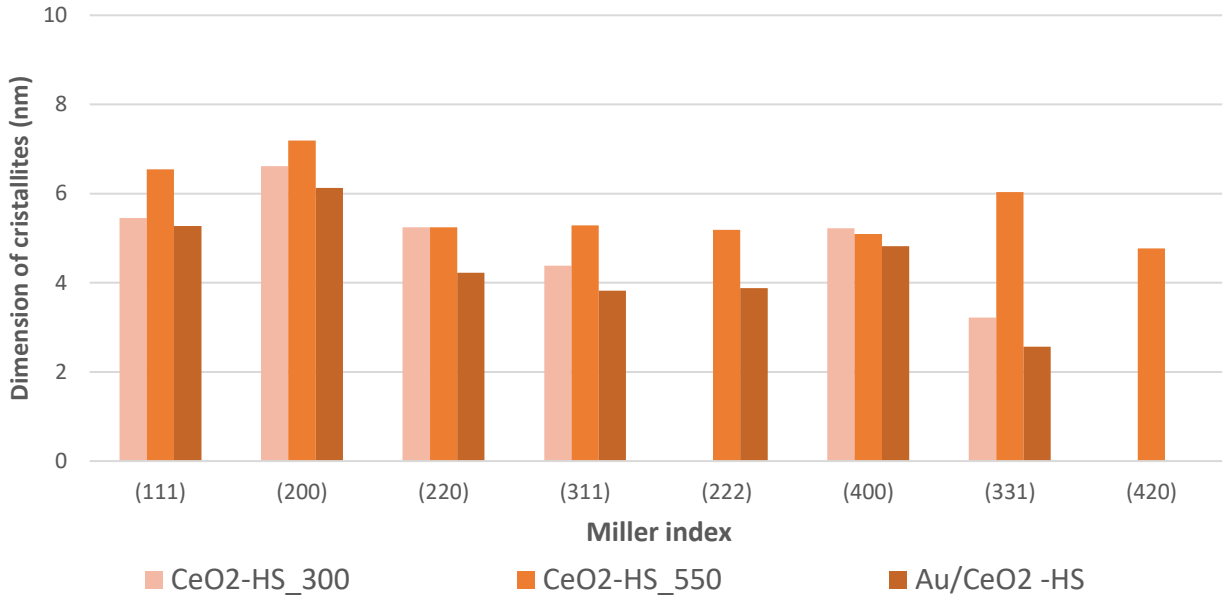

Figure 50: Dimensions of crystallites for CeO_2-HS samples

No relevant differences have been detected between the recorded and tabulated relative intensities in the XRD spectra (reference code: 00-043-1002, comparisons in Figure 51).

All the peaks show slightly higher relative intensities than the tabulated one, is then possible to assume that the reference peak (111) could be slightly less exposed. The main difference can be noted between samples CeO_2_300 and Au/CeO_2_300, where the peaks (220) and (311) show a reduction of 7% and 3% respectively after the DP process. No preferential increases in the crystalline planes exposures have been noticed. The lack of the signal at 79.2 *2θ* for the samples CeO_2-HS_300 and Au/CeO_2-HS are only artefacts due to the peak overlapping.

Figure 51: Differences between intensities tabulated and measured for samples CeO2-HS (tabulated intensities reference code: 00-043-1002)

The XRD analysis carried out on the catalyst sample Au/CeO_2-HS between 36 and 41 is shown in Figure 52. It is not possible to distinguish the peak of gold around 38 2θ[13], the peak might not be visible if the gold nanoparticles are well distributed and smaller than 5nm[17].

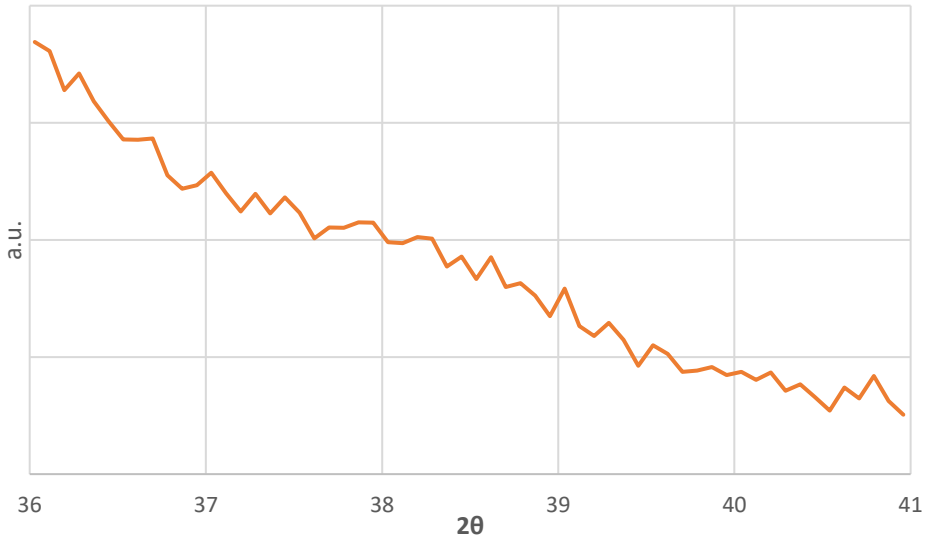

Figure 52: XRD analysis between 36 and 41 2θ of sample Au/ CeO_2-HS

3.2.2 *Raman analysis of CeO_2-HS samples*

The spectra of high-surface samples clearly show the characteristic peaks of ceria (Figure 53), this is due to the high surface area of the samples that allows the exposure of more defects and more bonds for the Raman analysis.[24] The surface area of about 140-160 m^2/g was confirmed in the previous paragraphs by the BET analysis, and it is higher than the surface area of the CeO_2-C samples, which did not show clearly at Raman the 2TA and the D-band peaks at around 250 and 600cm^{-1} respectively (chapter 3.1.2) .

Peaks due to impurities have been recorded at 825 and 1040 cm^{-1}. The peak at 825 disappeared after washing the sample with pure water, so it is probably due only to traces of soluble species, as chlorides, left on the samples. The peak at 1040 cm^{-1} is caused to traces of carbonates chemisorbed onto the ceria surface.[14,25,26]

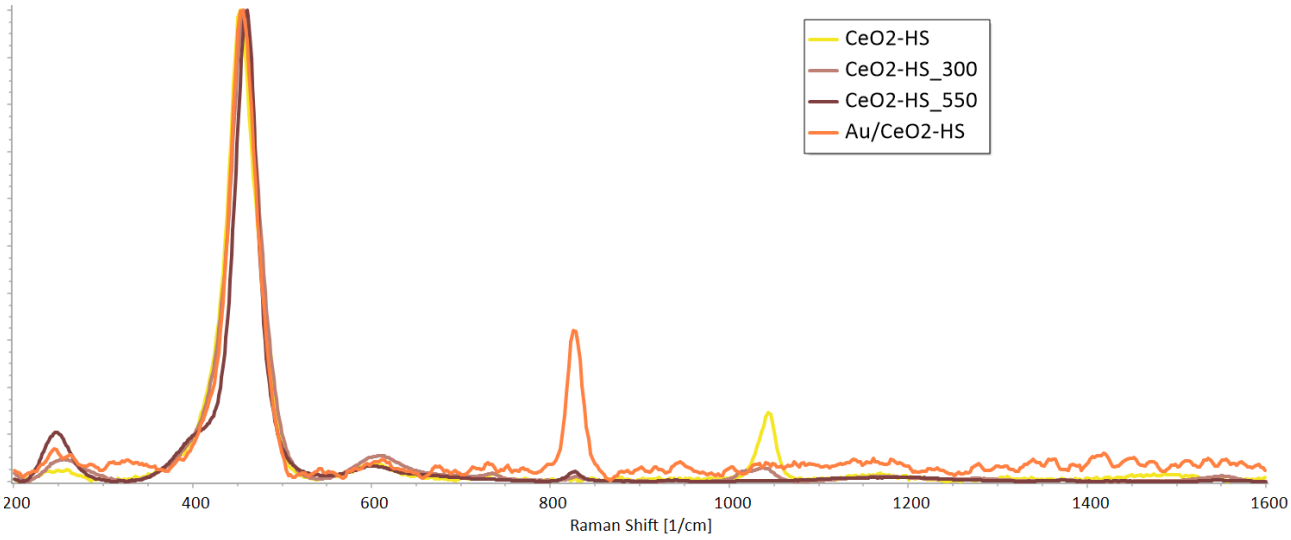

Figure 53: Raman spectra of CeO2-HS samples from 200 to 1600 cm^{-1}

Comparing the spectra of the CeO_2-HS samples with the spectrum of the sample CeO_2-C (Figure 54), the untouched low-surface commercial ceria, used as reference is possible to notice a marked peak broadening of the main peaks in the CeO_2-HS samples. This phenomenon is due to the smaller dimension of the crystallites in the CeO_2-HS samples, and it is in accordance with the dimensions reported in chapters 3.1.1 and 3.2.1.

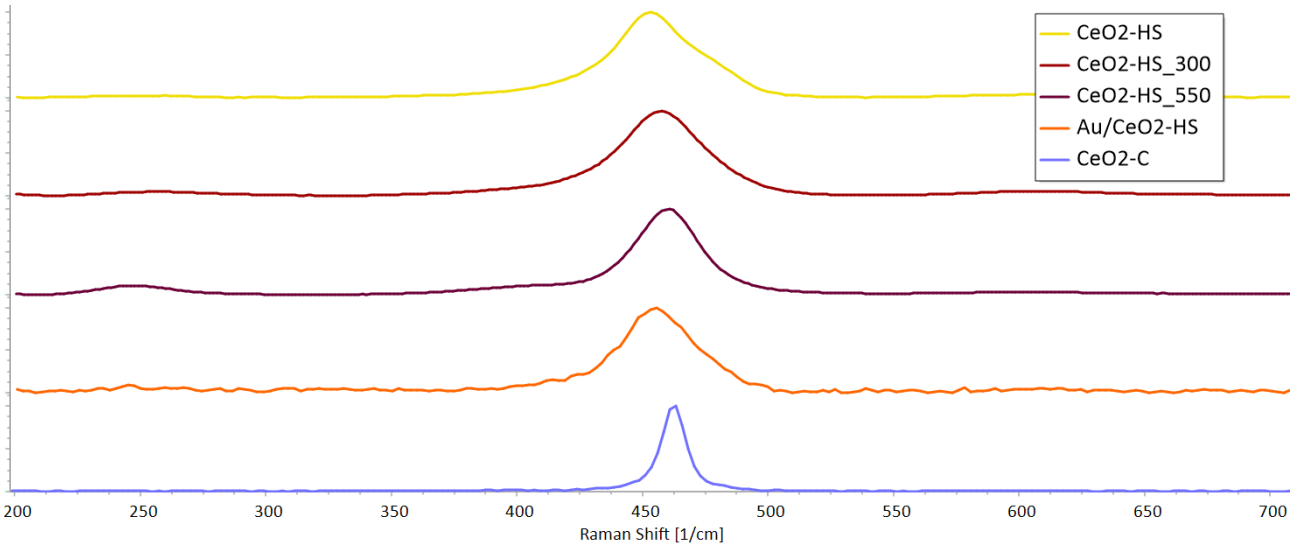

Figure 54: Raman spectra of Ceo2-HS samples compared with the sample CeO_2-C

The D-band shows an increase from the sample of untouched support (CeO_2-HS) to the sample calcined at 300°C (CeO_2-HS_300) and a decreasing in the sample calcined at 550°C (CeO_2-HS_550), (Figure 55), this trend is in line with the trend of the defectivity and surface area caused by the calcination temperature recorded in litterature[6]. The sample Au/CeO_2-HS that is calcined at 300°C shows a lower D-band than the support calcined without gold nanoparticles at the same temperature (CeO_2-HS_300), this effect is caused by the gold nanoparticles deposited on the ceria which cover its defectiveness.[15,27,28]

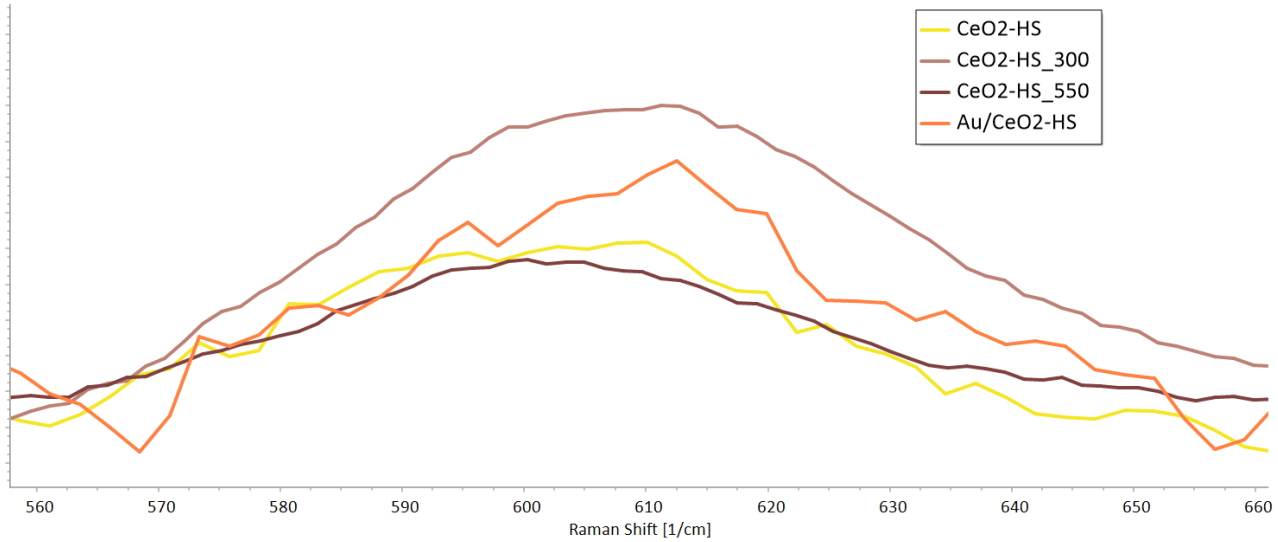

Figure 55: D-band patterns in high surface samples

3.2.3 *DRUV-Vis analysis of CeO_2-HS samples*

The DRUV-Vis spectra of the samples CeO_2-HS have been reported in Figure 56, in the Au/CeO_2-HS sample is visible the surface plasmonic resonance band with is maximum at 575nm, the presence of this bands confirms the hypothesis that gold nanoparticles were correctly deposited on the support but were too small to be detected via XRD in the Au region (chapter 3.2).[17] Usually, smaller nanoparticles lead to a blue shift of the peak, and therefore a shift to smaller wavelengths, but, comparing the plasmonic resonance bands of the samples Au/CeO_2-HS and Au/CeO_2-C (blue line), one can observe the opposite trend. The cause probably lies in the different metal-support interaction due to the different morphologies and dimensions of the two supports. [20]

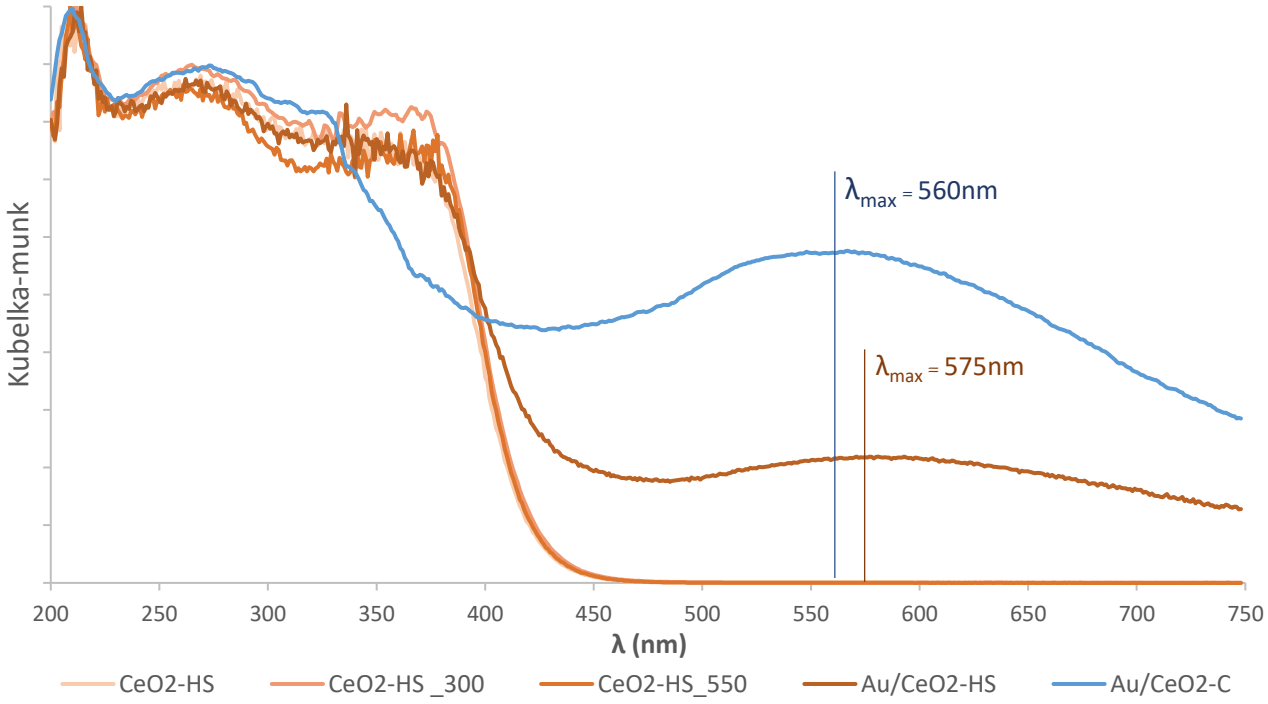

Figure 56: DRUV-Vis on CeO_2-HS samples

From the DRUV-vis analysis on commercial samples with high surface area (Figure 57) and as explained in chapter 3.1.4, is not possible to notice the different amount in the content of Ce^{3+} and Ce^{4+} in the region 200-300nm in the different samples.

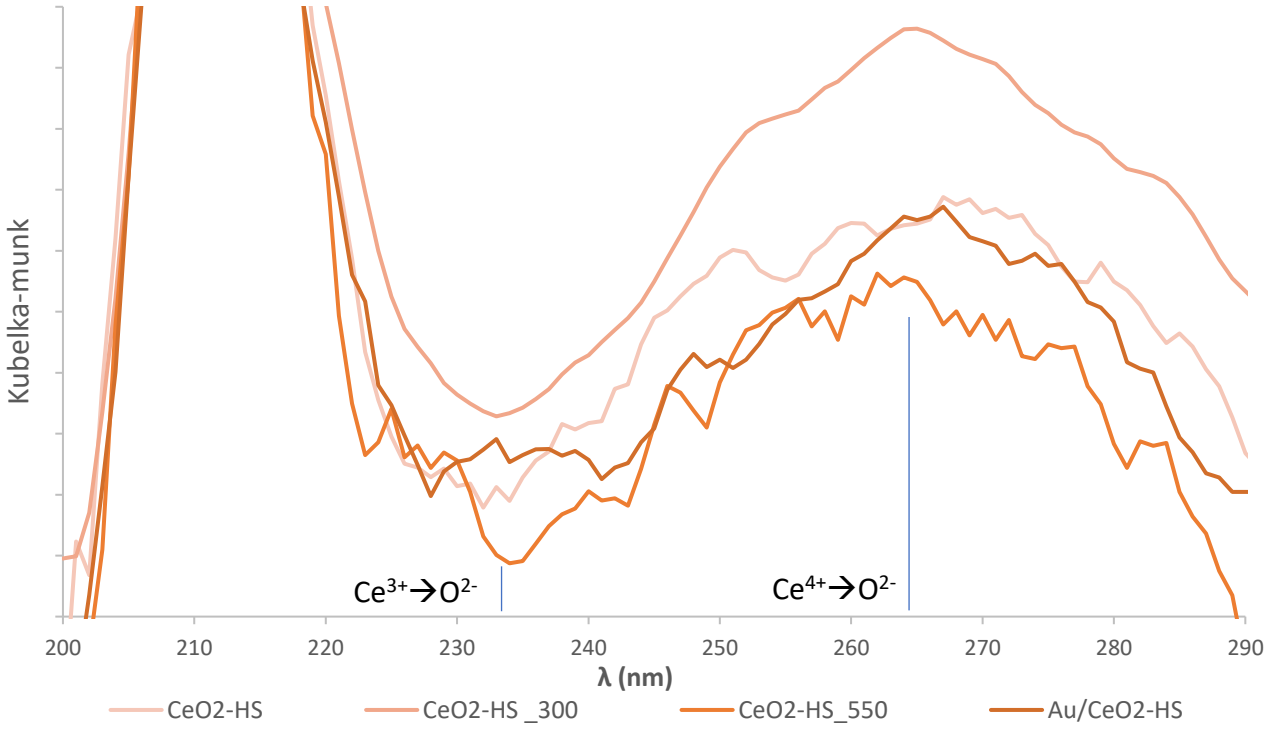

Figure 57: DRUV-Vis on CeO2-HS samples, between 200 and 390nm

3.2.4 *Catalytic tests on CeO_2-HS samples*

The results for the catalytic test for the catalyst supported on commercial ceria with high surface samples are reported over time at different temperature in the following Table 7, 8, and Figure 58, and compared to the reaction blanks in the same conditions.

The presence of the catalyst leads to complete conversion of HMF, as for the catalyst supported on the cerium oxide with low area (chapter 3.1.4) but the reaction seems to proceed less rapidly over HMF, leading to lower yield in FFCA and FDCA. The catalyst seems to be less selective than commercial sample with low surface area, leading to higher carbon losses over time.

The catalyst's performance for the same reaction performed at 80°C (8) resemble the same pattern recorded at 70°C, but higher yield and better selectivity after 4 hours of reaction. Considering that high carbon losses have been visually detected by observing the colour of the post-reaction mixture (as explained in chapter 2.2.13) after 1 and 2 hours of reaction time at 80°C, the injection in the HPLC column has not been executed.

time (h)	X HMF (%)	Y HMFCA (%)	Y FFCA (%)	Y FDCA (%)	Carbon Loss (%)	Note:
4	94	28	6	4	57	Blank reaction, in absence of any support or catalyst
4	94	24	2	2	65	Blank reaction, in presence of CeO_2-HS calcined at 300°C (CeO_2-HS_300)
1	100	79	8	5	8	
2	100	75	6	13	6	
4	100	64	2	16	18	

Table 7: Catalytic test results over time of the Au/CeO_2-HS catalyst, conditions: HMF: NaOH 1:4, 70 °C

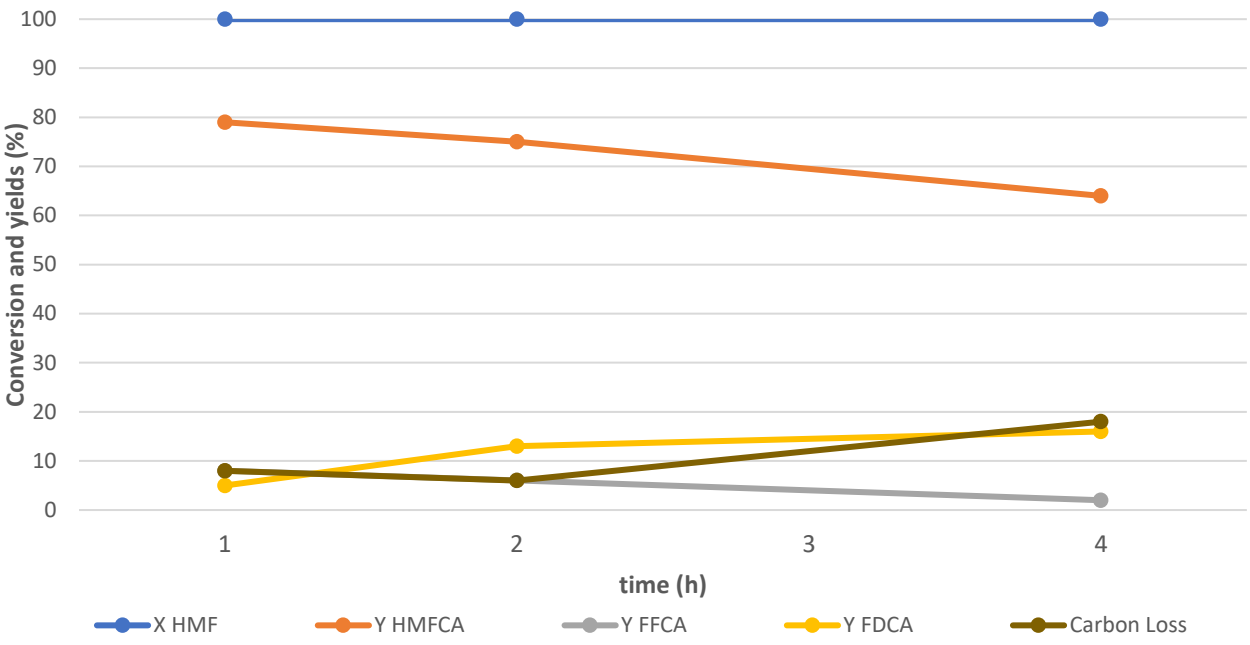

Figure 58: Conversion and products yields over time for the Au/CeO_2-HS catalyst, T= 70 °C

time (h)	X HMF (%)	Y HMFCA (%)	Y FFCA (%)	Y FDCA (%)	Carbon Loss (%)
1	Not injectable due to heavy products				
2	Not injectable due to heavy products				
4	100	55	3	33	9

Table 8: Catalytic test results over time of the Au/ CeO_2-HS catalyst, T= 80 °C

3.3 Catalysts prepared by electrospinning

The synthesis of CeO_2 nanofibers have been performed by electrospinning and subsequent heat treatments. PVP was used as a guiding polymer and viscosity controller for the formation of a uniform fibrous structure because it has remarkable characteristics such as high molecular weight and high solubility in polar solvents.

First of all, a study has been performed to optimise the spinning conditions in our spinning setup.

There are plenty of different spinning conditions and composition of spinning solutions tested in literature[1,4,17,29], depending on the different setup available and final structure desired (nanotubes, nanobelts nanofibers, etc.). The initial spinning condition and the solution composition used for our study has been chosen from a paper by Gibbons et al.[1] in order to produce regular ceria nanofibers.

The composition of the spinning solution used is: 6.0g H_2O, 6.6g ethanol, 2.2g $Ce(NO_3)\cdot 6H_2O$ and 1,4g PVP the correct amount of chloroauric acid was added if needed in order to obtain a metal/support ratio of 1.5%wt. Some tests have been performed to carry out correctly electrospinning and to maximise the productivity of the process. The tests involved changes in the composition of the solution and the electrospinning parameters (voltage, flow, distance tip-collector). Chosen electrospinning conditions are reported in Table 9.

	In literature[1]	**Selected conditions**
Voltage (kV)	22	11-13
Distance (cm)	22	15
Flow (mL/h)	1.0	1.1-2.2

Table 9: List of spinning conditions found in literature and the ones used

The difference between the optimal conditions in the literature and those selected by us is probably due to the different instrumentation we are equipped with Figure 59), as we have neither a rotary drum nor a second generator available to apply an opposite potential to the collector surface.

Figure 59: The set up for electrospinning used, from left to right: generator, pump with the syringe and the collector (not covered by a sheet to collect the nanofibers)

The voltage and the flow used varies slightly according to the environmental conditions of the day, in particular: temperature and relative humidity, to try to maximise the productivity while keeping the flow stable, avoiding drops "thrown" in the direction of the collector surface that could compromise the deposited material. The environmental parameters are not controllable in this type of set up, and they could be decisive for a correct spinning, e.g., at a temperature lower than 17°C let the solution too viscous to be spun and, a temperature lower than 20°C let the maximum exploiting flow of 1.4 mL/h only.

The optimised conditions have been tested for 30 minutes each when the spinning was considered stable, then, the products have been analysed by SEM microscopy to evaluate if they were producing nanofibers and or undesired products such as: beads, irregular nanofibers or film. High values of flow or voltage led to film (Figure 60-A) or irregular nanofibers (Figure 60-B).

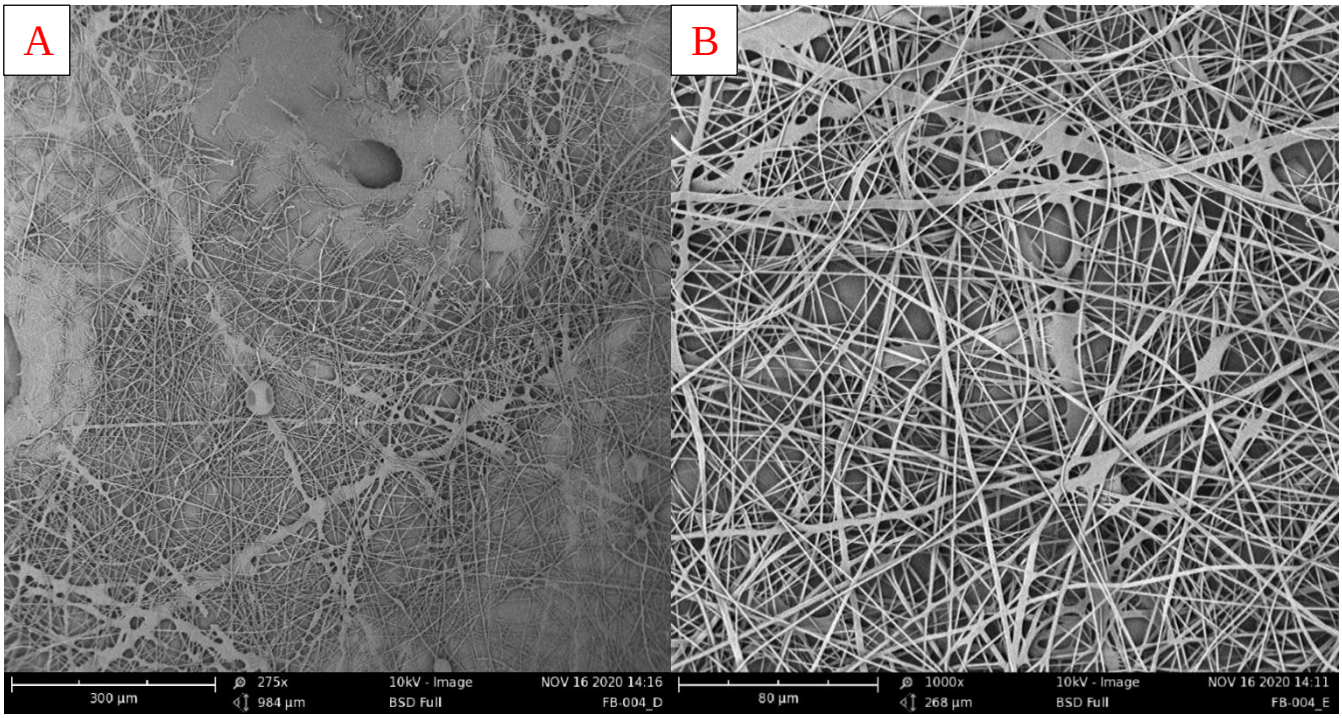

Figure 60: deposit of film and broken nanofibers due to a flow higher than 2,2ml/h (A) and irregular nanofibers due to a voltage higher than 15kV (B) on our set up

3.3.1 *Synthesis and characterization of CeO_2 nanofibers via electrospinning*

In this part of the study, we prepared CeO_2 nanofibrous mats with a uniform three-dimensional structure via the optimized electrospinning technique. The collected nanofibers were then calcined at different temperatures in air atmosphere to eliminate the polymer substance (PVP) and obtain pure CeO_2 nanofibers. Then, gold nanoparticles were loaded by deposition precipitation on the surface of the prepared cerium oxide (Figure 61).

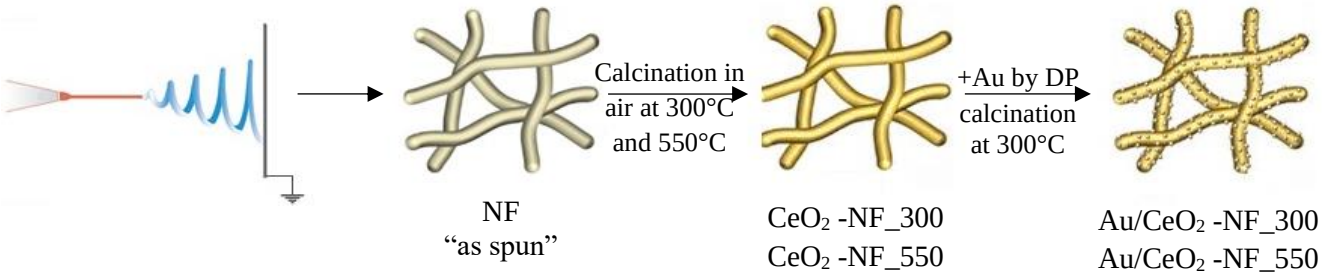

Figure 61: Scheme of the synthesis of the ceria nanofibers via DP

The prepared samples are summarized in Table 10.

Sample	Surface Area (m^2/g)	Description
NF "as-spun"	-	Nanofiber of PVP and cerium nitrate as-electrospun
CeO_2 -NF_300	83	Ceria nanofiber calcined at 300°C
CeO_2 -NF_550	21	Ceria nanofiber calcined at 550°C
Au/CeO_2-NF _300	77	Au supported on CeO2 nanofiber calcined at 300°C
Au/CeO_2-NF_550	29	Au supported on CeO2 nanofiber calcined at 550°C

Table 10: samples of ceria nanofibers produced and surface area values calculated using the BET method

The morphology and microstructure of the as-electrospun CeO_2 fibres before calcining is shown in Figure 62.

The produced nanofibers electrospun in the optimised conditions have a diameter of 435 ± 90 nm, the samples as at naked eye the appearance of a thin white film. Using a pair of clean

scissors, the samples have been cut into squares of few centimetres and inserted in a small crucible to be calcined.

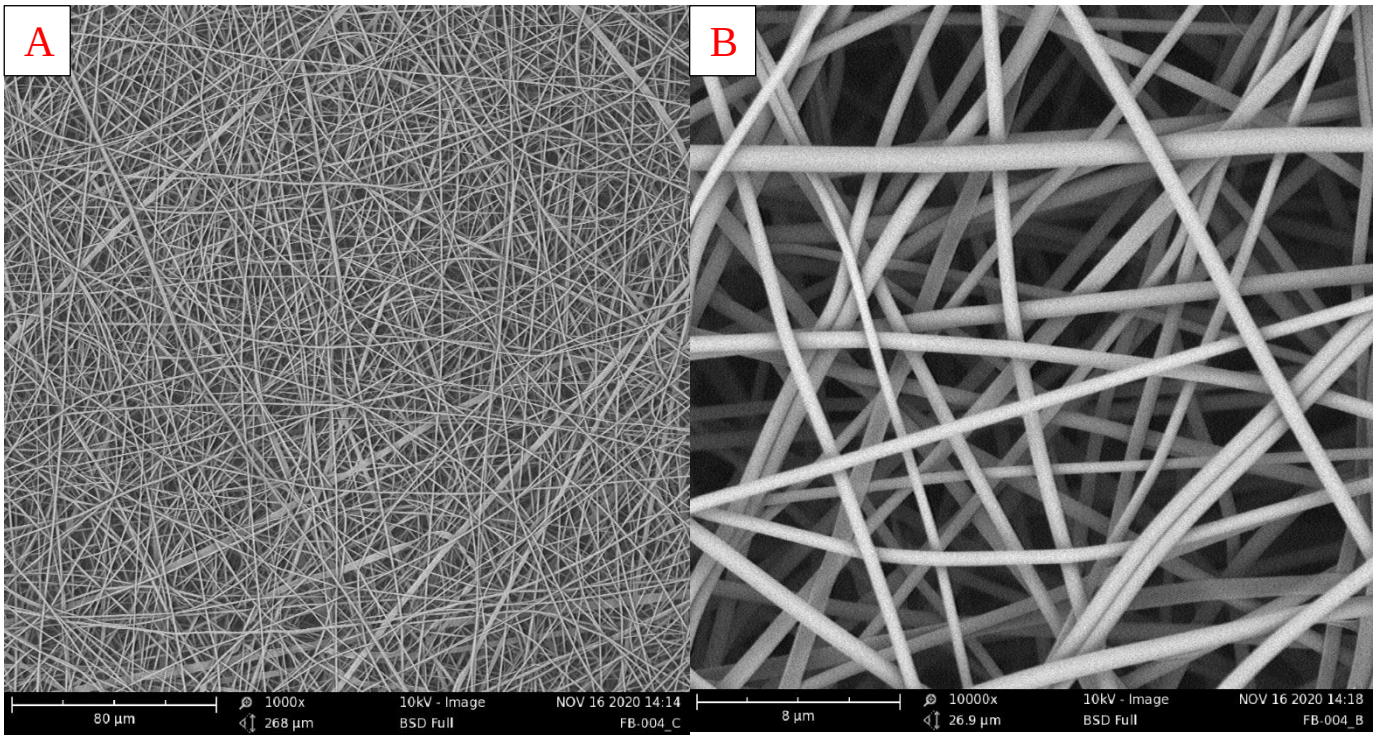

Figure 62: CeO_2 nanofibers as electrospun obtained using the optimised condition on our set-up (A), higher magnification (B)

To optimize the PVP elimination, a TGA-DTG analysis has been performed on the spun fibres to evaluate the behaviour of the sample during the heating and to evaluate the correct heat treatment to not damage the samples[1].

The temperature ramp used in the TGA was: 2°C/min from room temperature to 200°C, 0.2°C/min until 600°C, 2°C/min to 800°C and 1 hour of isotherm maintenance; this ramp was meant to evaluate the calcination ramp used for the nanofibers and to better understand their behaviour during the process.

In the TGA analysis is easily recognizable the exothermic combustion of the PVP contained in the fibres at about 245°C (reported in Figure 63 and the respective DTG in Figure 64) the associated weight loss of the sample is from 90% to 30% of the original weight.

The first weight loss recorded in the sample is due to desorption of water, it is around 10% of the weight of the sample and the wright change ends at 100°C.

The other three “steps” visible on the DTA curve (Brown line, Figure 63) at 220, 320, and 700°C are only artefacts caused by the thermal inertia of the instrument.

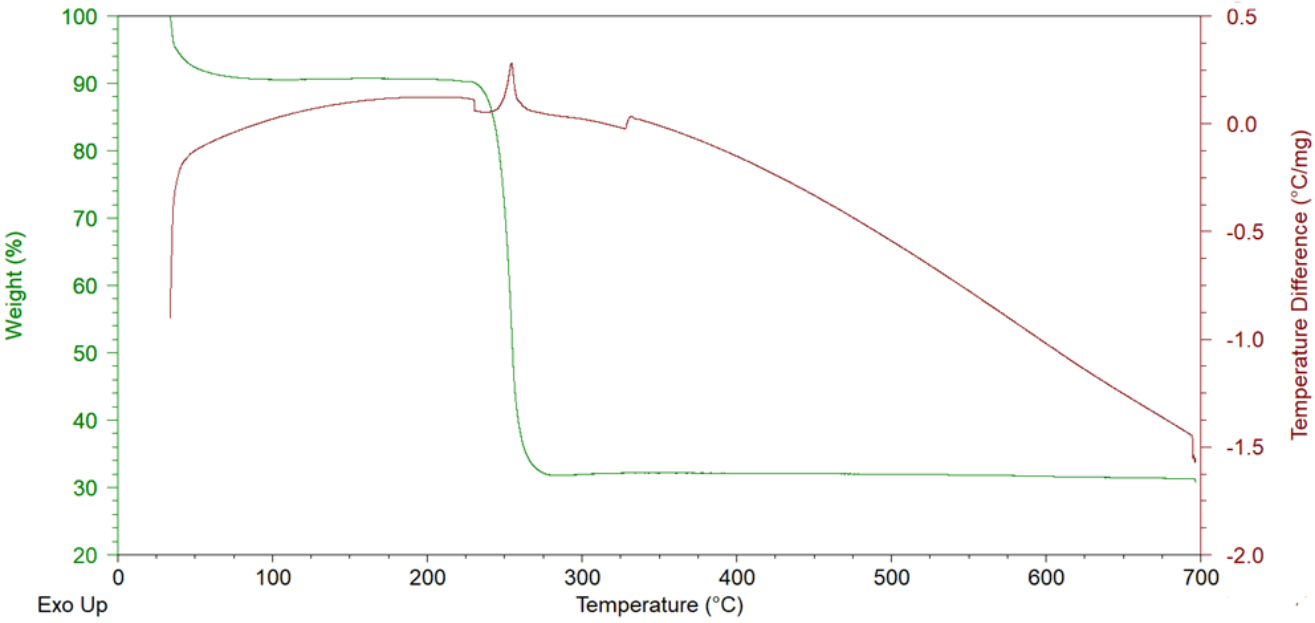

Figure 63: Thermogram of the TGA analysis of the sample CeO_2-NF as spun

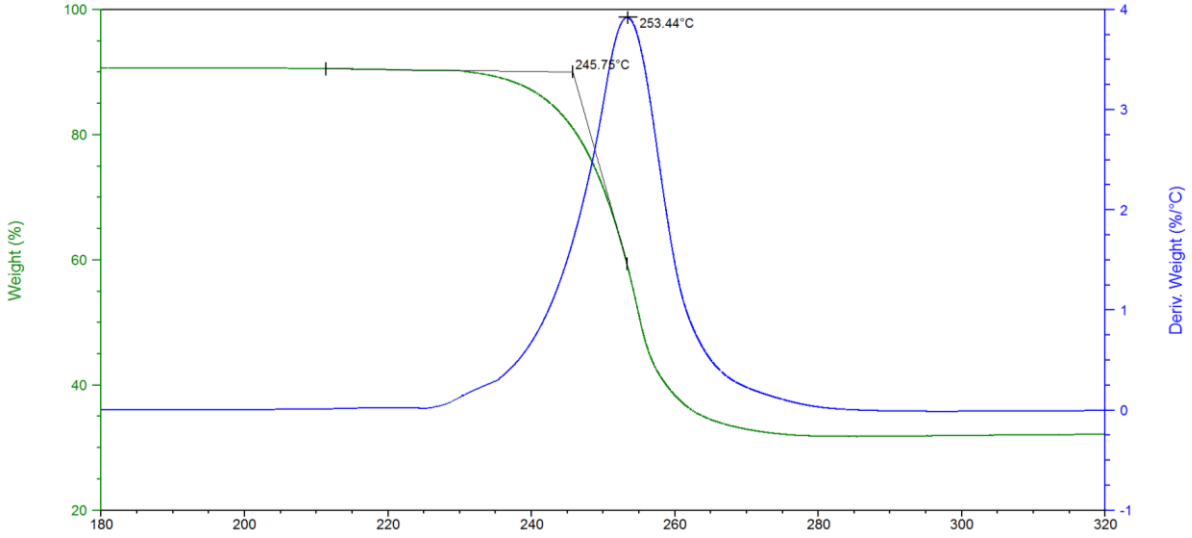

Figure 64: TGA-DTG analysis of as-spun nanofibers detail on the peak of PVP combustion. On Y axis: in green the weight loss percentage, in blue the derivative of the weight loss, temperature on X axis

Considering that the heat developed during the TGA because the PVP combustion was not too high to damage the sample, the calcination was then carried out using a ramp of 0.2°C/min up to the desired temperature (300°C or 550°C), the temperature was then maintained for 3 hours.[1] After calcination, the diameter of the fibres is equal to 400 ±100 nm and the surface area of the samples is 83m^2/g for the sample calcined at 300°C and 21m^2/g for the one calcined at 550°C (Figure 65 and Figure 66).

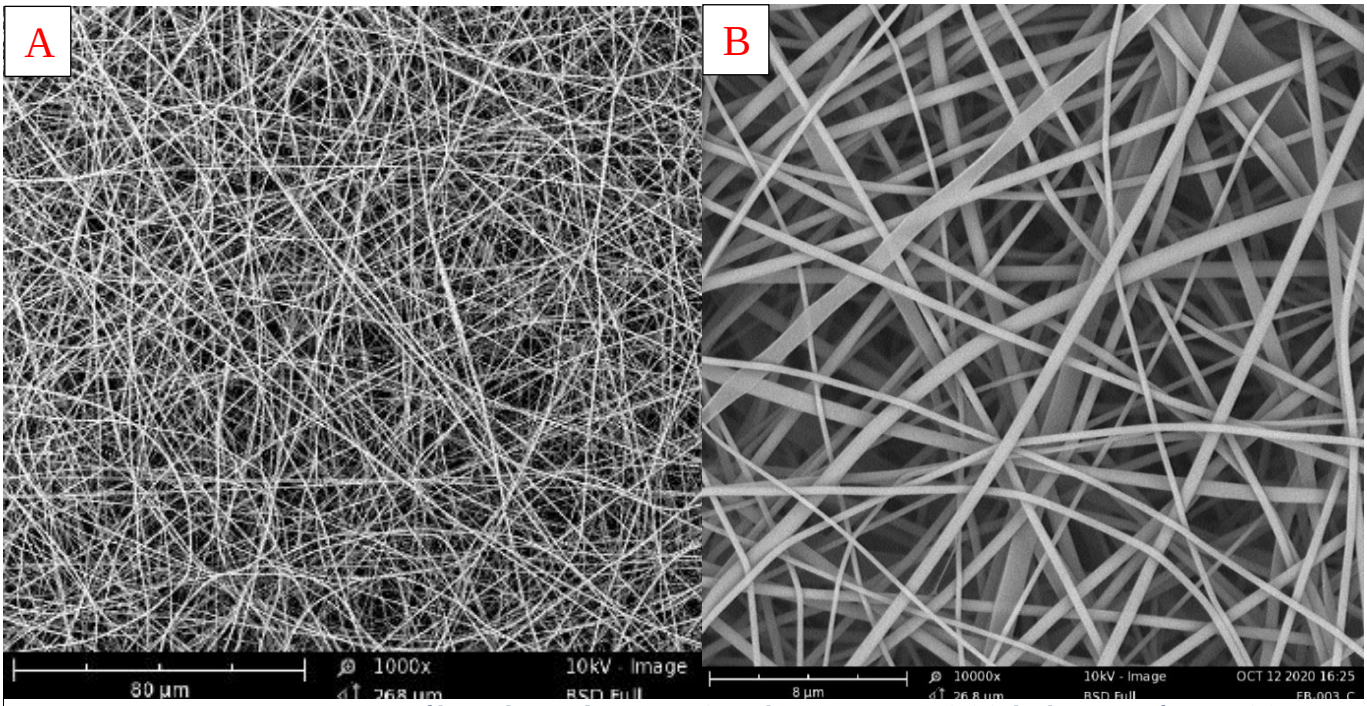

Figure 65: SEM images on CeO2 nanofibre calcinated at 300°C (sample CeO2-NF_300) (A), higher magnification (B)

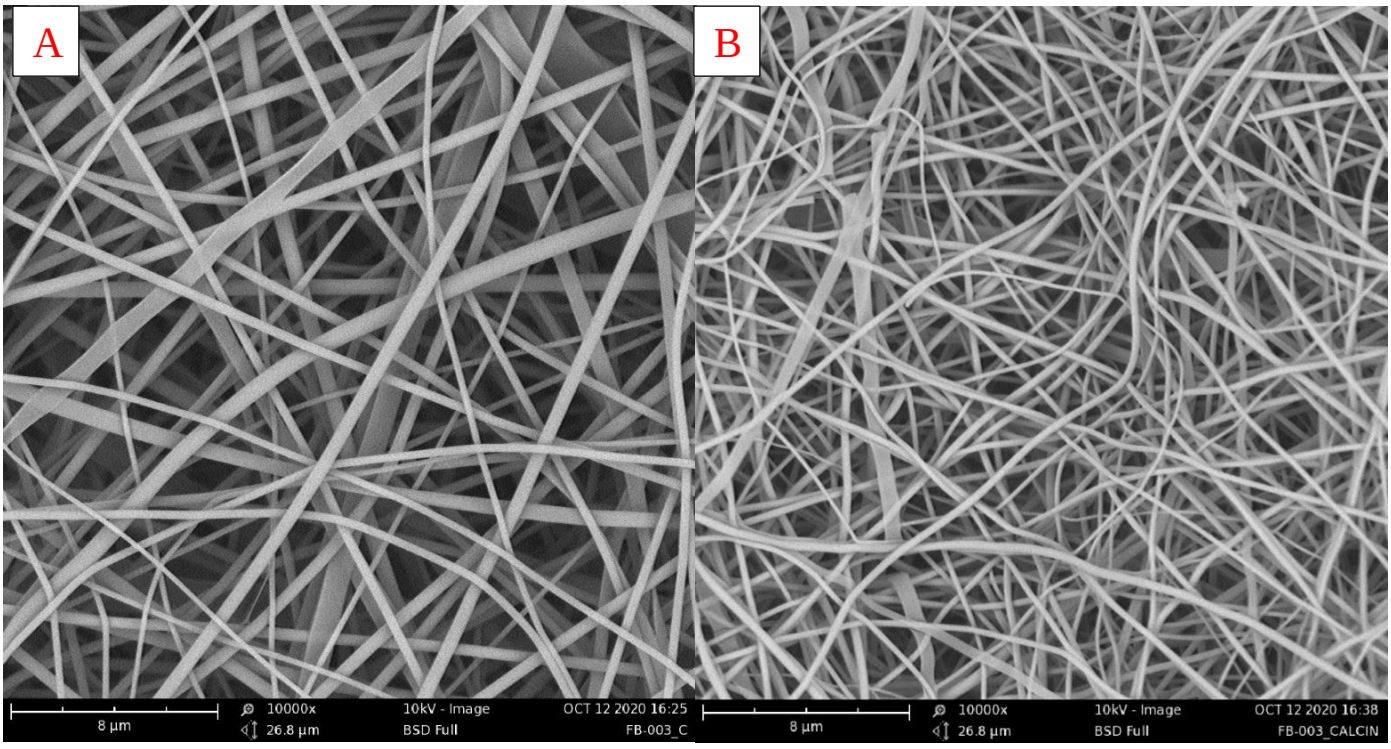

Figure 66: Comparison of SEM images for samples calcined at 300°C (CeO2-NF_300) (A) and 550°C (CeO2-NF_550) (B).

To verify if the thermal treatment at 300°C was sufficient to eliminate completely the PVP from fibre, a TGA analysis has been performed on the samples CeO_2-NF_300 (nanofibers calcined at 300°C) in order to evaluate possible leftovers of PVP on the fibres after calcination (Figure 67). In this case, the temperature ramp used was from room temperature to 700°C with a 10°C/min heating ramp and followed by 10 minutes of isotherm.

The analysis of the CeO_2-NF_300 sample (Figure 67) shows a continuous loss of weight during the process and is particularly intense in the first part. The curve of the temperature difference shows first an exothermic process followed by an endothermic one. Looking at the results, the total loss on the sample of 4% of the original weight is probably due to combustion processes of lighter PVP leftovers at lower temperatures, and to desorption of product at higher temperature.

This second weight loss is continuous too, and it is less marked than the one reported previously, probably because of the presence of different lighter oxidation product on the sample due to the previous calcination treatment at 300°C. The mass lost during the analysis is 4% of the initial mass of the sample, 2% is lost before 100°C and the remaining 2% after 100°C. These data seem to indicate the elimination of almost all the PVP after calcination in air at 300°C, with only traces of organic left.

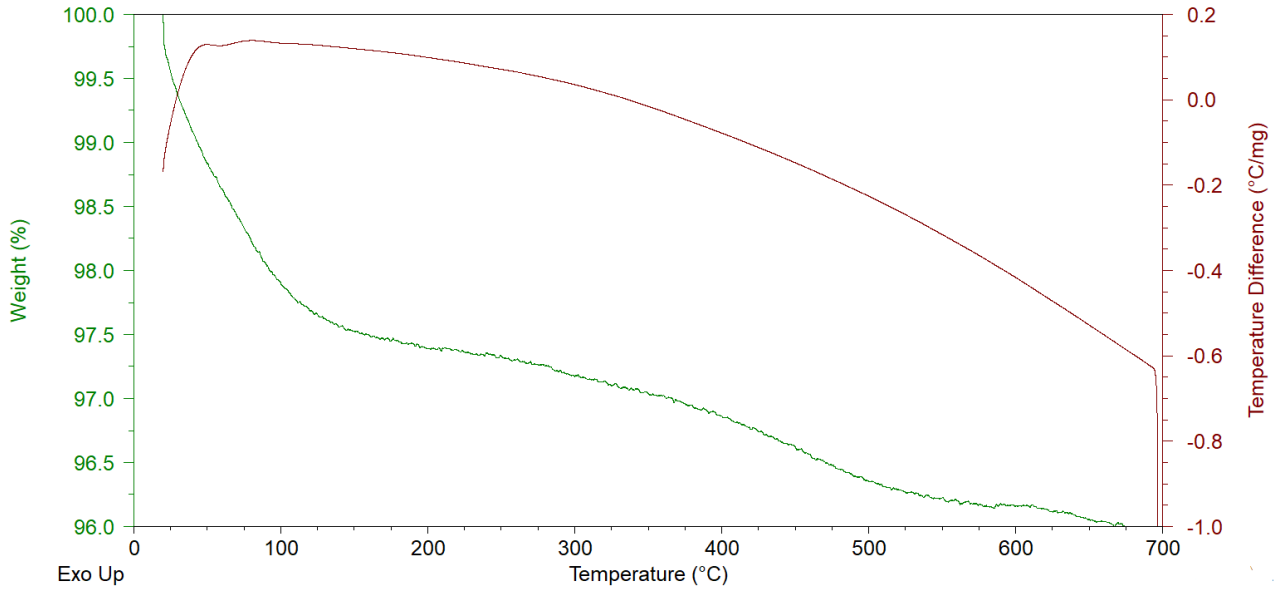

Figure 67: TGA analysis on sample CeO_2-NF_300 (ceria nanofibers after calcination at 300°C)

3.3.1.1 ATR analysis of CeO_2-NF samples

Nanofibers were analysed via ATR before and after calcination (Figure 68 and Figure 69), to facilitate the comparison between the various heat treatments, the ATR spectrum of PVP and cerium nitrates used during spinning have been reported too. The PVP has characteristic peaks at 2930, 1670, 1420, 1280 cm^{-1} (yellow spectrum and yellow lines), such peaks are attributed to the vibrational stretching of the bonds C-H, C=O, $-CH_2$ and C-N. The peaks of the fingerprint region of the PVP are located between 1280 cm^{-1} and 600 cm^{-1}. The peak at 3450 cm^{-1} is due to surface hydroxyl groups, this peak is still recognizable shifted at 3300 cm^{-1} after the calcination process, because of the hydroxyl groups present on the ceria surface.[25,29,30]

On the nanofibers as electrospun ("NF as spun", blue curve) it is still possible to observe the peaks of PVP, among the three main peaks of the cerium nitrate, between 1200 and 1700 cm^{-1}, the first two have a slight red shift, while the third a blue shift, there are also the peaks of cerium nitrate located between 740, 810 and 1040cm^{-1} (shaded blue lines, Figure 69).

The characteristic peaks of the PVP in the calcined samples (the two grey tracks) are hardly visible in nanofibers calcined at 300°C (highlighted with a triangle in the following figures), and not present in the one calcined at 550°C, while the absorptions of the cerium oxide are visible at 3300 cm^{-1} due to HO groups on its surface, and below 600 cm^{-1}, as strong absorption caused by Ce-O stretching (grey lines, Figure 70). The peaks attributed to C=O, at 760 and 1340 cm^{-1}, are still slightly visible in the calcined sample, but it is only due to carbon dioxide from air[26,29,31]. The peaks at 760 and 1510 cm^{-1} are due to carbonates chemisorbed on ceria surface[26,31].

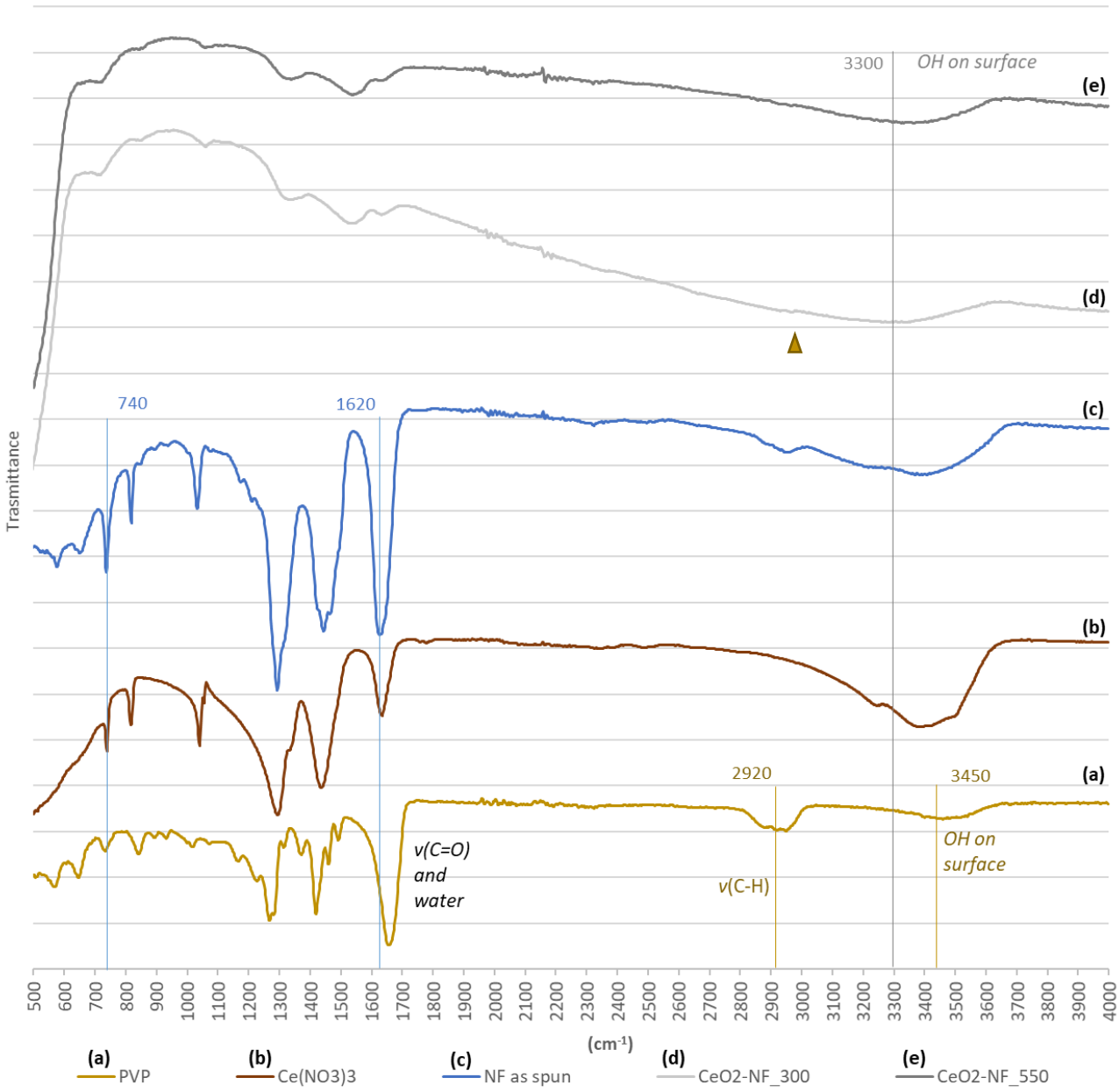

Figure 68: ATR spectra between 500 and 4000cm-1 of nanofibers samples and precursors used

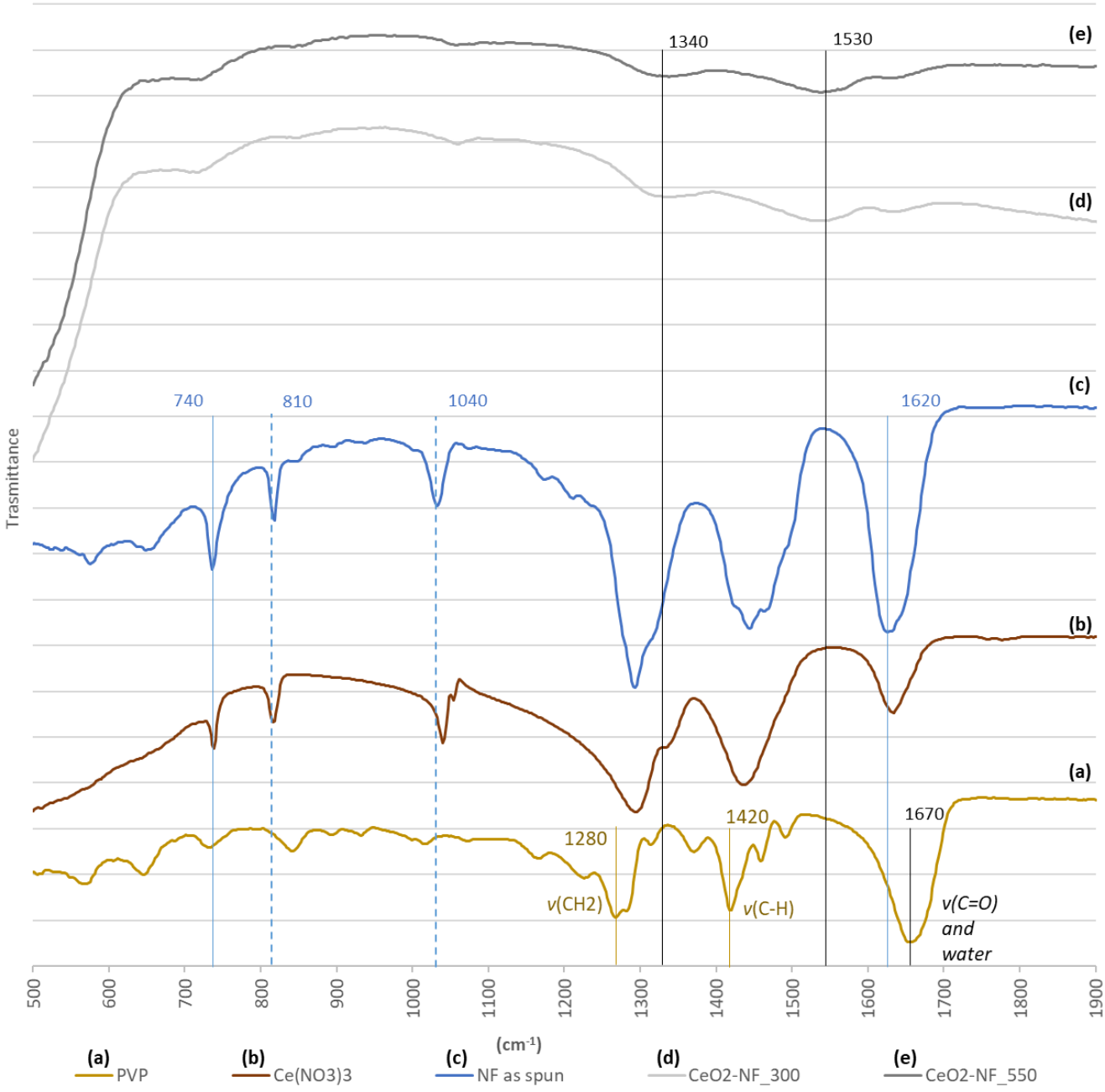

Figure 69: ATR spectra of nanofibers samples and precursors used, magnification between 500 and 1900cm^{-1}

The ATR spectra of the supports in nanofibers calcined at different temperature and of the different catalyst have been reported in Figure 70, once again a small amount of PVP leftovers have been barely detected at 2930cm^{-1} (yellow triangle) the catalyst samples calcined at 300°C: Au/CeO_2-NF_300.

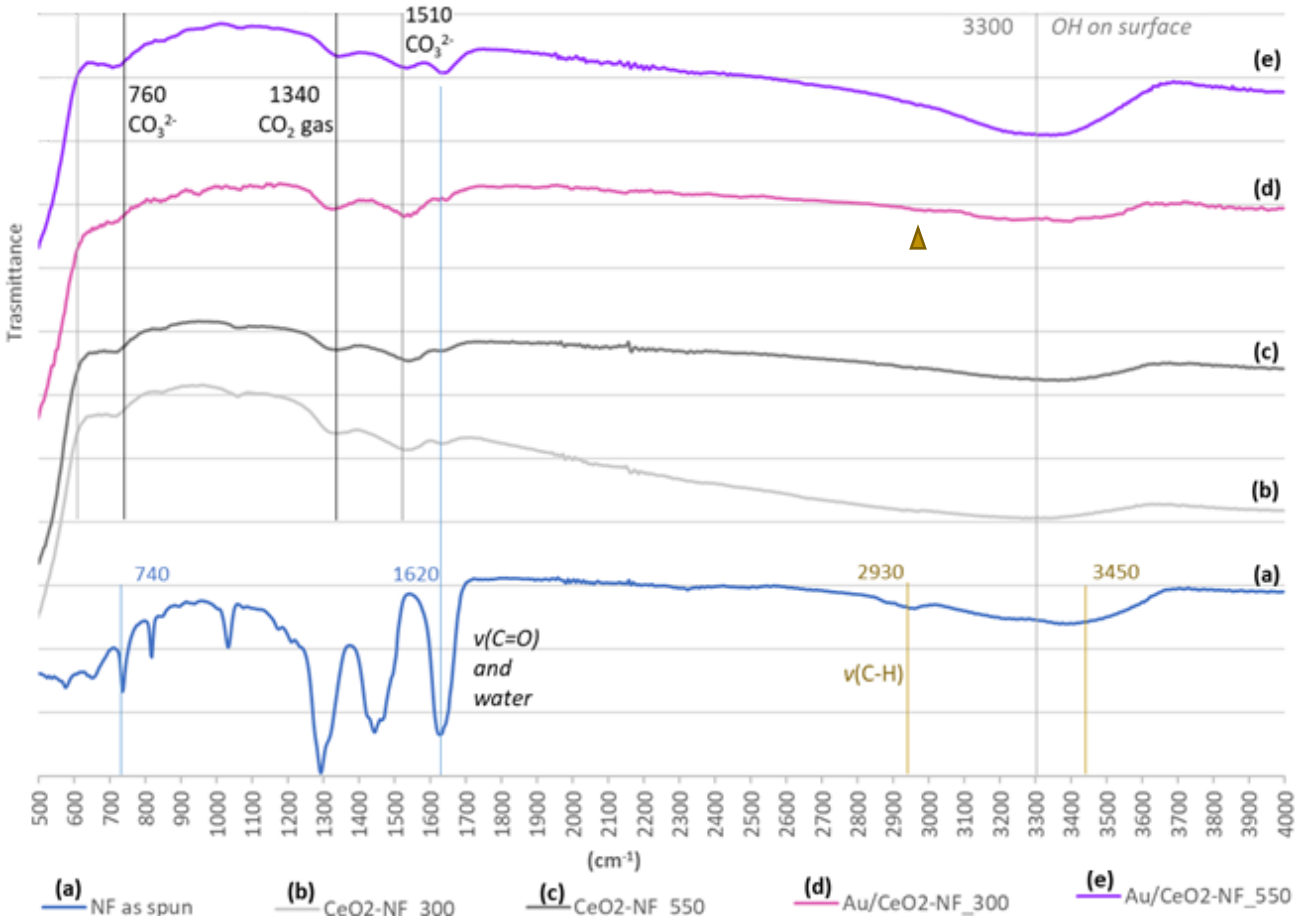

Figure 70: ATR spectra between 500 and 4000cm-1 of catalyst in nanofibers

3.3.1.2 TEM of ceria nanofibers

TEM analysis on Ceria Nanofibers after calcination at different temperature are reported in Figure 72 and Figure 74. The analysis confirms the formation of nanofibers with a length from one to tens of microns, and a diameter from 100 to 500 nm (Figure 71), as reported previously by SEM analysis too. The nanofibers show a better crystalline structure with the increase of calcination temperature (Figure 72). The HRTEM images (Figure 71– D) revealed fibers made of nanocrystals which dimensions range from 5 to 10 nm after calcination at 300°C, or from 5 to 20nm after calcination at 550°C. This fact is in accordance with the dimensions calculated using the Scherrer equation from the XRD analysis.

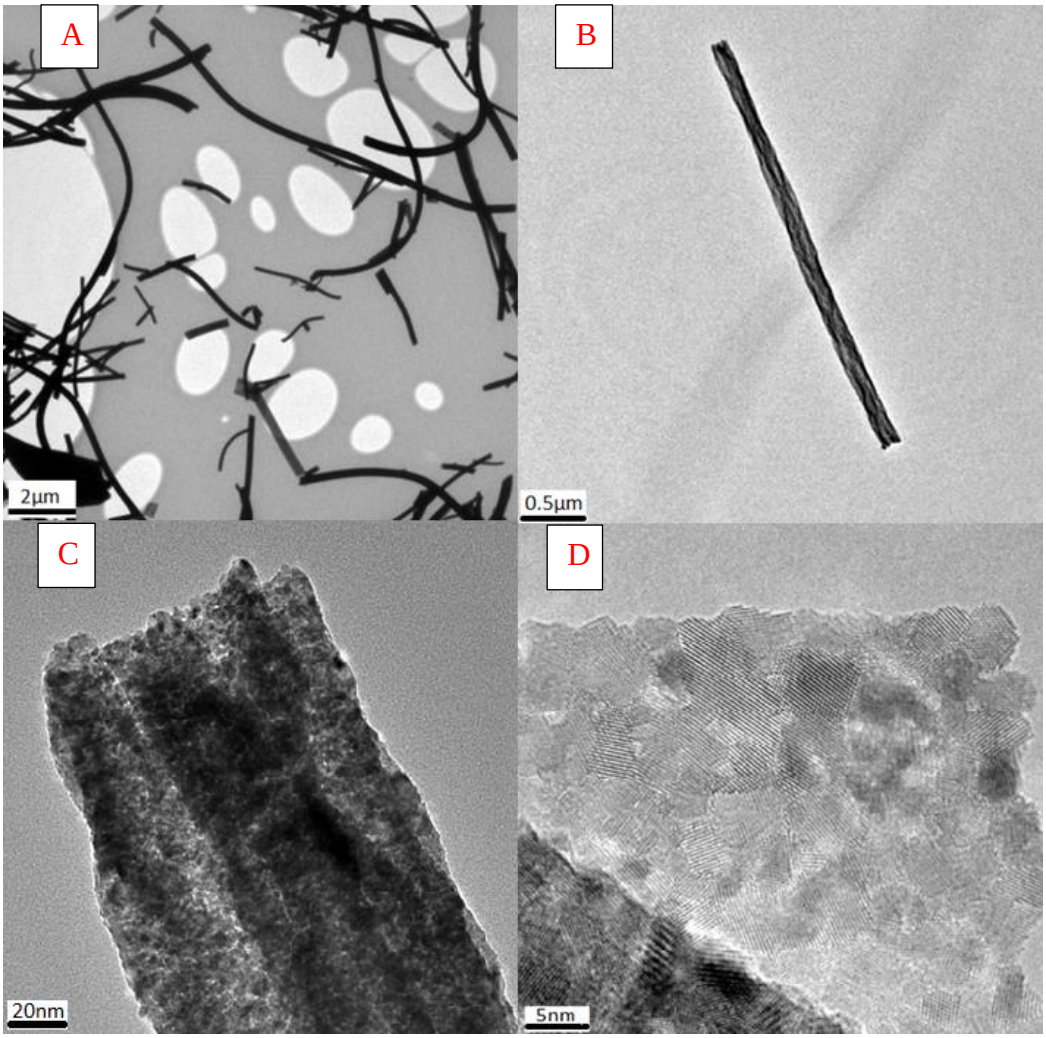

Figure 71: TEM images of CeO_2 nanofiber calcined at 300°C, higher magnification from A to D

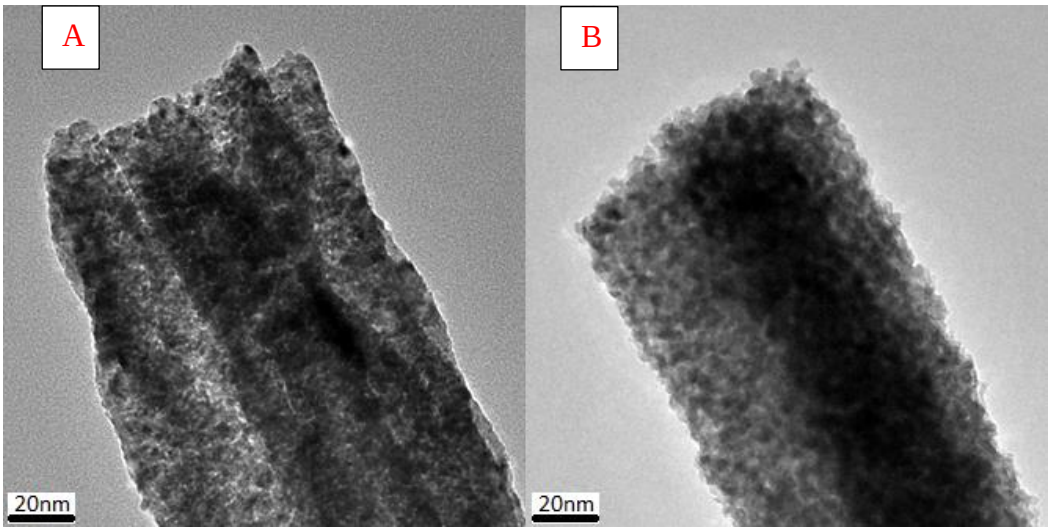

Figure 72: Comparison between TEM images of CeO_2 nanofibers calcined at 300°C (A) and at 550°C (B)

The rings of the SAED pattern (Figure 73) sampled on the crystals can be index as cerianite, this confirms that the fibers are made of CeO_2 nanocrystals.

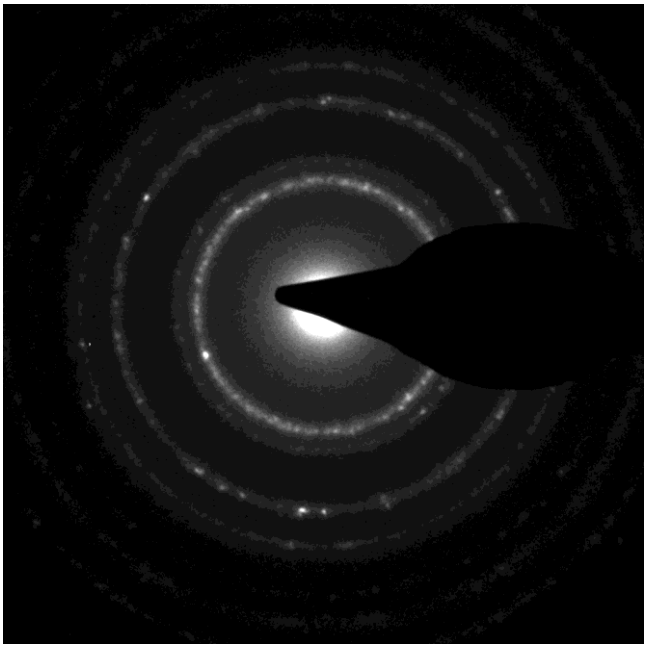

Figure 73: SAED pattern of calcined nanofiber sample

No significant changes in the length or the diameter of nanofibers have been reported by TEM observation before and after the DP process of Au nanoparticles (Figure 74). The dimensions of Au nanoparticles range from 5 to 20 nm, the gold nanoparticles have been observed in annular dark-field imaging (HAADF, Figure 74 A) however, locating the smallest nanoparticle

was not an easy task. The HAADF technique allows to produce contrast in the image in function of the atomic number squarer, but cerium and gold are not that dissimilar to be easy recognized when they are in little particles. As a result of this, most of the smallest Au nanoparticles were mistaken by small ceria crystallites protruding from the main fibre. To not overestimate the Au-NP size distribution we used only the results from the Scherrer equation on XRD spectra (results reported in paragraph 3.3.1.4).

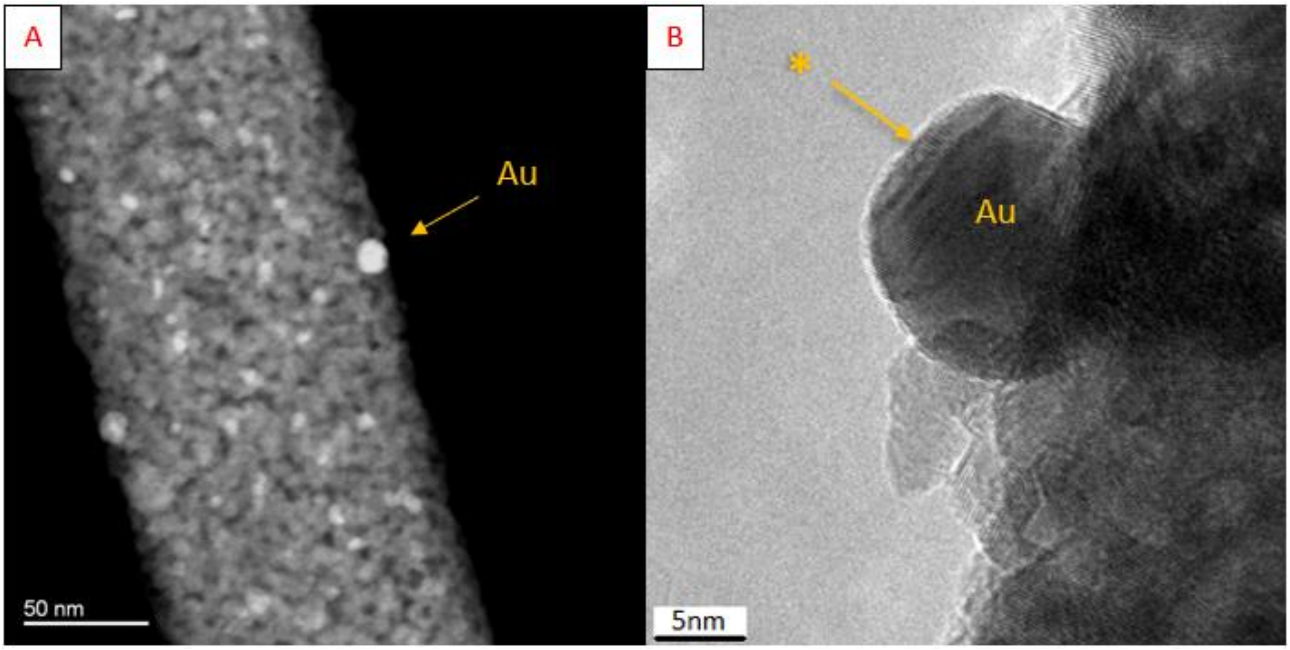

Figure 74: Au nanoparticles on the sample Au/CeO_2-NF_550 (A) and a closer view of a nanoparticle with the characteristic Au lattice fringes highlighted by the asterisk(B)

3.3.1.3 *Evaluation of PVP leftovers on the catalyst sample Au/CeO2-NF_300*

The analysis on catalyst Au/CeO_2-NF_300 sample (Figure 75), resemble the same pattern of the previous analysis on CeO_2-NF_300, with a weight loss of 4% in total, 2% before 100°C, due to water absorbed and another 2% during the rest of the heating. Given the facts, we can confirm that the second heat treatment at 300°C after the DP process is not sufficient to remove all PVP leftovers.

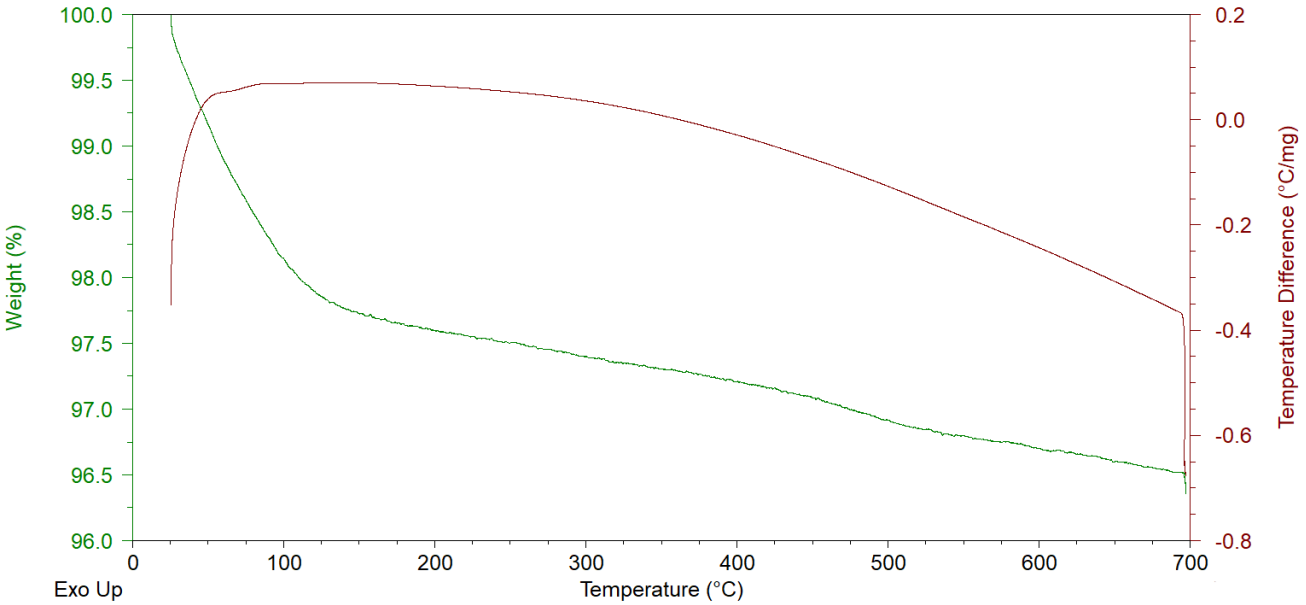

Figure 75: TGA analysis of sample Au/CeO_2-NF_300

3.3.1.4 XRD analysis of CeO_2-NF samples

The XRD analysis on the nanofibers support and catalyst prepared via DP (Figure 76, the spectrum of the sample Au/CeO_2–C, blue line, have been added for the comparison) shows the characteristic peaks of the fluorite-type structure of crystalline ceria, as listed above in paragraphs 3.1.1, and indicate the success of the electrospinning and calcination process, no other crystal phases have been recorded. The relative intensities and positions of the various peaks remained unchanged before and after the DP process, a sign that the synthesis of the catalyst did not change the crystalline structure of the supports.

Is possible to notice that the samples CeO_2-NF_300 and Au/CeO_2-NF_300 have broader peaks than the others, the broadening is due to the smaller size of the crystallites, which have been calculated through Scherrer and equal on average of 7and 8nm respectively, smaller than the crystallites of the fibres calcined at 550°C (dimension of the crystallites are reported in Table 11, Figure 77).

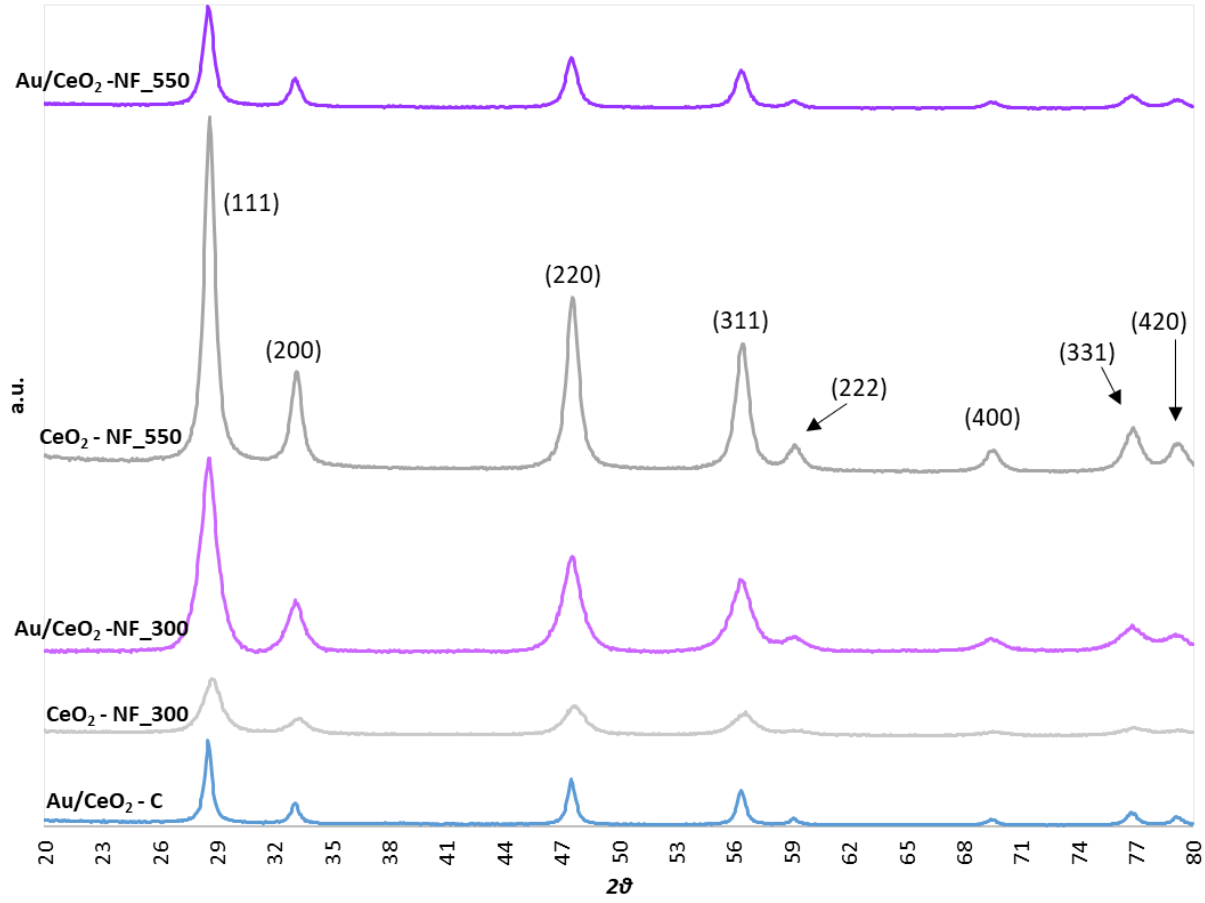

Figure 76: XRD patterns of the samples of nanofibers

The dimension of the crystallites in each crystal plane has been calculated through Scherrer's equations to highlight possible preferential grooving on the crystalline plane, the results have been reported in Figure 77. No preferential growing has been detected for the nanofibers samples; is possible to notice the Ostwald ripening due to the calcination process at the higher temperature, which caused the formation of bigger crystallites on the samples which support was calcined at 550°C (CeO_2-NF_550 and Au/CeO_2-NF_550, Figure 77) than the samples with the support calcined at 300°C (CeO_2-NF_300 and Au/CeO_2-NF_300).

Sample	Average dimension of the ceria crystallites (nm)
Au/CeO_2-NF _550	12
CeO_2-NF _550	12
Au/CeO_2-NF_300	8
CeO_2-NF_300	7
Au/CeO_2-C	18

Table 11: Average dimensions of the ceria crystallites from Scherrer

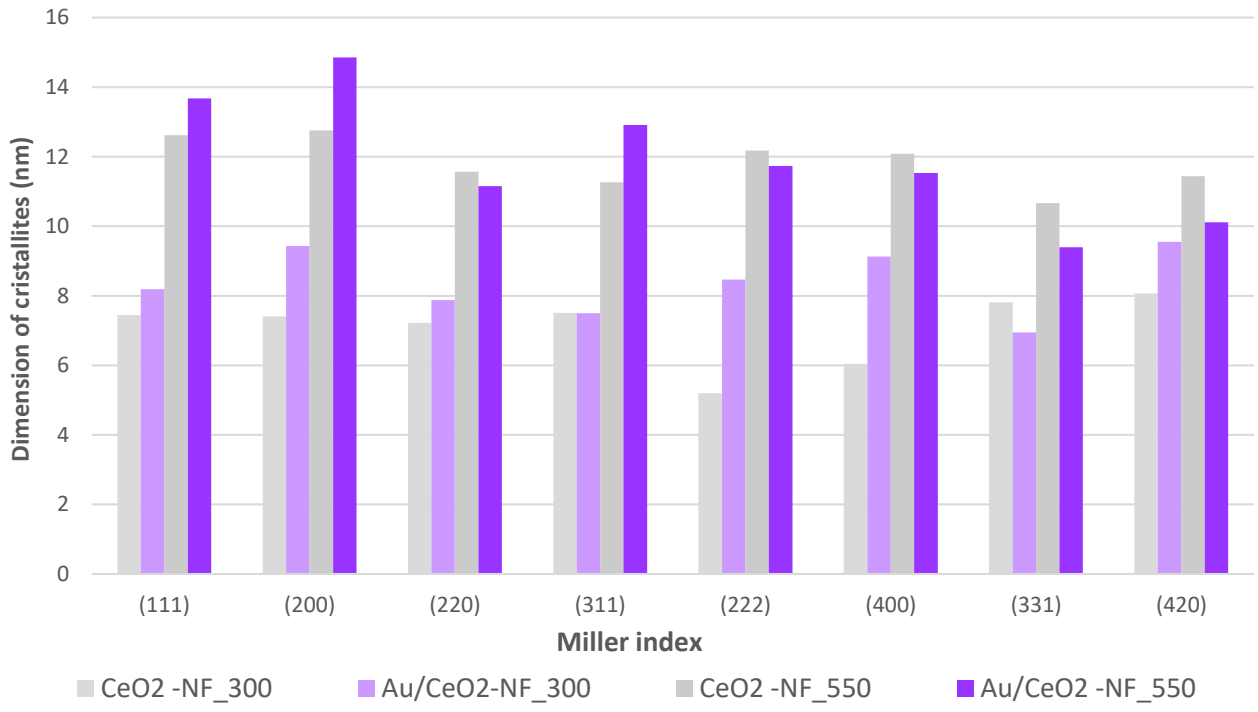

Figure 77: Dimension of crystallites of the different crystal planes in the samples CeO_2-NF spun without chloroauric acid

The relative peak intensities of the nanofibers samples have been compared to a reference tabulated ceria structure (reference code: 00-043-1002) and the results are reported in Figure 78. No relevant differences have been detected in the exposure of the reticular planes except for planes (220) and (311) of the samples CeO_2-NF_300 which seems to be less exposed for around 8%.

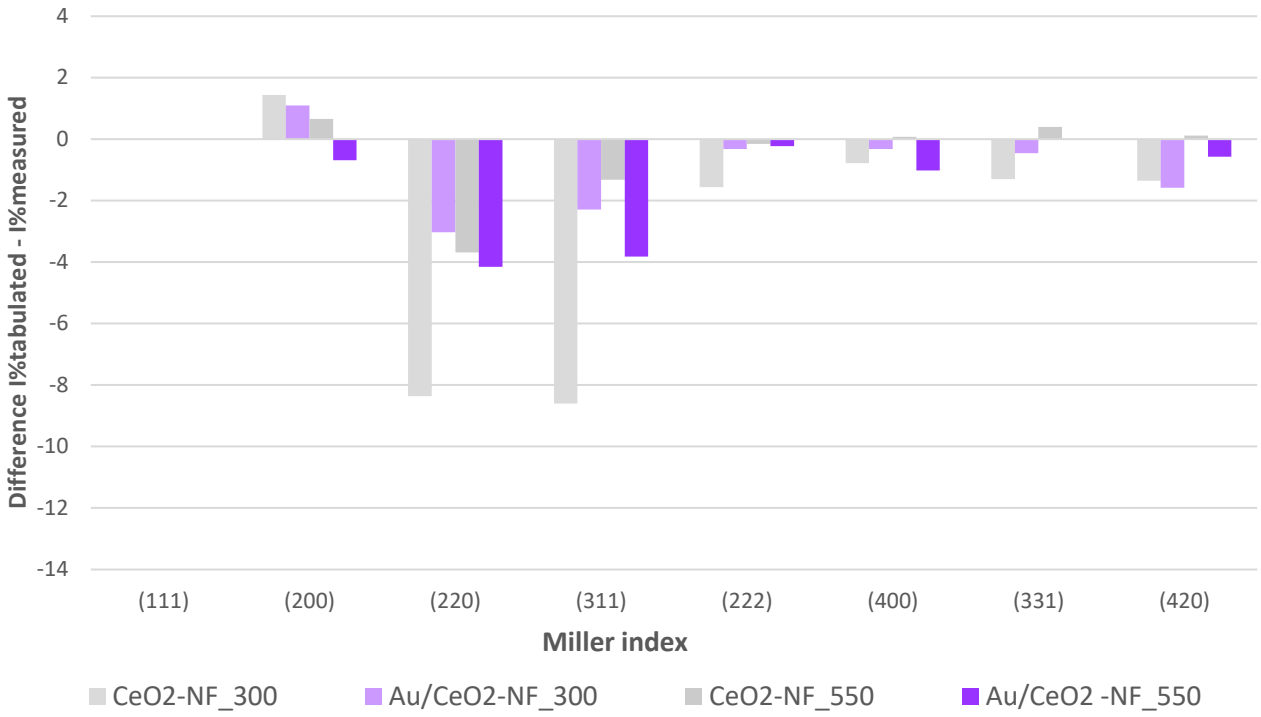

Figure 78: Differences between the intensities tabulated and measured for samples CeO_2-NF spun without chloroauric acid (tabulated intensities reference code: 00-043-1002)

The detailed XRD analysis between 36 and 41 *2θ* (Figure 79) shows clearly the diffraction peak of the crystalline plane (111) of gold nanoparticles on the catalyst samples in nanofibers prepared via DP.[13] The Scherrer equation was used again to calculate the dimensions of crystallites that have been reported in the following Table 12 and compared with the results of the crystallites sizes on the commercial samples from chapters 3.1.1 and 3.2.1.

Catalyst	**Average dimension of the gold crystallites (nm)**
Au/CeO_2-NF _550	8
Au/CeO_2-NF_300	7
Au/CeO_2-C	6
Au/ CeO_2-HS	<5

Table 12: Average dimensions of the gold crystallites from Scherrer

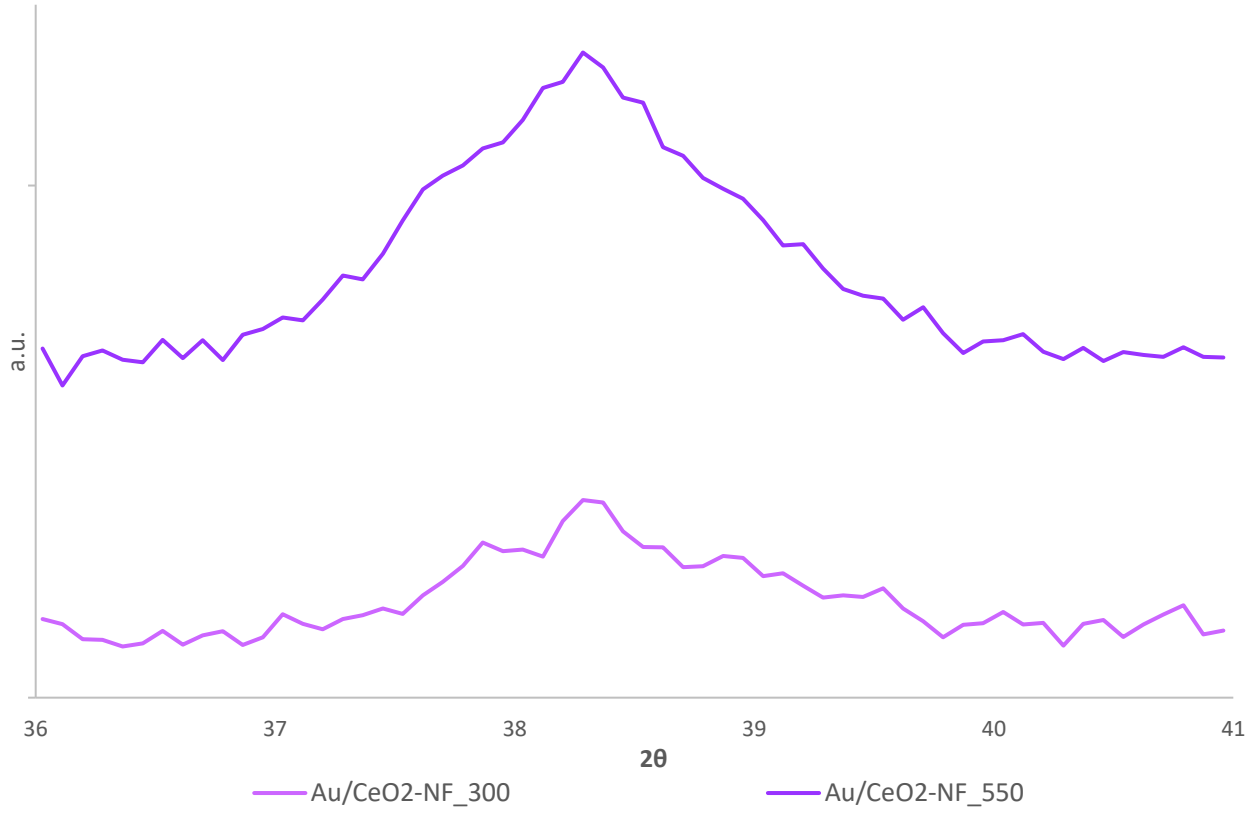

Figure 79: XRD analysis of the catalyst samples in nanofibers 36 and 41 2θ

3.3.1.5 Raman analysis of CeO_2-NF samples

In Raman spectra of nanofibers samples of supports and catalysts prepared via DP (Figure 80), it is possible to identify the characteristic peaks of cerium oxide, a sign that the calcination step has given the desired crystalline phase. The main peaks of cerium oxide after DP (the two purple spectra) are visibly enlarged and shifted to smaller cm^{-1}, this is a sign of the presence of Au nanoparticle on the support[14]. (Figure 80-A and Figure 81).

Is possible to notice a decreasing in the D-band with the increasing of the calcination temperature (Figure 80-B) on the two nanofibers support (grey spectra), this is due both to the diminishing of the defects in the ceria structure and the sintering of the supports, that leads to a lower surface area.[6,24] The D-band on the catalyst with Au nanoparticles seems to have a counter-intuitive changing regarding the Au deposition on the defects previously cited (chapter 3.2.2), this is probably due to the high fluorescence on the samples, in particular for the fluorescence of sample Au/CeO_2-NF_550 (dark purple spectrum) that was difficult to correct.

On the samples Au/CeO_2-NF_300 is present the signal at 835cm^{-1} due to traces of soluble impurities, probably chlorides, previously mentioned (chapter 3.2.2). The secondary 2TO band to 1180cm^{-1} is shifted to minor Raman shift, this could be due to the presence of traces of carbonates chemisorbed on the ceria surface or small leftovers of nitrates, which peak around 1060cm^{-1}. [14,25,26,32]

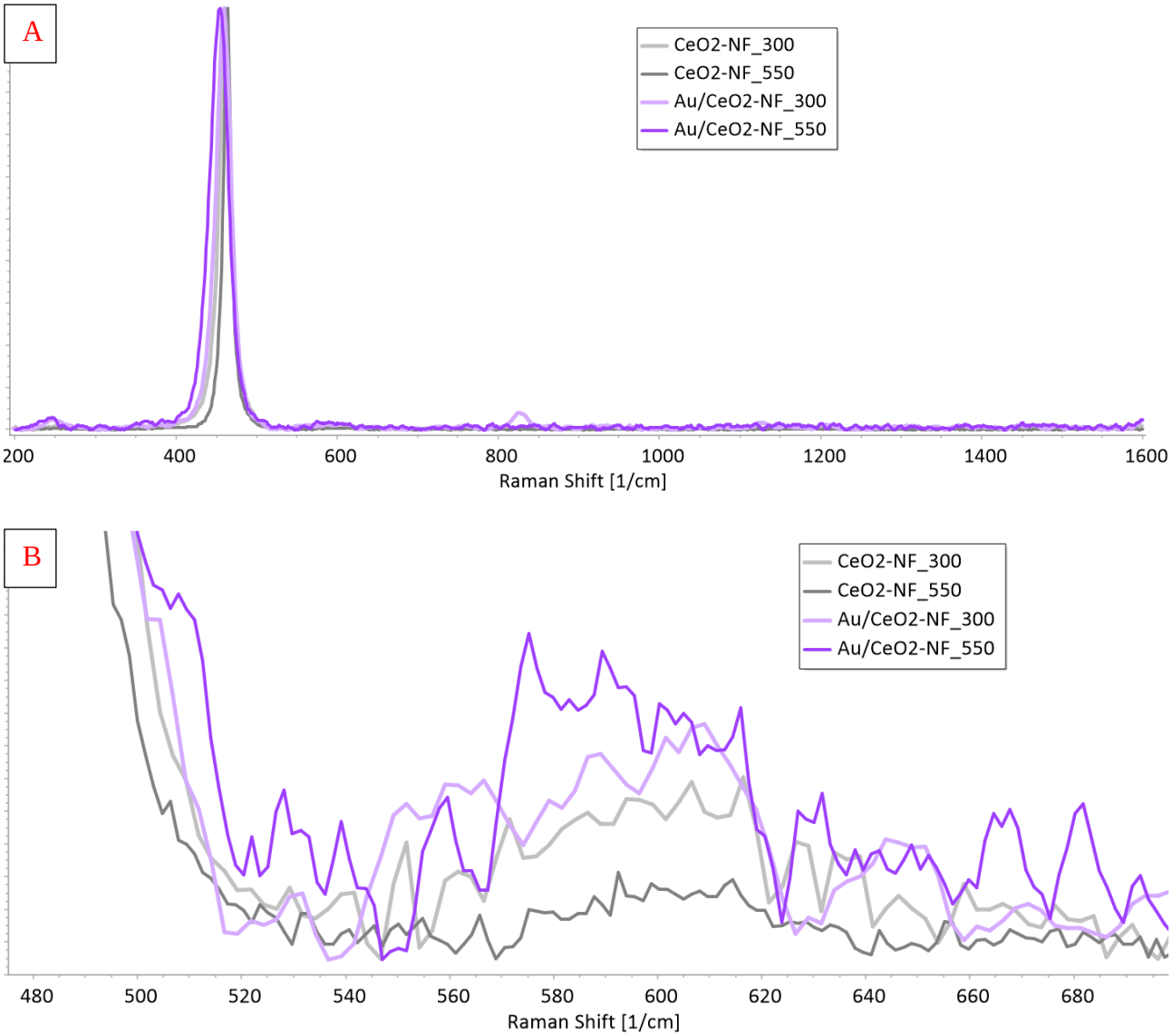

Figure 80: Raman spectra of nanofibers samples between 200 and 1600 cm^{-1} (A) and magnification on the D-band and the main peak region (B)

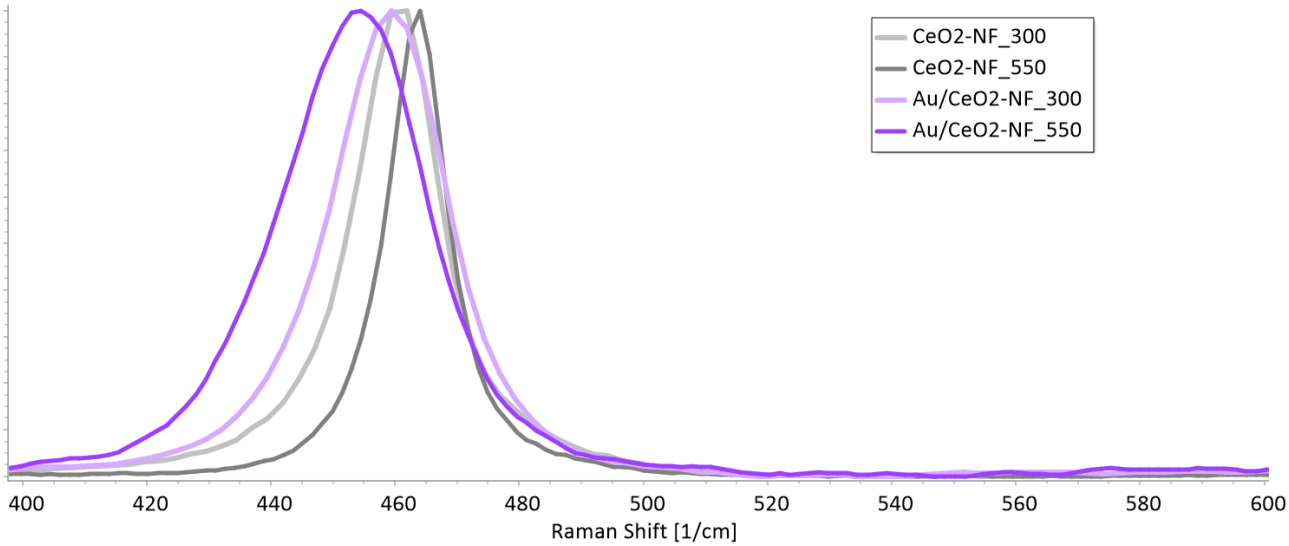

Figure 81: Raman spectra of nanofibers samples between 400 and 600 cm^{-1}

3.3.1.6 DRUV-Vis analysis of CeO_2-NF samples

The spectra of the DRUV-vis analysis on nanofibers samples are reported in Figure 82. The catalyst prepared via DP (the two purple curves) show the band of the plasmonic resonance of gold nanoparticles around 570nm (maximums highlighted in Figure 83, for comparison the position of the maximum of the sample Au/CeO_2-300 has been added too). The maximum of the plasmonic band depends on the dimension of the nanoparticles, while the broadness and the intensity of the peak depends on their polydispersion, in particular: a redshifted peak is due to bigger nanoparticles and a broadening of the peak is caused by a higher polydispersion.

The samples Au/CeO_2-NF_300 and Au/CeO_2-NF_550 present the maximum of their plasmonic bands at 565 and 580nm respectively. The two bands are more redshifted than the band of the catalyst Au/CeO_2-NF_300 supported on commercial ceria. These data are in accordance with the dimension of the nanoparticles calculated from XRD using the Scherrer equation because the smaller nanoparticles detected at the XRD are associated with a higher wavelength of the plasmonic band of the sample.[18,19,21,22]

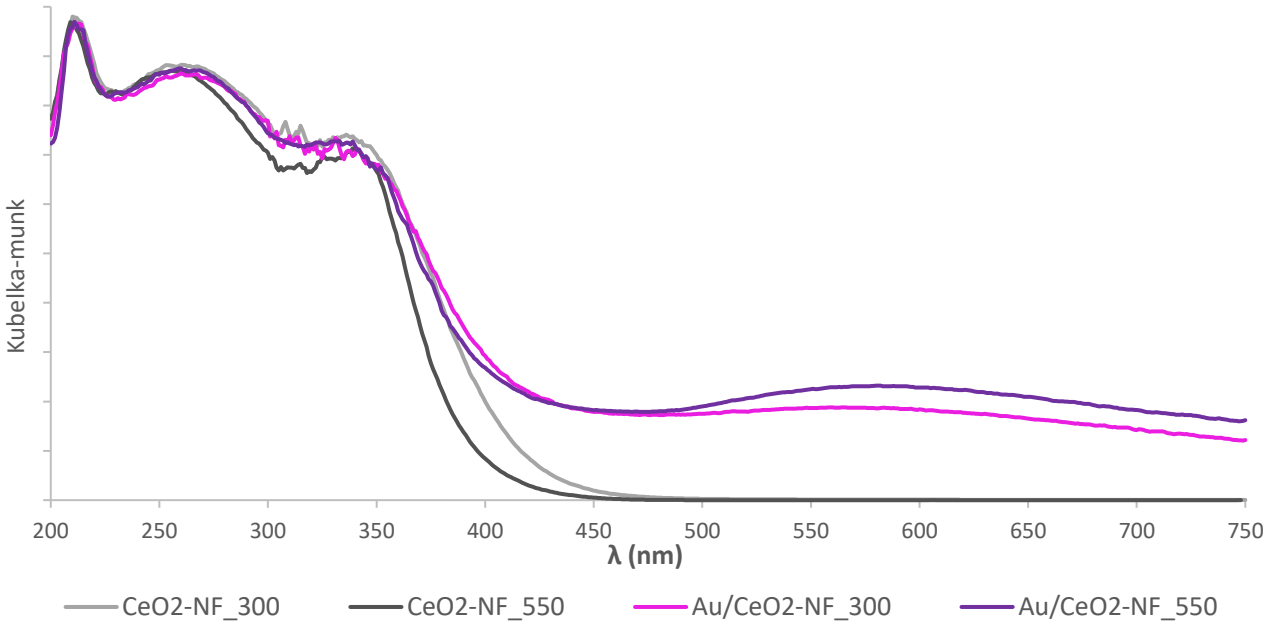

Figure 82: DRUV-Vis on CeO_2-NF samples

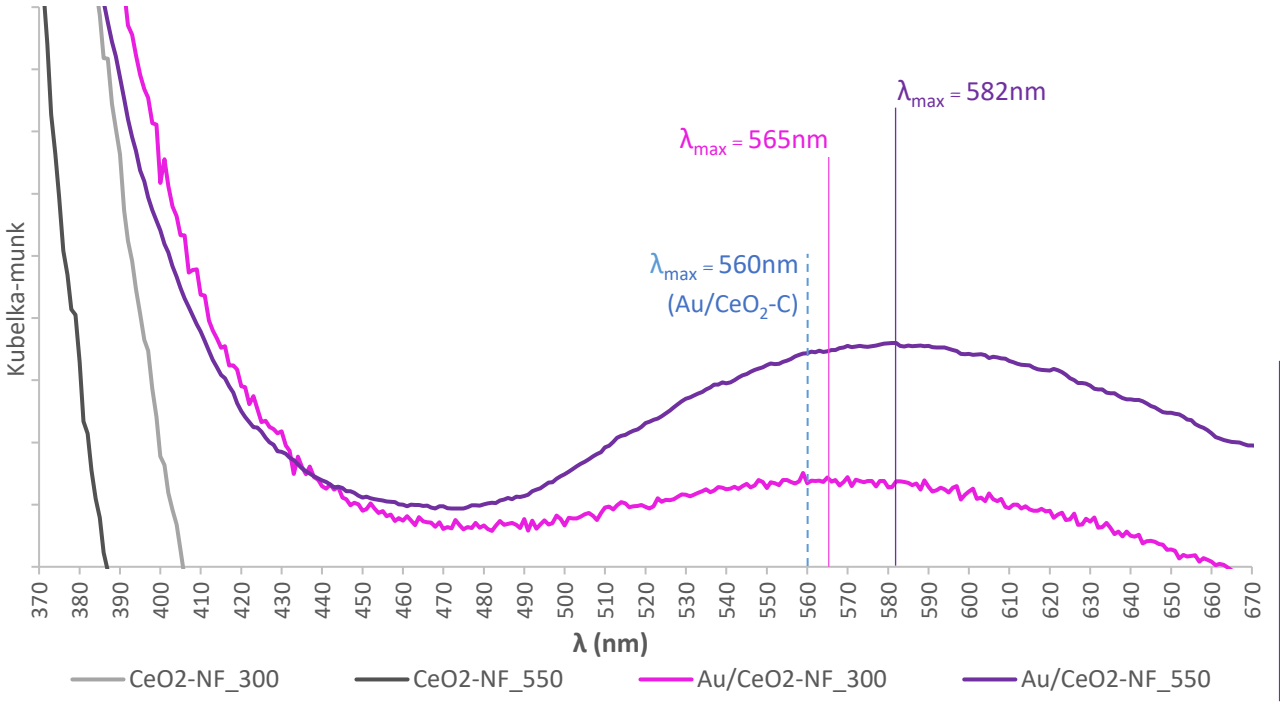

Figure 83: DRUV-Vis spectra of CeO_2-Nanofibers samples between 370nm and 740nm

Comparing the relative intensity of the spectra at 235nm and 260nm (Figure 84) is not possible to clearly notice the different amount of Ce^{3+} and Ce^{4+} in the samples.

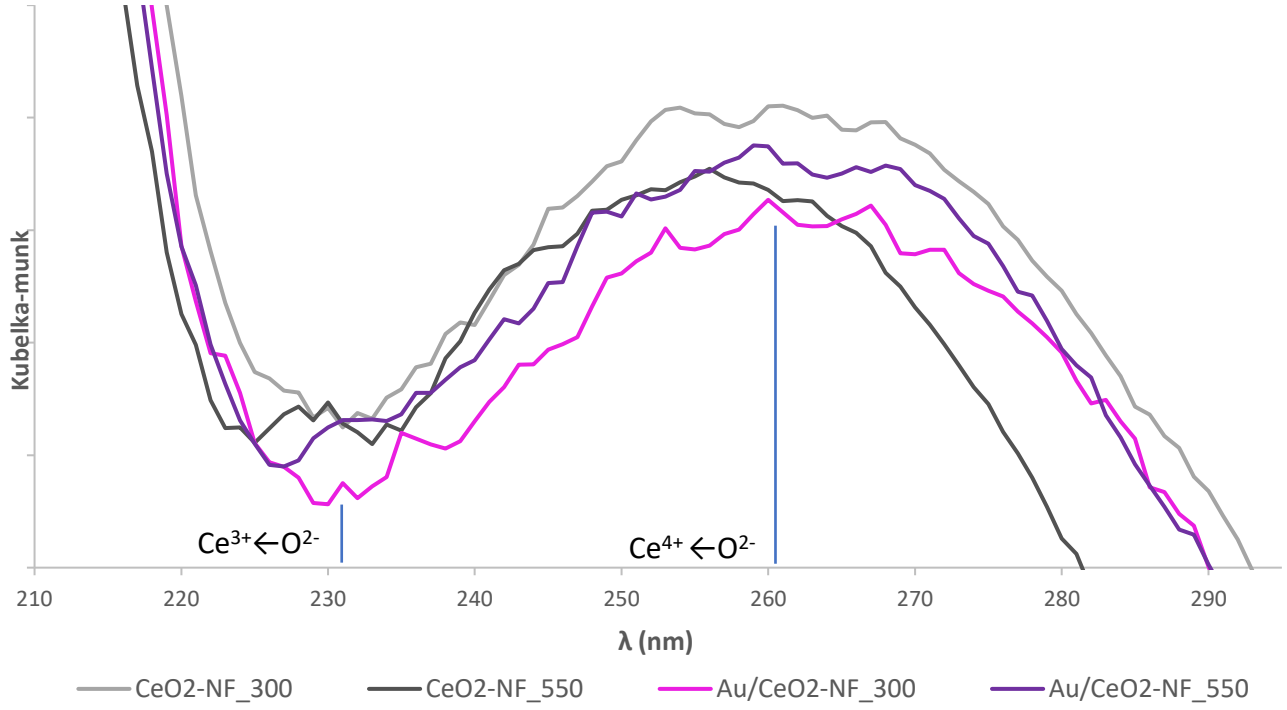

Figure 84: DRUV-Vis spectra of CeO_2-Nanofibers samples between 210nm and 290nm

3.3.1.7 Catalytic tests on CeO_2-NF samples prepared via DP

The results for the catalytic test for the gold catalyst supported on ceria nanofibers prepared via DP are reported over time in the following Table 13 and Figure 85, for the tests performed at 70°C, and in Table 14 for the tests performed at 80°C.

The presence of the catalysts leads to complete conversion of HMF, as for the other catalysts supported on commercial cerium oxide (chapters 3.1.4 and 3.2.4), the catalysts prepared trough the DP process lead to the maximum yield in HMFCA after 2 hours of reaction time, presence of residual FFCA does not exceed over 5%, probably almost all the FFCA produced is converted to FDCA. The yield in FDCA increases over time and reach 53% after 4 hours of reaction time with the sample Au/CeO_2 -NF_300, while less than half of it is formed using the catalyst Au/CeO_2 -NF_550 in the same conditions. The carbon loss diminishes over the reaction time, in particular, it shows a marked decreasing after 1 hour of reaction time while the yield in FDCA at the same time is comparable with the yield in FDCA in the blank after 4 h of reaction.

Catalyst	time (h)	X HMF (%)	Y HMFCA (%)	Y FFCA (%)	Y FDCA (%)	Carbon Loss (%)	Note:
blank	4	94	28	6	4	57	Neither support nor catalyst
blank	4	Not injectable due to side products					Blank, only CeO_2-NF_300°C
blank	4	Not injectable due to side products					Blank, only CeO_2-NF_550°C
Au/CeO_2 -NF_300	1	100	77	3	4	16	
	2	100	67	2	28	3	
	4	100	47	0	53	0	
Au/CeO_2 -NF_550	1	100	68	0	4	27	
	2	100	77	5	13	5	
	4	98	70	4	21	3	

Table 13: Catalytic test results overtime of the catalyst in nanofibers prepared via DP, T= 70 °C

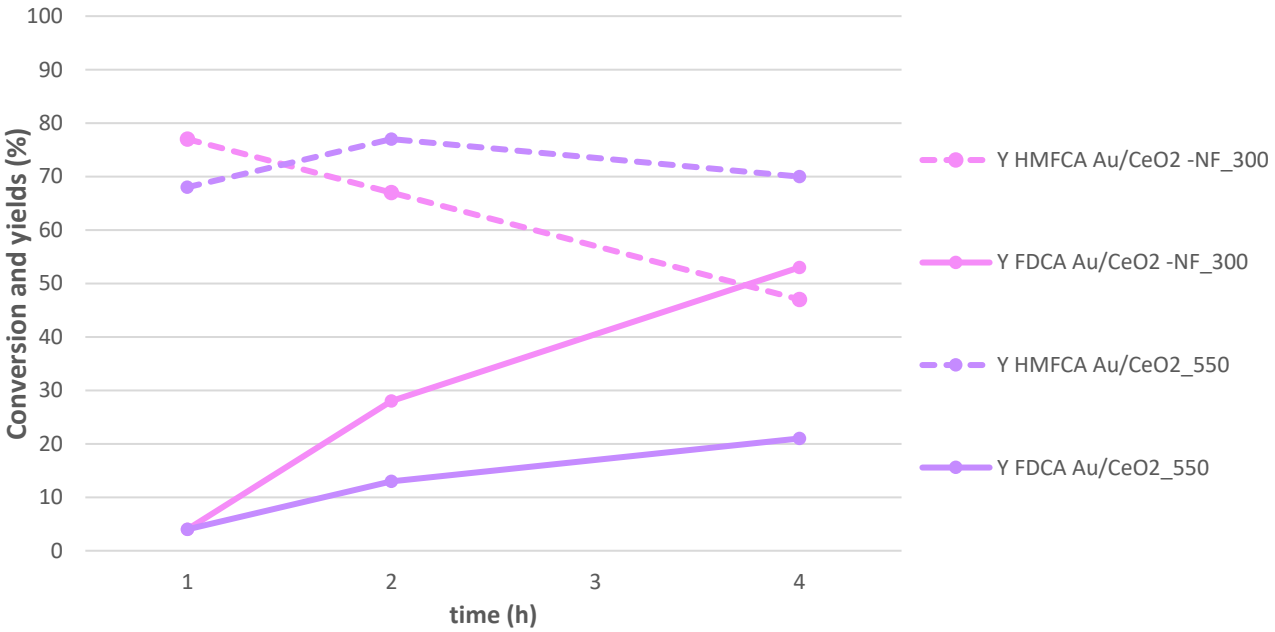

Figure 85: Conversion and products yields as a function of time for the catalyst in nanofibers prepared via DP, T=70 °C

The catalytic performance for the same reaction performed at 80°C (Table 14 and Figure 86) resemble the same pattern recorded at 70°C, but higher yield and better selectivity in the desired product are obtained. The reaction proceeds better over HMFCA, its yields are, in fact, lower compared to the yields obtained at 70°C. Both the yield in FDCA and the carbon loss are increased with the increasing of the temperature for the sample Au/CeO_2-NF_550, while a diminishing in carbon losses and an increasing in the yield of FDCA is recorded for the sample Au/CeO_2 -NF_300.

Catalyst	time (h)	X HMF (%)	Y HMFCA (%)	Y FFCA (%)	Y FDCA (%)	Carbon Loss (%)	Note:
blank	4	94	28	6	4	57	Neither support nor catalyst
Au/CeO_2 -NF_300	1	100	61	4	25	10	
	2	100	42	2	54	2	
	4	100	44	1	55	0	
Au/CeO_2 -NF_550	1	98	51	6	3	40	
	2	100	68	1	17	14	
	4	100	59	3	24	13	

Table 14: Catalytic test results overtime of the catalyst in nanofibers prepared via DP, T= 80 °C

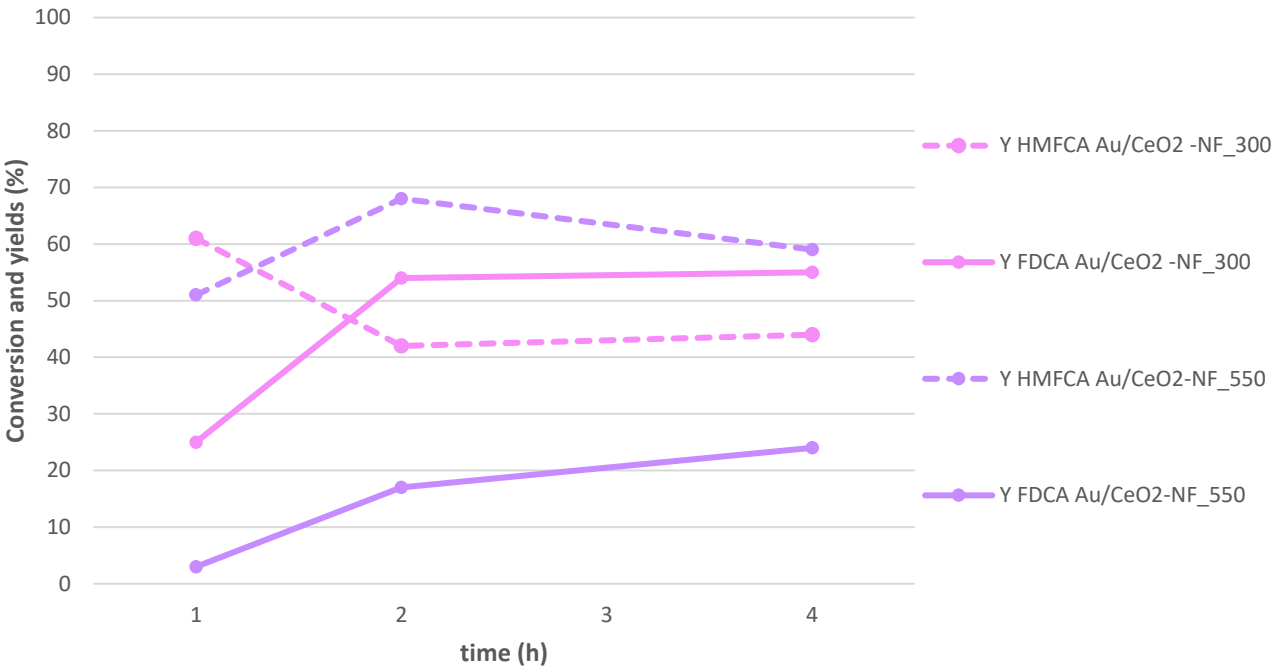

Figure 86: Conversion and products yields over time for the catalyst in nanofibers prepared via DP, T=80 °C

3.3.2 *Synthesis of ceria nanofibers containing gold precursor via electrospinning*

In this part of the work, the gold nanoparticles precursor were directly inserted in the spinning solution for the electrospinning process. In this case, the main problem to solve was to succeed in the elimination of PVP controlling the growth of metal species.

Prepared materials are reported in Table 15:

Sample	Surface Area (m^2/g)	Sample description
Au/CeO_2-NF_C	76	Au on CeO_2 nanofibers prepared by electrospinning calcined at 300°C in air
Au/CeO_2-NF_PC	96	Au on CeO_2 nanofibers prepared by electrospinning calcined at 300°C in N_2 and 300 in air

Table 15: catalyst samples in nanofibers electrospun with gold precursor

Catalysts Au/CeO_2NF_C and Au/CeO_2NF_PC were electrospun using the same solution, containing the desired amount of chloroauric acid to obtain a catalyst with a metal loading of 1.5%wt. but they were thermally treated in different conditions. (scheme in Figure 87)

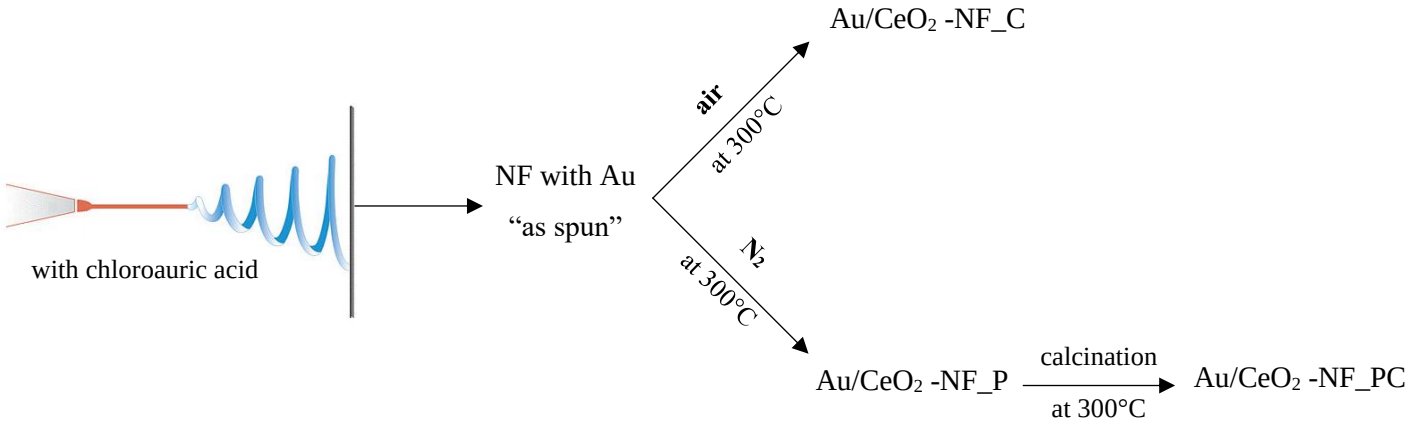

Figure 87: Scheme of the catalysts prepared by direct spinning with gold precursor

The result from the electrospinning process was not a fibre-like structure but a nano-belts structure with cross-section dimensions around 2x10µm (Figure 88).

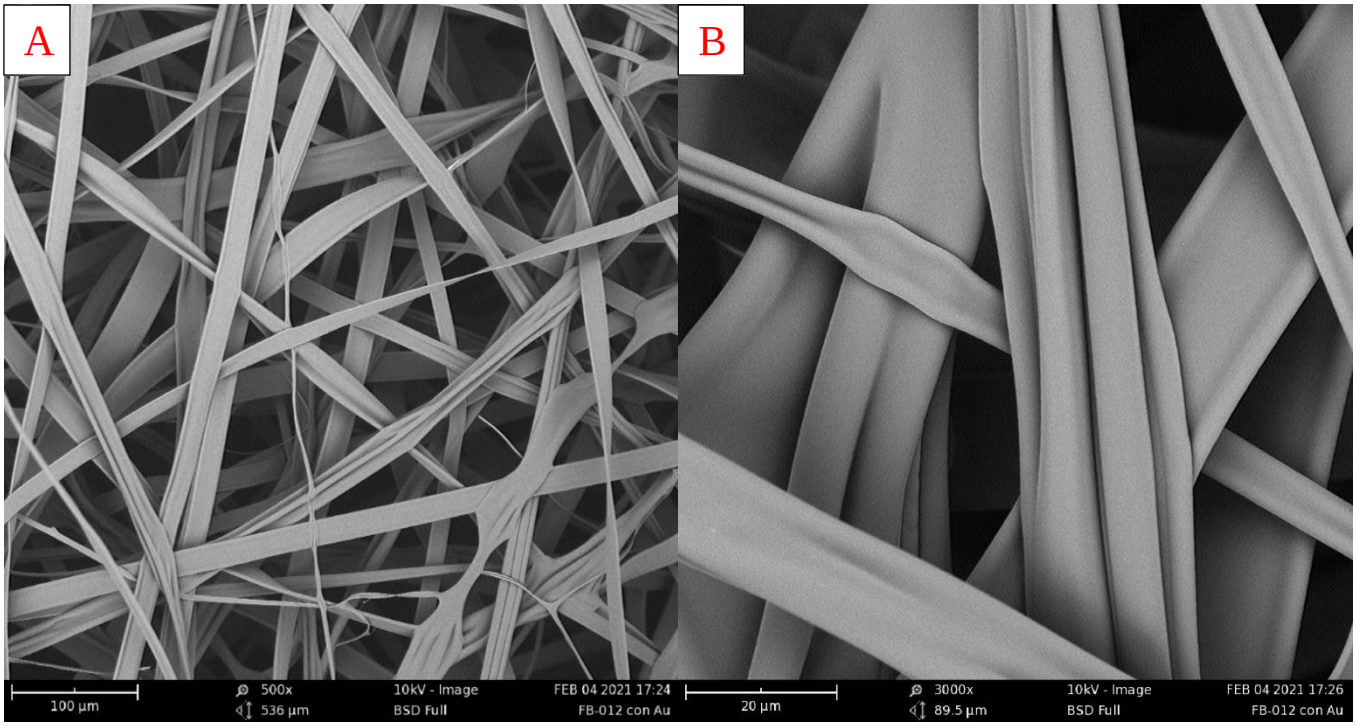

Figure 88: sample Au/CeO2-NF as spun (A) and at higher magnification (B)

This nano-belts micro-structure was probably due to the different conductibility of the solution, which was enhanced by the greater ions content introduced in it by the addition of chloroauric acid. To prepare the catalysts the sample was divided into two different batches, one has been labelled "Au/CeO_2-NF_C" been calcined with a heating ramp of 0.2°C/min and an isotherm maintenance at 300°C for three hours. The other one labelled "Au/CeO_2-NF_PC", has been first pyrolyzed in of N_2 (flow 80mL/min, heating ramp of 0.2°C/min and isotherm maintenance at 300°C for three hours). Then it followed the same calcination in air of the sample "Au/CeO_2-NF_C".

The double heat treatment of the sample "Au/CeO_2-NF_PC" was meant to be a more gently removal of the PVP in the structure of the catalyst, to study both the effect of the pyritization and to avoid localized temperature increases that could lead to an increasing in the dimension of the gold nanoparticles.

3.3.2.1 Thermogravimetric analysis of the calcination process on nanofibers spun with gold

The electrospun nanofibers comprised of gold, cerium nitrate and PVP were analysed via TGA. The analyses were carried out both in air and in nitrogen, to study the different behaviour of the samples.

The TGA performed in air shows three weight losses in the sample (Figure 89). The first one is a continuous loss due to water absorbed in the sample and is particularly evident around 100°C. The second one is settled at 240°C and correspond to a loss of 4% of the weight, it is due to a first structural degradation of PVP[33] . The third one is the most intense loss, it is settled at 300°C and corresponds to a loss of 45% of the weight, which is due to the PVP combustion. The final mass of the sample is 27% of the original mass. The fourth "step" in the temperature difference curve (brown plot) at 700°C is due to the thermal inertia of the system and not to a real change in the sample.

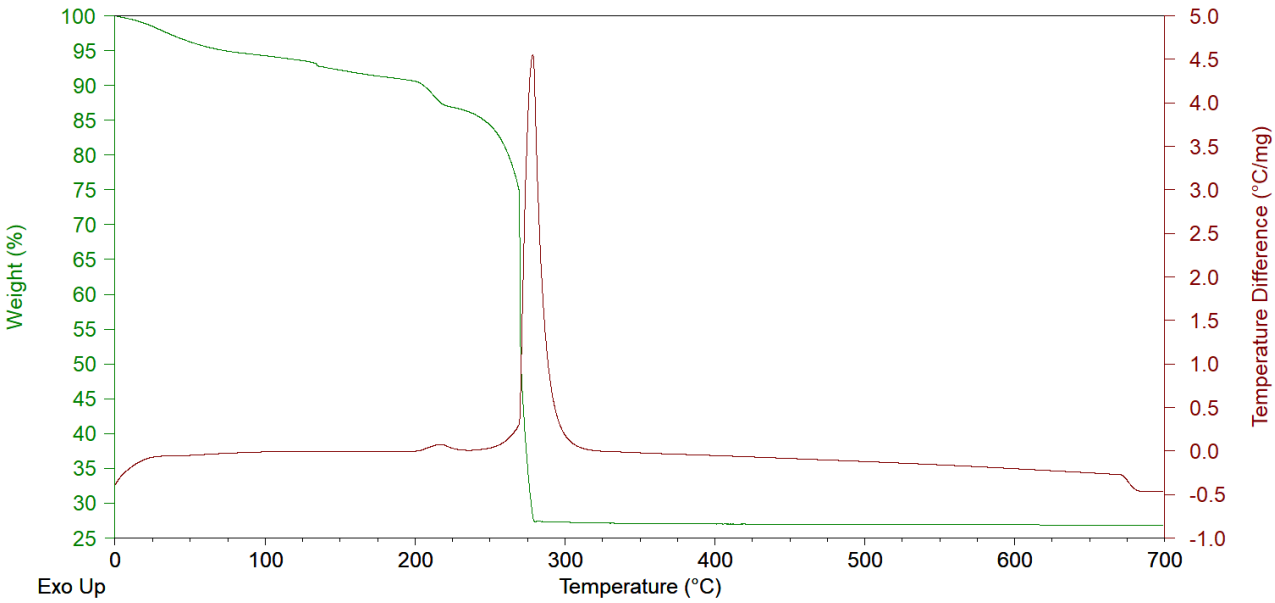

Figure 89: TGA/DTA analysis under airflow of the sample in NF with Au "as-spun"

The TGA performed under nitrogen flow shows four smooth weight losses followed by a continuous gently weight loss until the end of the analysis (Figure 90). The first, the fourth and the final continuous weight losses are associated with an endothermic peak in the curve of the temperature difference between the PAN of the sample and the reference one, the first weight loss is due to loss of water from the sample, the others two are given by desorption of pyrolysis oils formed during the process. The second and the third weight losses are due to the

degradation of Cerium nitrate and PVP on the samples. In particular, the fourth weight loss gives the most intense temperature increasing.

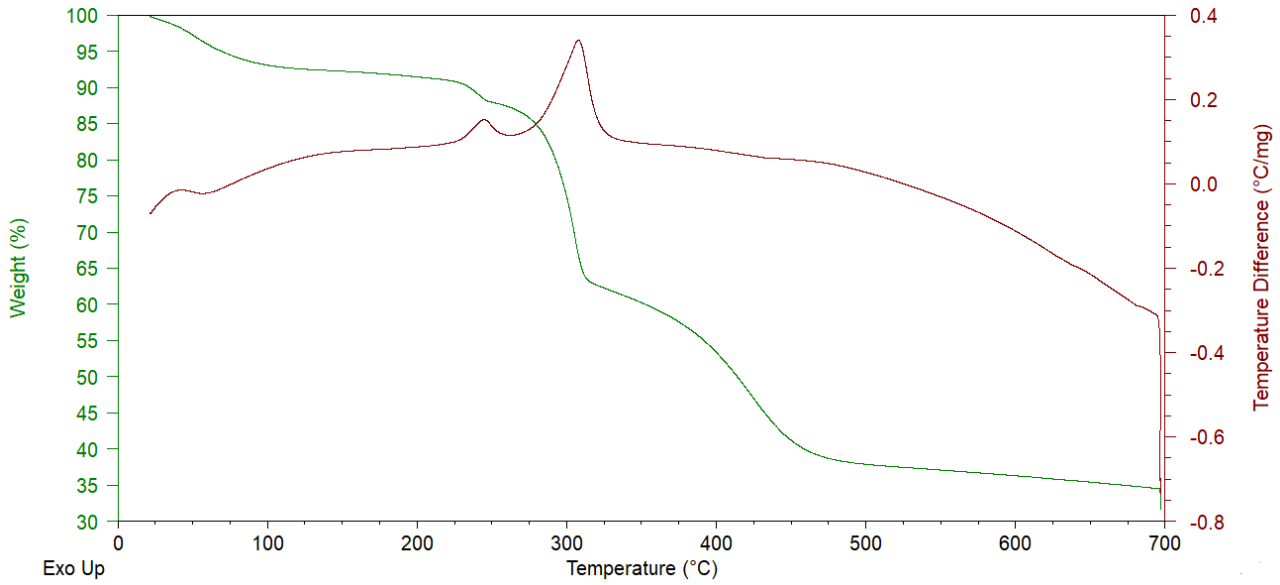

Figure 90: TGA/DTA analysis under N_2 flow of the sample in NF with Au "as-spun"

The TGA performed on the sample Au/CeO_2-NF_P under airflow (Figure 91) displays three weight losses for a total weight loss of 35% of the original weight. The first weight loss, around 100°C is associated with water absorbed in the sample, the second and the third weight losses, at 200°C and 300°C, these are caused by the thermal degradation of PVP and nitrates, this could be deduced by the positive peak in the DTA curve at the same temperature. The second weight loss in particular is associated with an intense positive peak in the DTA due to a strongly exothermic process.

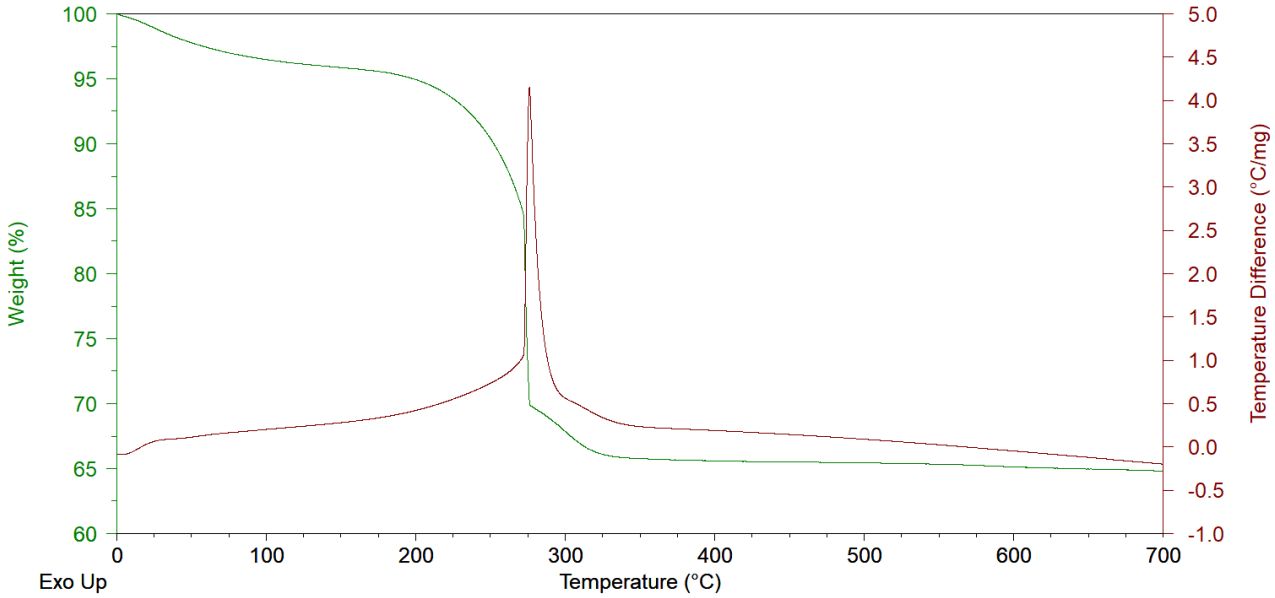

Figure 91: TGA/DTA analysis under airflow of the sample Au/CeO_2-NF_P

Looking at these results we decided to perform the calcination of the fibres spun with $HAuCl_4$ in air to prepare the sample Au/CeO_2-NF_C with a gentle heating ramp in a muffle with a rate of 0.2°C/min and three hours of isotherm maintenance, to not damage the nanofibers structure[1].

To prepare the sample Au/CeO_2-NF_P from the fibres spun with $HAuCl_4$ the heat treatment in N_2 flow have been performed with a heating rate of 2°C/min and three hours of isotherm maintenance.

The final heat treatment in air of the sample Au/CeO_2-NF_P to produce the sample Au/CeO_2-NF_PC has been performed in a muffle with a ramp of 0.2°C/min and three hours of isotherm maintenance, the purpose of this ramp was to avoid excessive temperature spikes which could lead to undesired growth of the gold nanoparticles.

3.3.2.2 ATR analysis on nanofibers spun with gold

The catalyst samples Au/CeO_2-NF_C and Au/CeO_2-NF_PC (black and green lines) have been analysed via ATR, the spectra are reported in Figure 92 with the other samples in nanofibers and the spectrum of the PVP for the comparisons.

The signal of PVP leftovers is still barely visible at 2930cm^{-1} on samples Au/CeO_2-NF_C and Au/CeO_2-NF_PC (highlighted by the yellow triangles in Figure 92).

The signal of residual PVP has not been detected in sample Au/CeO_2-NF_C however, as reported previously, PVP leftovers been detected via TGA in chapter3.3.2.1.

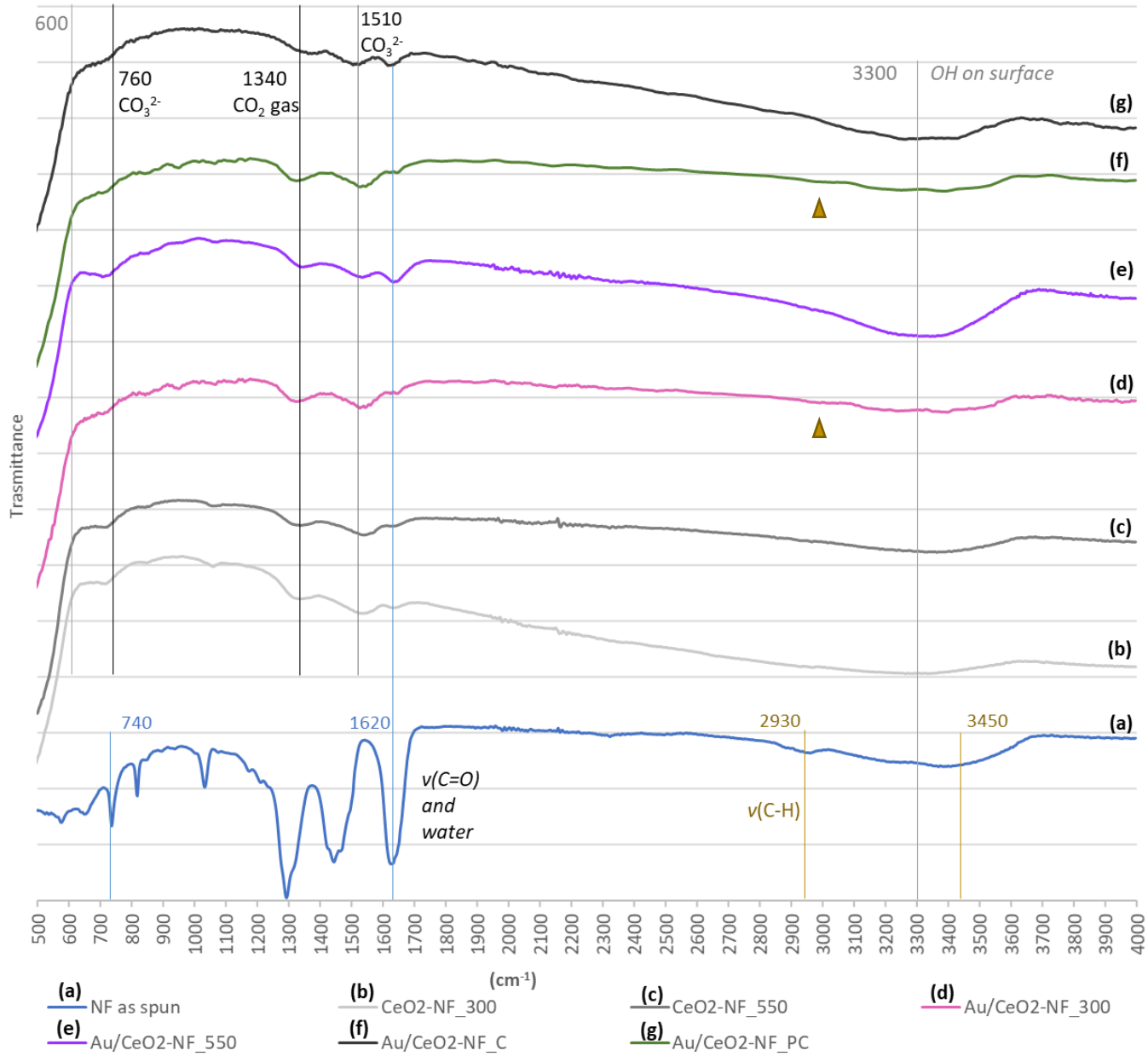

Figure 92: ATR spectra of the nanofibers samples

3.3.2.3 XRD analysis on nanofibers spun with gold

The XRD analysis on the sample of nanofibers and catalyst spun with gold (Figure 93, with the spectrum of the sample Au/CeO_2–C and, blue line, and the other sample in nanofibers have been added for the comparison) shows the characteristic peaks of the fluorite-type structure of crystalline ceria, as listed above in paragraphs 3.1.1, and indicate the success of the electrospinning and calcination process, no other crystal phases have been recorded.

The spectrum of the samples Au/CeO_2-NF_P (dark grey line, Figure 93) shows the characteristics peaks of cerium(IV) oxide too, this means that the heat treatment under N_2 flow at 300°C was sufficient to form the oxidic structure of ceria.

Is possible to notice that some of the samples have broader peaks than the others, this is particularly noticeable in the samples spun with chloroauric acid and for the nanofibers samples calcined only at 300°C.

The broadening is due to the smaller size of the crystallites, which have been calculated through Scherrer and was equal to 7nm and 4nm for the samples Au/CeO_2-NF_C and Au/CeO_2-NF_PC respectively, these are the smallest crystallites dimension measured in al the prepared nanofibers samples (dimension of the crystallites are reported in Table 16, Figure 94 and Figure 95). The overlapping in those samples is particularly evident on the peaks of the planes (331) and (420) that are almost completely overlapped.

The XRD on the samples spun with chloroauric acid revealed smaller nanocrystals (Table 16 and Figure 95), in particular on the samples Au/CeO_2-NF_P and Au/CeO_2-NF_PC than in the sample Au/CeO_2-NF_C (brown and green columns), this suggests that the two steps preparation process (heat treatment in N_2 followed by calcination) influenced the final dimension of the crystallites.

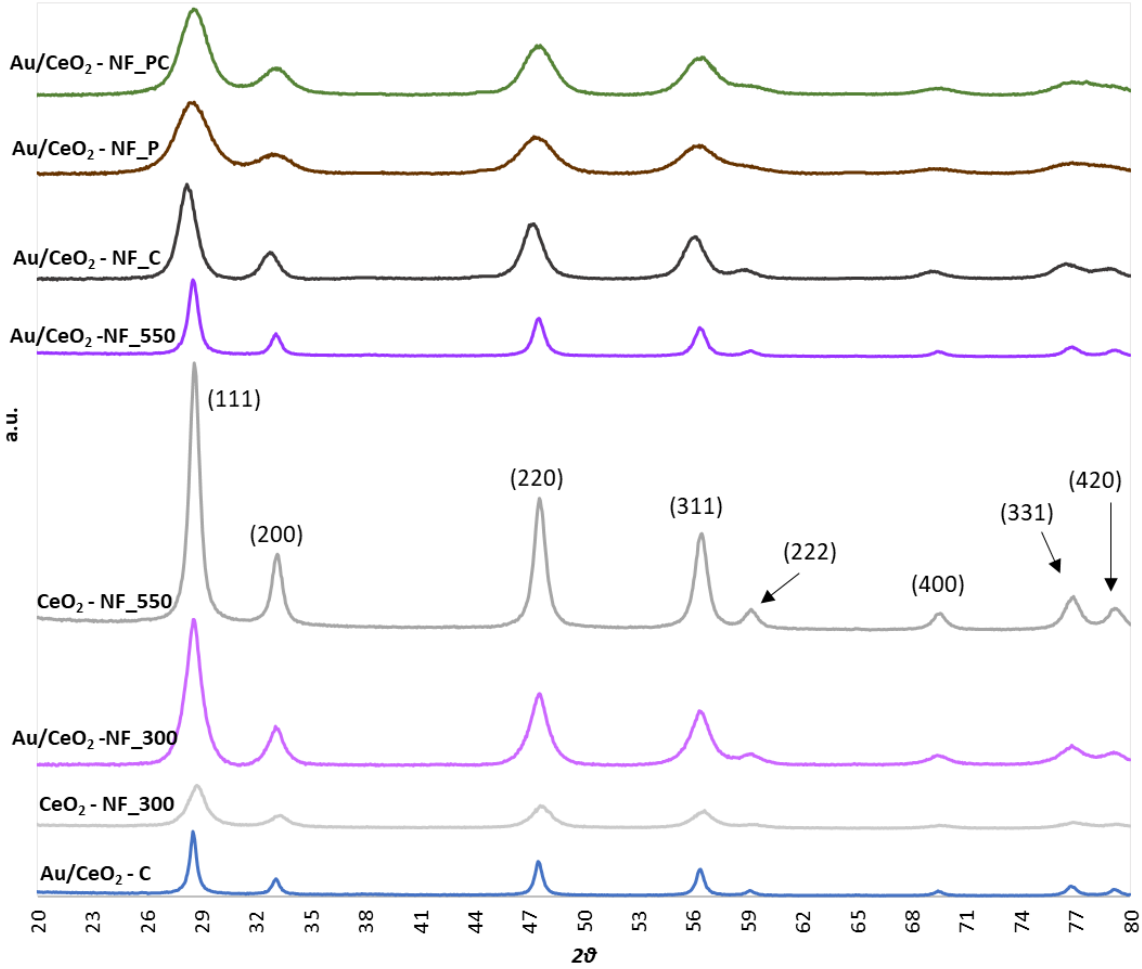

Figure 93: XRD patterns of the samples of nanofibers

Sample	Average dimension of the ceria crystallites (nm)
Au/CeO_2-NF _PC	4
Au/CeO_2-NF _P	4
Au/CeO_2-NF _C	7
Au/CeO_2-NF _550	12
CeO_2-NF _550	12
Au/CeO_2-NF_300	8
CeO_2-NF_300	7
Au/CeO_2-C	18

Table 16: Average dimensions of the ceria crystallites from Scherrer

The dimension of the crystallites in each crystal plane has been calculated through Scherrer's equations to highlight possible preferential grooving on the crystalline plane, the results have been reported in Figure 94 and Figure 95. No preferential growing has been detected for the nanofibers samples spun with and without chloroauric acid (Figure 95).

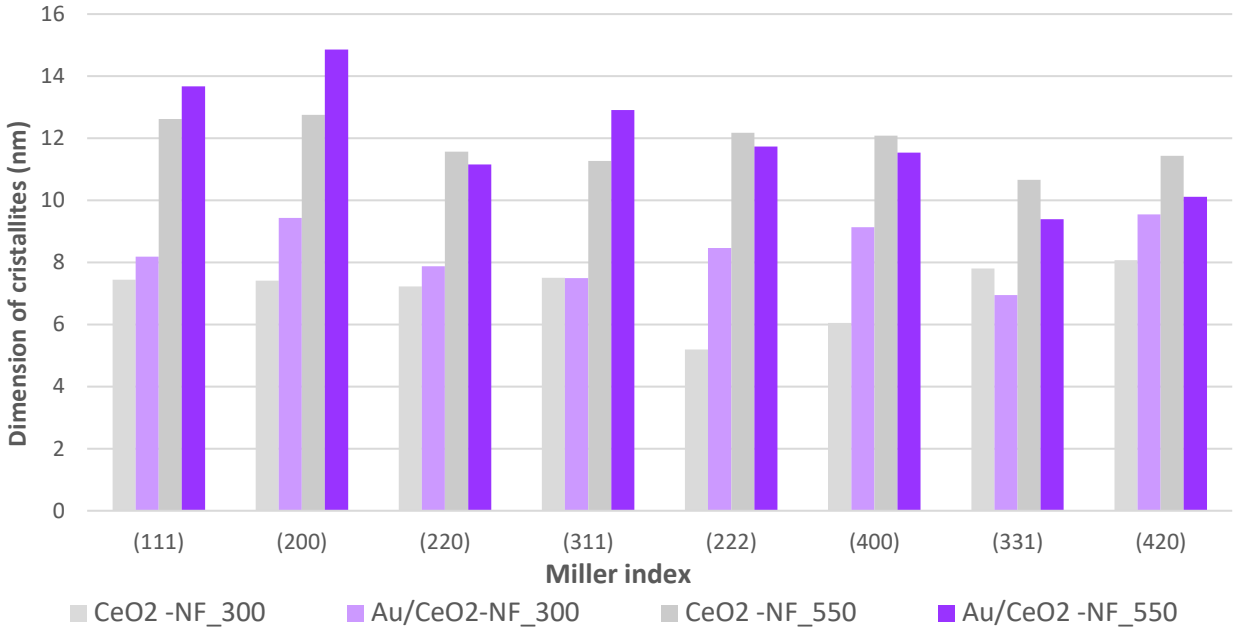

Figure 94: Dimension of crystallites of the different crystal planes in the samples CeO_2-NF spun without chloroauric acid

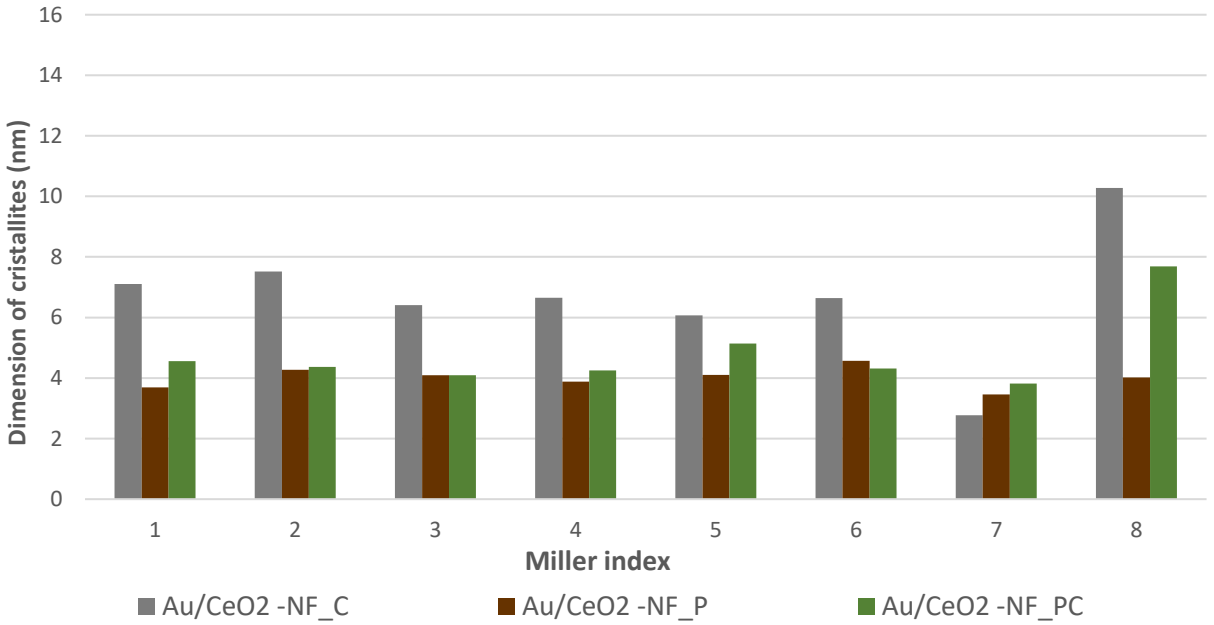

Figure 95: Dimension of crystallites of the different crystal planes in the samples CeO_2-NF spun with chloroauric acid

The relative peak intensities of the nanofibers samples have been compared to a reference tabulated ceria structure (reference code: 00-043-1002) and the results are reported in Figure 96 and Figure 97. No relevant differences have been detected in the exposure of the reticular planes except for planes (220) and (311), in particular for the samples CeO_2-NF_300, Au/CeO_2-NF _C and Au/CeO_2-NF _P, which seems to be less exposed for around 10%. Given the fact that the plane (220) is parallel to the plane (110), it could be that this plane in less exposed to. The plane (110) is visible only at small angles[10], a further SAXRD analysis could confirm this hypothesis.

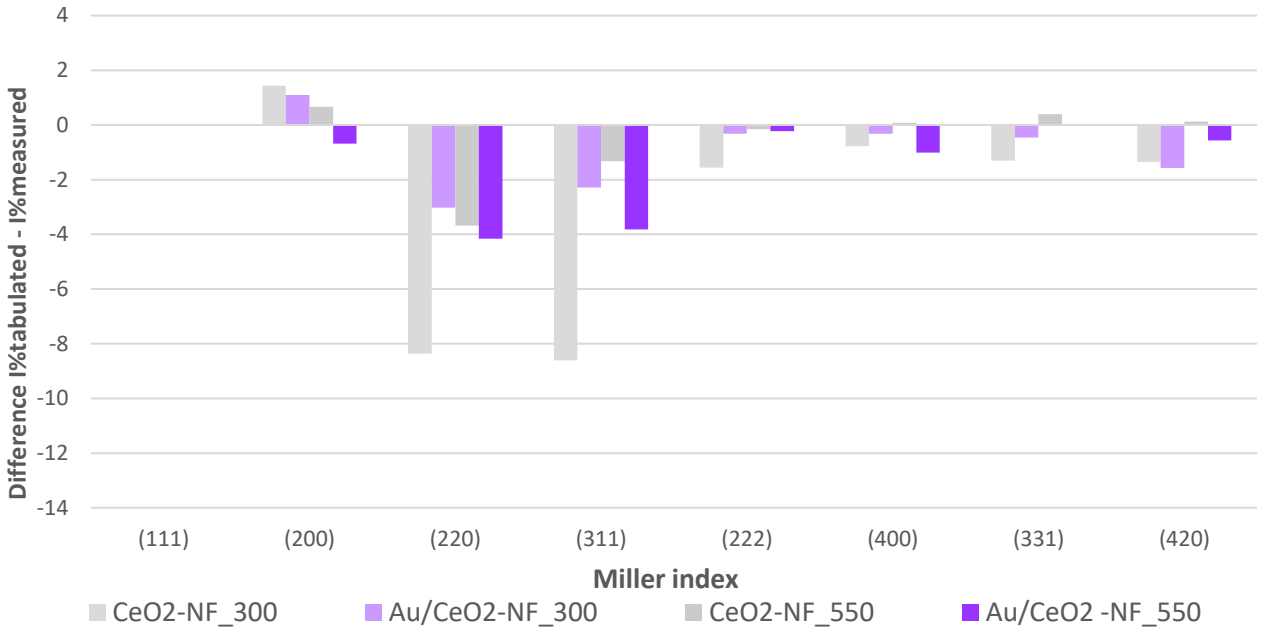

Figure 96: Differences between the intensities tabulated and measured for samples CeO_2-NF spun without chloroauric acid (tabulated intensities reference code: 00-043-1002)

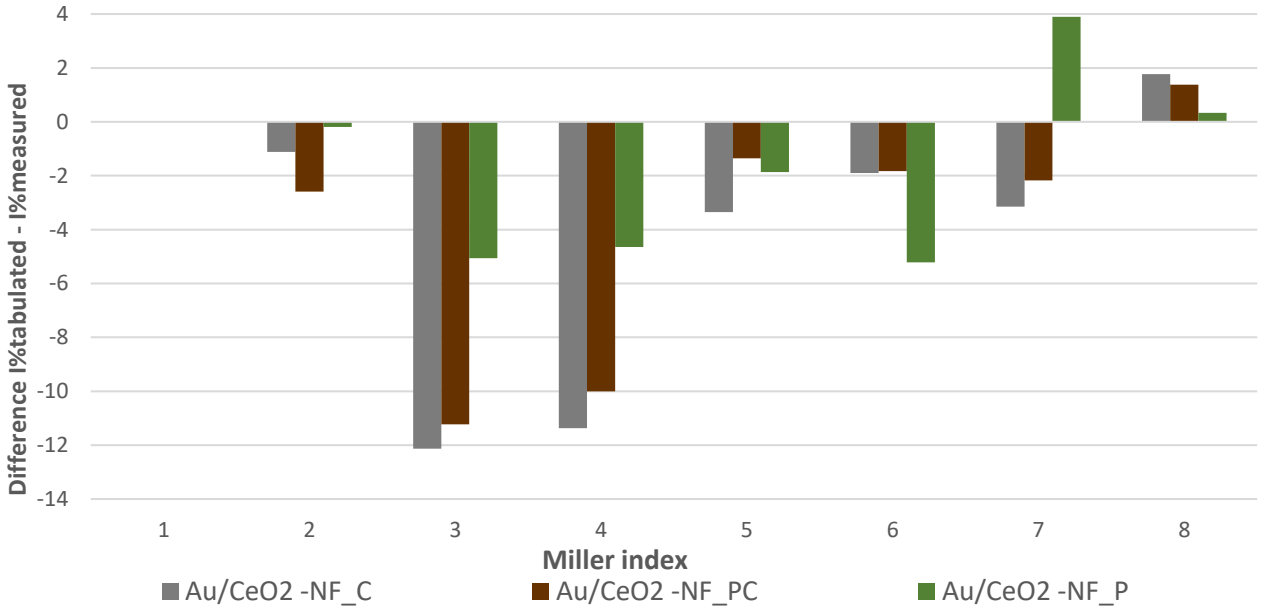

Figure 97: Differences between intensities tabulated and measured for samples CeO_2-NF spun with chloroauric acid (tabulated intensities reference code: 00-043-1002)

The detailed XRD analysis between 36 and 41 *2θ* (Figure 98) shows clearly the diffraction peak of the crystalline plane (111) of gold nanoparticles on the catalyst samples in nanofibers prepared via DP (the two purple curves) or directly spun with chloroauric acid (black and green curves).[13] The Scherrer equation was used again to calculate the dimension of crystallites that have been reported in the following Table 17 and compared with the results of the crystallites sizes on the commercial samples from chapters 3.1.1 and 3.2.1, is possible to notice that the border peaks are associated with the smallest crystallites size of the gold nanoparticles.

Catalyst	**Average dimension of the gold crystallites (nm)**
Au/CeO_2-NF _PC	24
Au/CeO_2-NF _C	20
Au/CeO_2-NF _550	8
Au/CeO_2-NF_300	7
Au/CeO_2-C	6
Au/ CeO_2-HS	<5

Table 17: Average dimensions of the gold crystallites from Scherrer

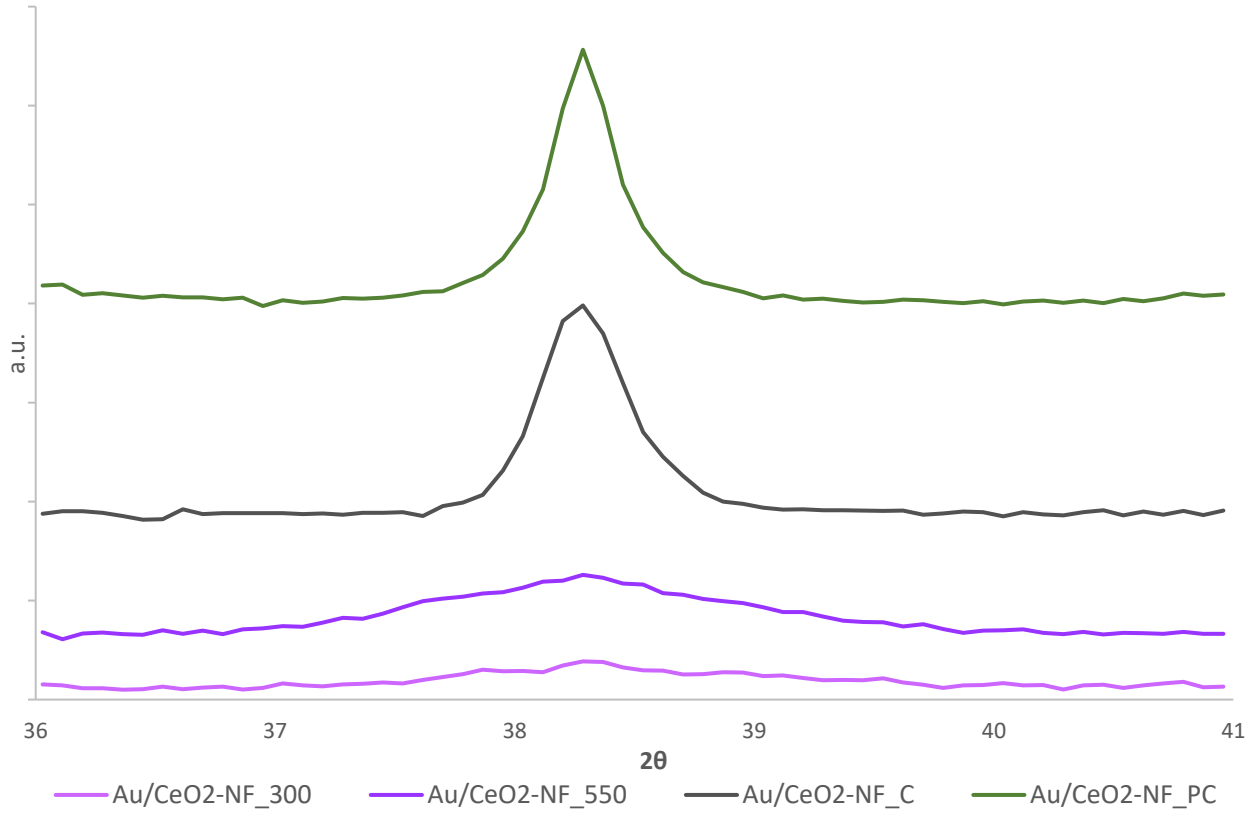

Figure 98: XRD analysis of the catalyst samples in nanofibers 36 and 41 2θ

3.3.2.4 Raman analysis on nanofibers spun with gold

In Raman spectra of nanofibers samples Au/CeO_2-NF_C and Au/CeO_2-NF_PC (dark grey and green lines, Figure 99) it is possible to identify clearly only the main characteristic peaks of cerium oxide, due to the strong fluorescence on the samples that were impossible to correct completely. The intense fluorescence was probably due to the relatively big gold nanoparticles deposited on the samples.

On the sample Au/CeO_2-NF_PC is present the signal at 835cm^{-1} due to traces of soluble impurities, probably chlorides, previously mentioned (chapter 3.2.2).

The two spectra have been compared with the Raman spectra of the other nanofiber samples (Figure 100).

The main peaks of cerium oxide of the catalyst in nanofibers prepared both via DP or via direct spinning with $HAuCl_4$ are visibly enlarged and shifted to smaller cm^{-1}, this is a sign of the presence of Au nanoparticle on the support[14] (Figure 100 A and C, the two purple, the dark grey and the green spectra).

The D-band of samples directly spun with Au (Figure 100 B, dark grey and green curves) are not comparable due to the high fluorescence on the samples.

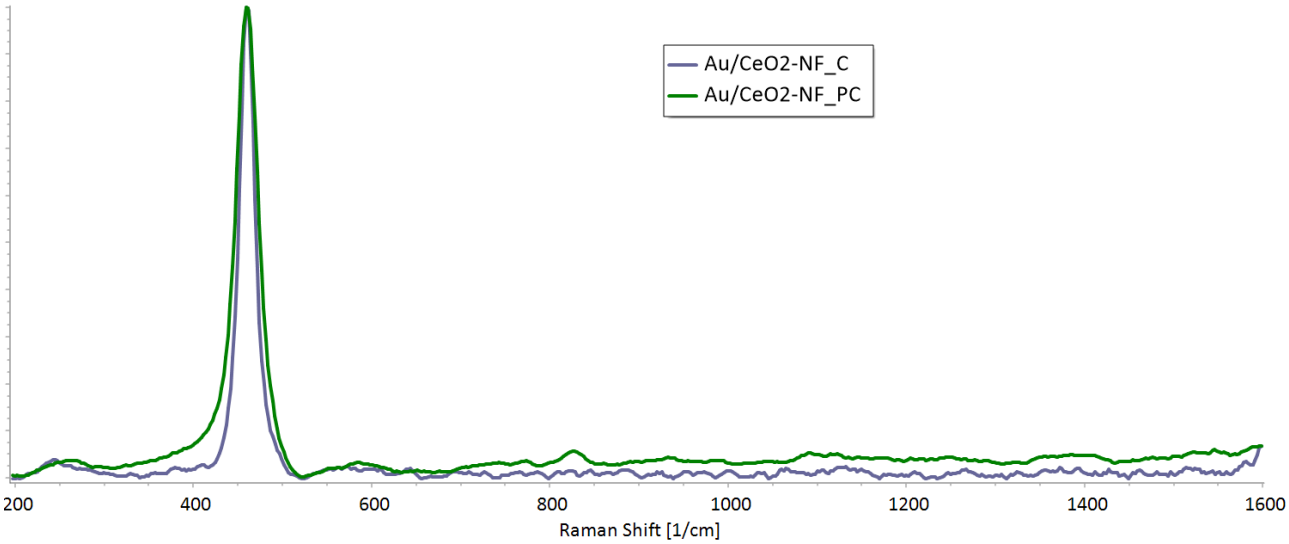

Figure 99: Raman spectra of samples Au/CeO_2-NF_C and Au/CeO_2-NF_PC

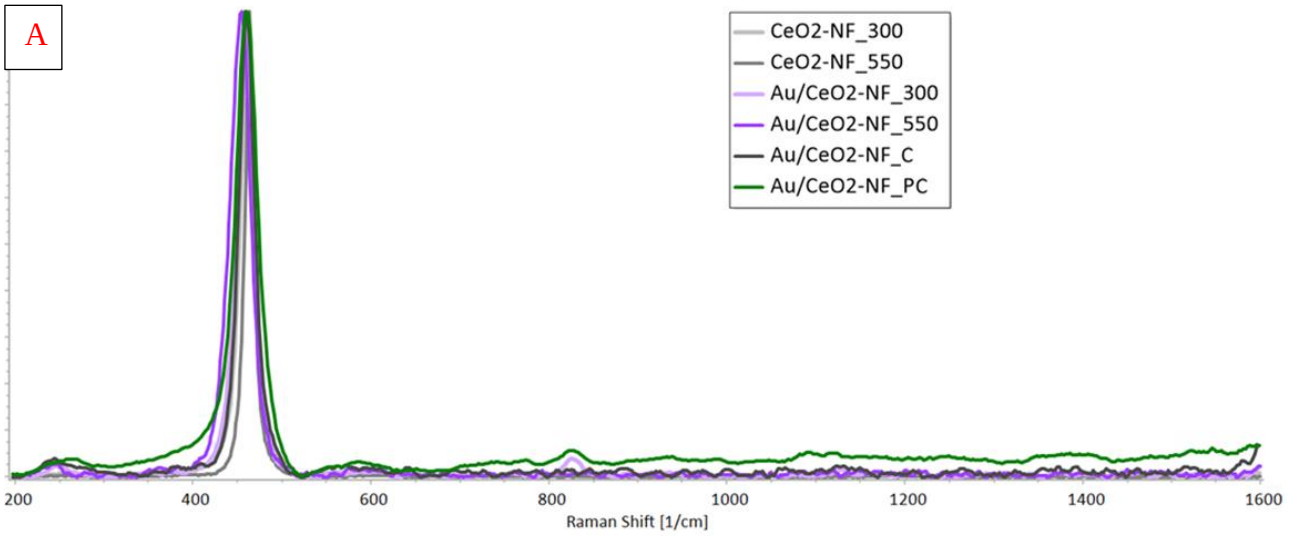
A
CeO2-NF_300
CeO2-NF_550
Au/CeO2-NF_300
Au/CeO2-NF_550
Au/CeO2-NF_C
Au/CeO2-NF_PC
200
400
600
800
1000
1200
1400
1600
Raman Shift [1/cm]

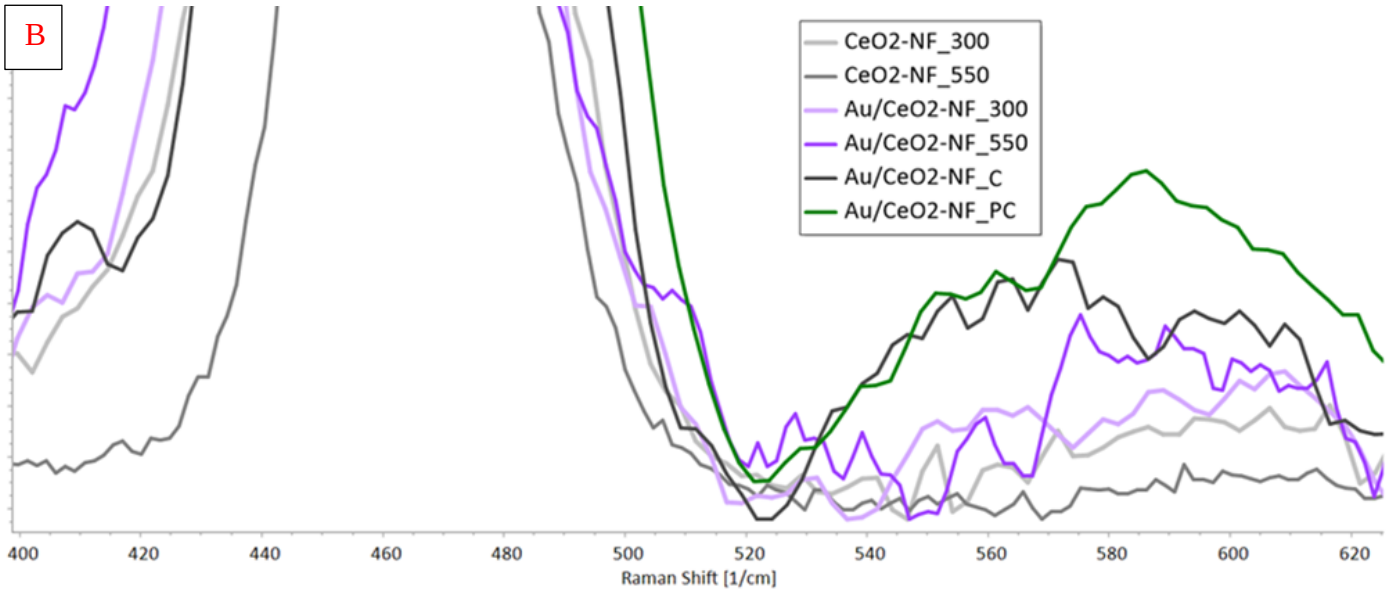
B
CeO2-NF_300
CeO2-NF_550
Au/CeO2-NF_300
Au/CeO2-NF_550
Au/CeO2-NF_C
Au/CeO2-NF_PC
400
420
440
460
480
500
520
540
560
580
600
620
Raman Shift [1/cm]

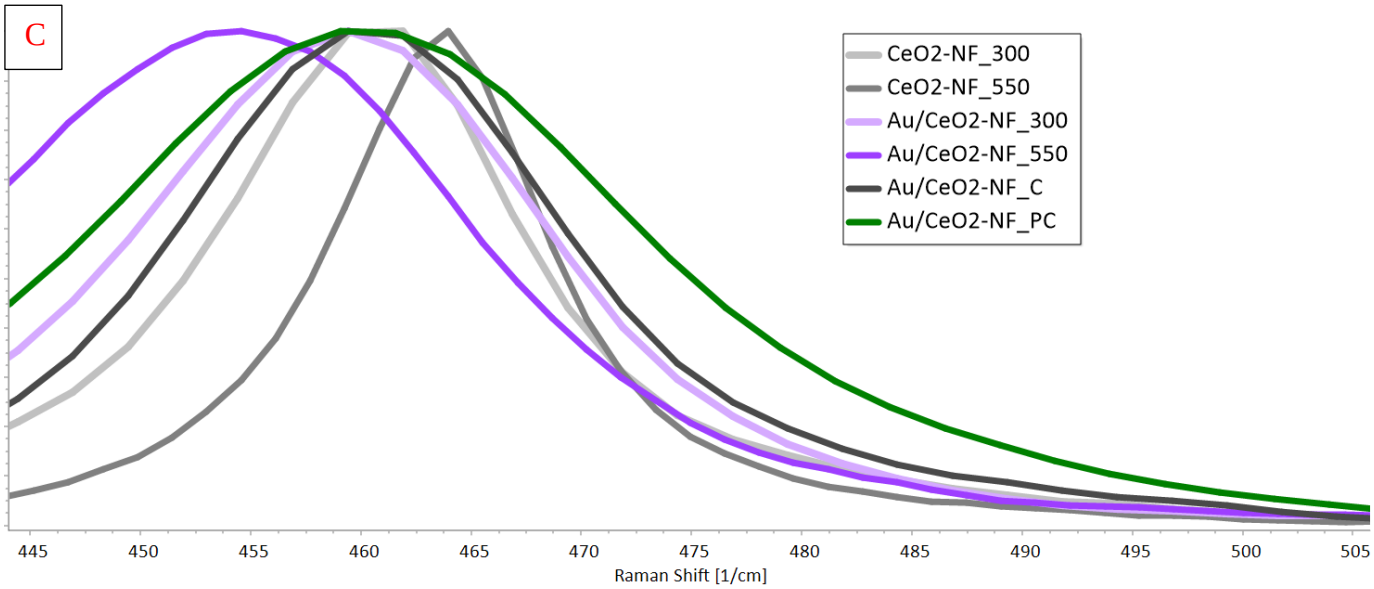

Figure 100: comparison of Raman spectra of the nanofiber samples (A), magnification on the D-band region (B), magnification on the main peak of ceria (C)DRUV-Vis analysis on nanofibers spun with gold

3.3.2.5 DRUV-Vis analysis on nanofibers spun with gold

The spectra of the DRUV-vis analysis on nanofibers samples Au/CeO_2-NF_PC (black and green lines) are reported in Figure 101, alongside sample Au/CeO_2-NF_300 (pink line) for comparison.

The catalyst samples show the band of the plasmonic resonance of gold nanoparticles around 570nm (Figure 102). The sample Au/CeO_2-NF_C (black curve), seems to have a plasmonic band more red-shifted at 588nm and intense, compared with the two catalysts prepared via DP (pink and purple curves) and to the sample Au/CeO_2-NF_PC. This information is in accordance with the XRD data from chapter 3.3.2.3, where Au NP are reported to have a greater average diameter (average diameter from Scherrer: 20nm) in the sample Au/CeO2-NF_C rather than the samples prepared via DP (average diameter for samples Au/CeO_2-NF_300 and _550 of 7nm and 8nm respectively).

The sample Au/CeO_2-NF_PC (green line) presents the maximum of its plasmonic band at 568nm as if the average diameter of its nanoparticles is at an intermediate size between samples Au/CeO_2-NF_300 and Au/CeO_2-NF_550; this data is not in accordance with the XRD where the average diameter of the nanoparticles calculated from Scherrer equation was 24nm. This shift could be caused by some interaction between the metal and the support. [18,19,21,22]

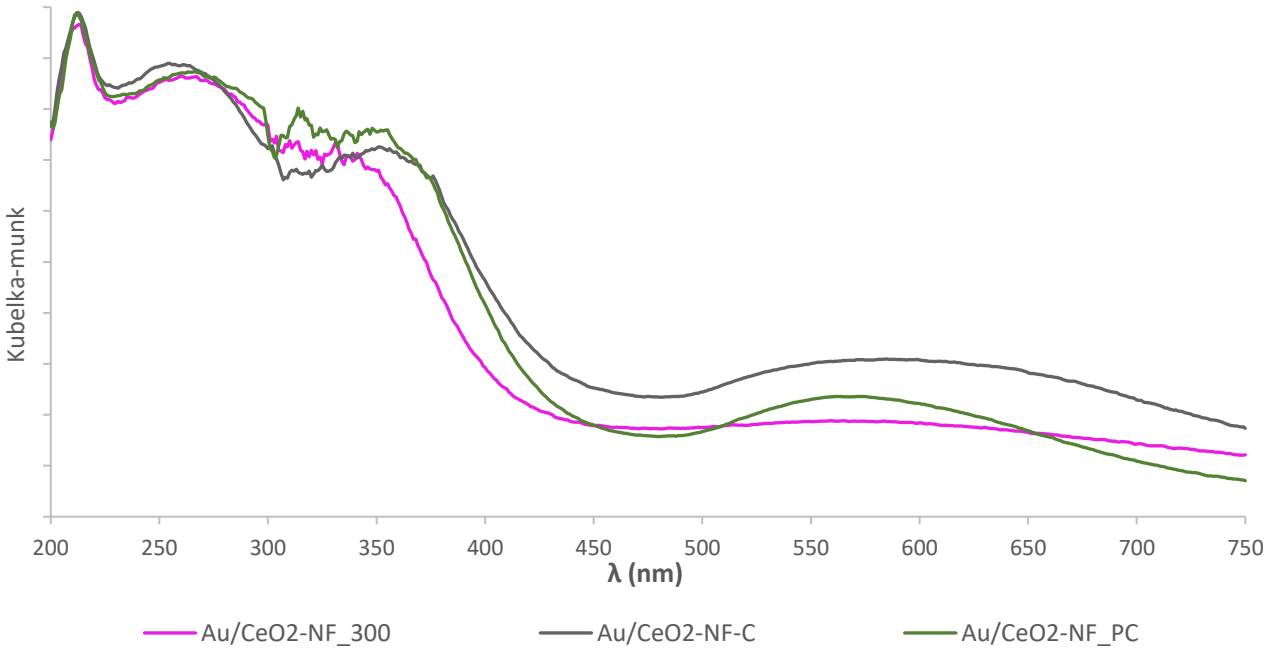

Figure 101: DRUV-Vis on CeO_2-NF samples spun with Au (black and green curve) and, for comparison, sample Au/CeO_2-NF_300 prepared via DP (pink curve)

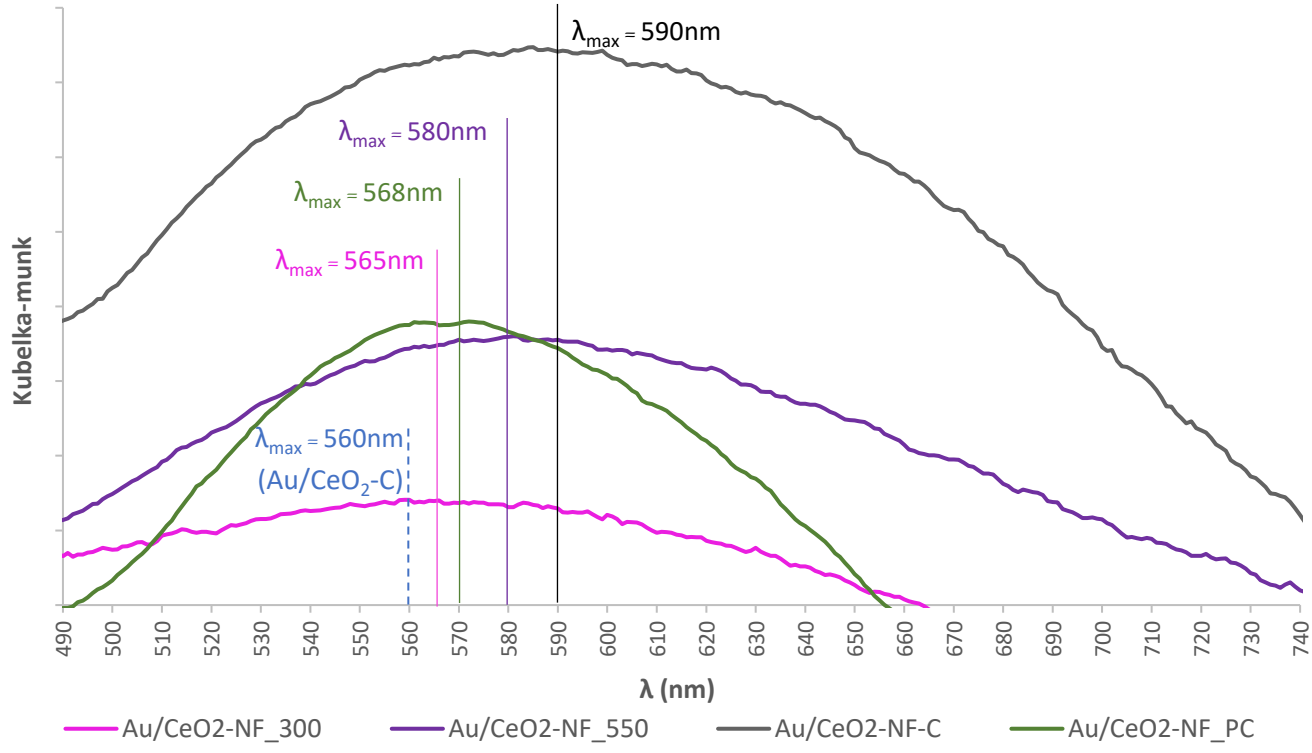

Figure 102: DRUV-Vis spectra of CeO2-NF samples between 370nm and 740nm

Comparing the relative intensity of the spectra for all the samples in nanofibers between 235nm and 260nm (Figure 103) is not possible to clearly notice the different amount of Ce^{3+} and Ce^{4+} in the samples.

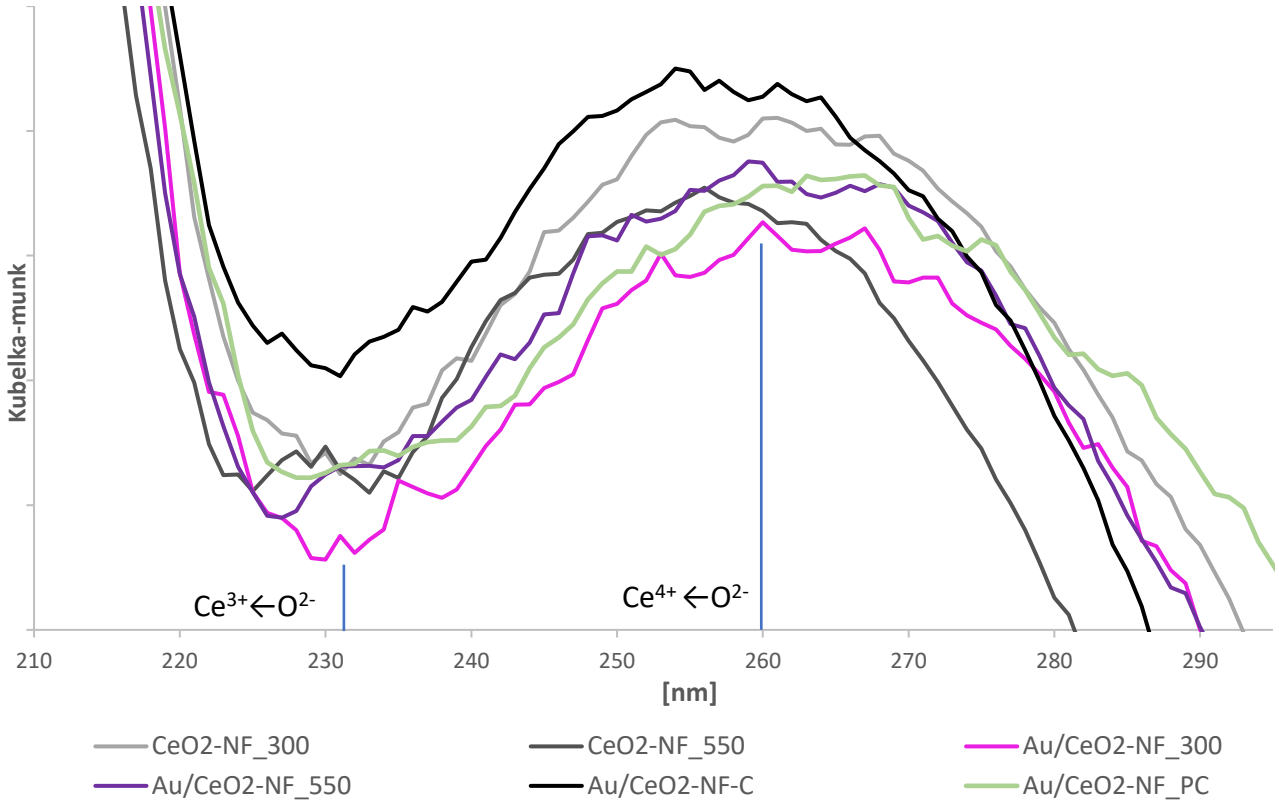

Figure 103: DRUV-Vis spectra of CeO_2-Nanofibers samples between 210nm and 290nm

3.3.2.6 Catalytic tests on nanofibers spun with gold

The results for the catalytic test for the gold catalyst supported on ceria nanofibers spun with $HAuCl_4$ are reported over time in the following Figure 104 and Table 18 for the tests performed at 70°C, and in Table 19 for the tests performed at 80°C.

The presence of the catalysts leads to complete conversion of HMF, as for the other catalysts supported on commercial cerium oxide (chapters 3.1.4 and 3.2.4), but the sample Au/CeO_2-NF_C seem not particularly selective for the reaction of oxidation of the HMF and shows almost negligible yield in FDCA and high carbon loss over 60% after 2 and 4 hours of reaction time. Considering the extremely low activity of the catalyst the reaction at 1 hour of reaction time have not been tested with this catalyst at the temperature of 70°C.

Catalyst	time (h)	X HMF (%)	Y HMFCA (%)	Y FFCA (%)	Y FDCA (%)	Carbon Loss (%)	Note:
blank	4	94	28	6	4	**57**	Neither support nor catalyst
blank	4	Not injectable due to side products					Blank, only CeO_2 - NF_300°C
blank	4	Not injectable due to side products					Blank, only CeO_2 - NF_550°C
Au/CeO_2 - NF_300	1	100	77	3	4	16	
	2	100	67	2	28	3	
	4	100	47	0	53	0	
Au/CeO_2 - NF_550	1	100	68	0	4	27	
	2	100	77	5	13	5	
	4	98	70	4	21	3	
Au/CeO_2 -C	2	100	7	0	1	92	
	4	100	39	0	>1	60	

Table 18: Catalytic test results over time of the Au/ CeO2 -NF catalyst, T= 70 °C

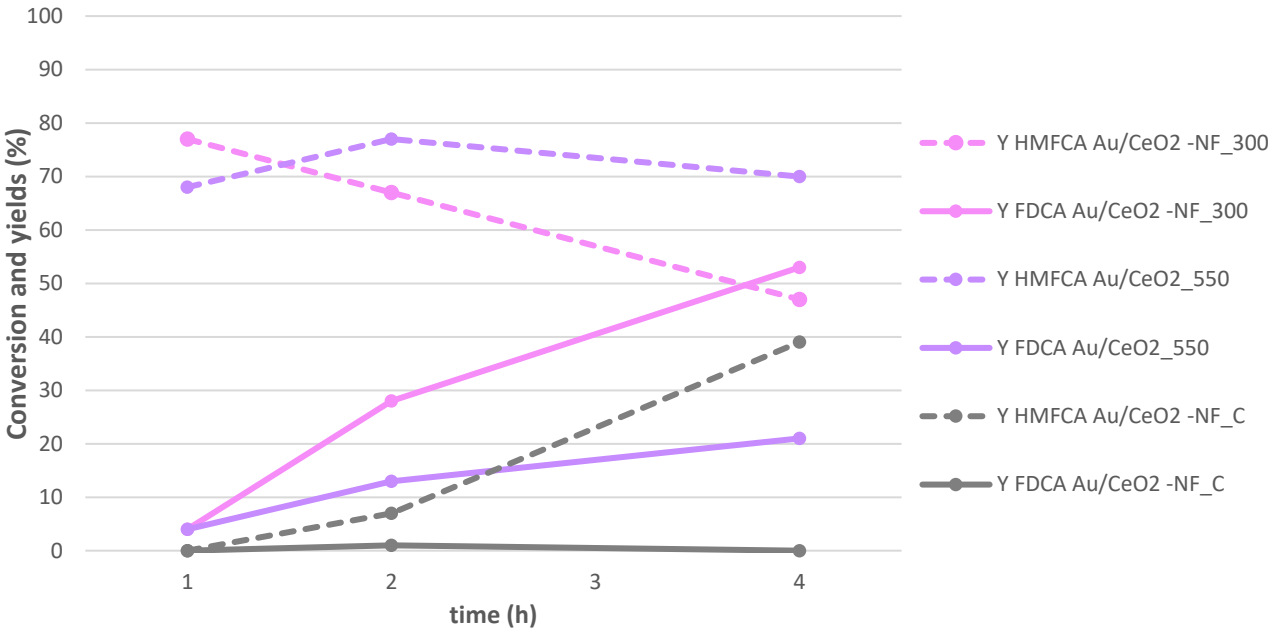

Figure 104: Conversion and products yields as a function of time for the Au/CeO2 -NF catalyst, T=70 °C

The catalytic performance for the same reaction performed at 80°C (Table 19) resemble the same pattern recorded at 70°C, but higher yield and better selectivity in the desired product are obtained with all the catalysts. At 80°C and 4 hours of reaction time have been tested also the sample Au/CeO_2 -NF_PC, it was not possible to do other tests for reasons of time.

The reaction with the sample Au/CeO_2 -NF_C proceeds slightly better over HMFCA, and its yields are, marginally higher compared to the yields obtained at 70°C. The carbon loss is increased to 34% after 4h with the increasing temperature. Despite these findings, the samples prepared via DP are more active and selective for the desired reaction.

The sample Au/CeO_2 -NF_PC had a similar performance to the sample Au/CeO_2 -NF_C in the same conditions. They have been compared at 80°C and 4 hours of reaction time (Table 19 and Figure 106) as is possible to notice both of the catalysts caused the complete conversion of the HMF and had low and comparable yield in the desired oxidation products, the main difference is that the sample Au/CeO_2 -NF_PC had a carbon loss greater than 10% of sample Au/CeO_2 -NF_C.

Catalyst	time (h)	X HMF (%)	Y HMFCA (%)	Y FFCA (%)	Y FDCA (%)	Carbon Loss (%)
Au/CeO_2 -NF_300	1	100	61	4	25	10
	2	100	42	2	54	2
	4	100	44	1	55	0
Au/CeO_2 -NF_550	1	98	51	6	3	40
	2	100	68	1	17	14
	4	100	59	3	24	13
Au/CeO_2 -NF_C	1	93	43	8	2	43
	2	96	28	7	2	63
	4	100	53	9	4	34
Au/CeO_2 -NF_PC	4	100	42	8	4	47

Table 19: Catalytic test results over time of the Au/ CeO2 -NF catalyst, T= 80 °

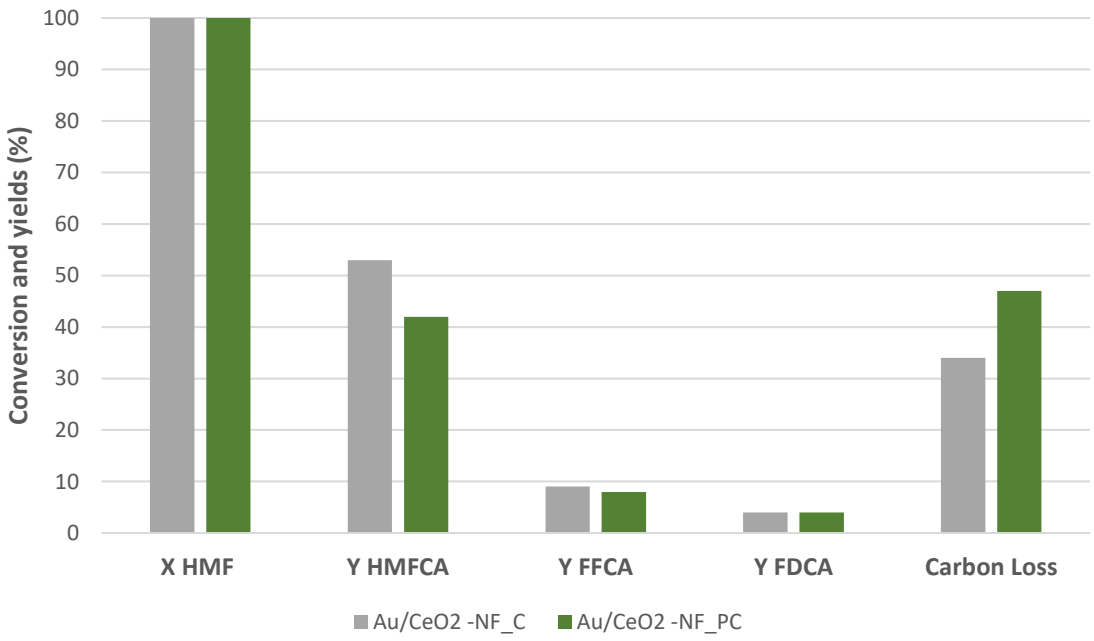

Figure 105: comparison of the catalytic test of the samples, reaction conditions: 4h, 80°C

3.4 Comparison of the different samples

3.4.1 *Comparison of the Raman analysis on the different samples*

The spectra of the catalysts synthesized are shown in Figure 106 while peaks parameters are reported in Table 20. All the spectra present a shift of the main F_2g peak to minor Raman shift than the respective supports without gold and the pure peak ceria (previously explained in chapters 3.1.2, 3.2.2 and 3.3.1.5)[14,24,28], this phenomenon is due to the presence of gold on the support and the size of the crystals[14,32]. Smaller crystals can produce a peak broadening and both smaller crystals and the presence of gold can produce a redshift of the peak to lower Raman shift. In this case, the crystallites dimension have been calculated through Scherrer's equation and reported previously (paragraphs: 3.1.1, 3.2.2 and 3.3.1.4), the sample with the smallest crystallites size is the sample Au/CeO_2-HS, but the samples in nanofibers are redshifted too, in particular the sample Au/CeO_2-NF_550°C is redshifted as the sample Au/CeO_2-HS and almost broad as it. Has been reported by Loridant et al.[32] that nanostructure with a high aspect ratio presents a broader and redshifted main band.

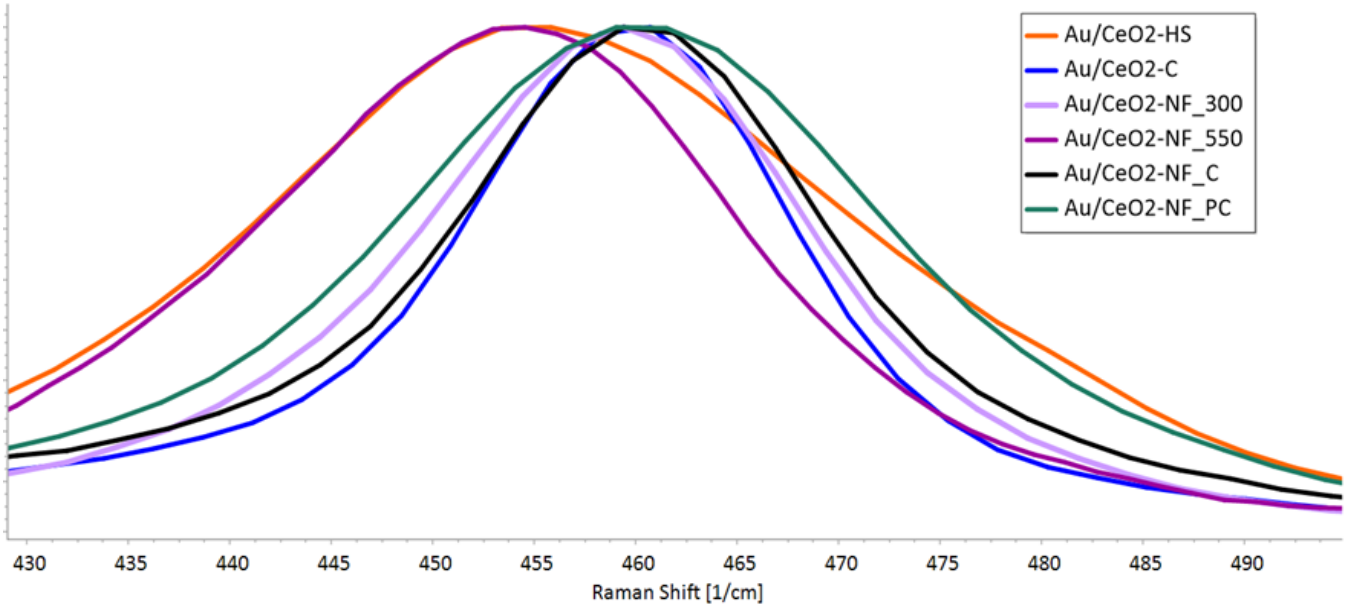

Figure 106: Comparison of the Raman spectra of the catalysts synthesised

Sample	Centre [cm^{-1}]	FWMH	Dimension of crystallites [nm]
Au/CeO_2-HS	454.8	36.8	5
Au/CeO_2-NF_550	454.1	28.8	12
Au/ CeO_2-NF_PC	460.4	24.2	4
Au/CeO_2-NF_300	459.4	23.1	8
Au/ CeO_2-NF_C	460.5	22.2	7
Au/ CeO_2-C	459.0	19.7	18

Table 20: peaks parameters

3.4.2 *Comparison between the results of the catalytic test of the different samples*

The catalytic test results at 70°C and 80°C of the catalysts supported on commercial ceria powder have been compared in the following Table 21 and Figure 107. The sample Au/CeO_2-C seem to be more selective and active for the oxidation of HMF than the other catalysts. The activity of the catalyst strongly increases with the temperature and reaches the 96% yield in FDCA and negligible carbon loss in 4 hours at 80°C. On the other hand, the catalyst Au/CeO_2-HS gives lower yields in the desired product and carbon losses. The carbon loss over time seems to get worst with the increasing temperature.

The catalyst Au/CeO_2-HS has smaller gold nanoparticles and a high surface area given by the small ceria crystallites. A possible explanation for the low performance of the sample Au/CeO_2-HS could be diffusion problems of the reagents and the products in the pores of the catalysts, which are probably narrow because of the small crystallites of the support. A further porosimeter analysis could provide more information.

Catalyst	**T (°C)**	**Reaction time (h)**	**Y HMFCA (%)**	**Y FFCA (%)**	**Y FDCA (%)**	**Carbon Loss (%)**
blank	70	4	28	6	4	**57**
Au/CeO_2-C	70	1	68	2	20	10
		2	59	0	41	0
		4	32	1	67	0
Au/CeO2-HS	70	1	79	8	5	8
		2	75	6	13	6
		4	64	2	16	18
Au/CeO_2-C	80	1	70	2	18	10
		2	35	0	65	0
		4	3	0	96	1
Au/CeO2-HS	80	1	Not injectable due to heavy products			
		2	Not injectable due to heavy products			
		4	55	3	33	9

Table 21: Comparison of the performance of the catalyst for the reactions at 70°C

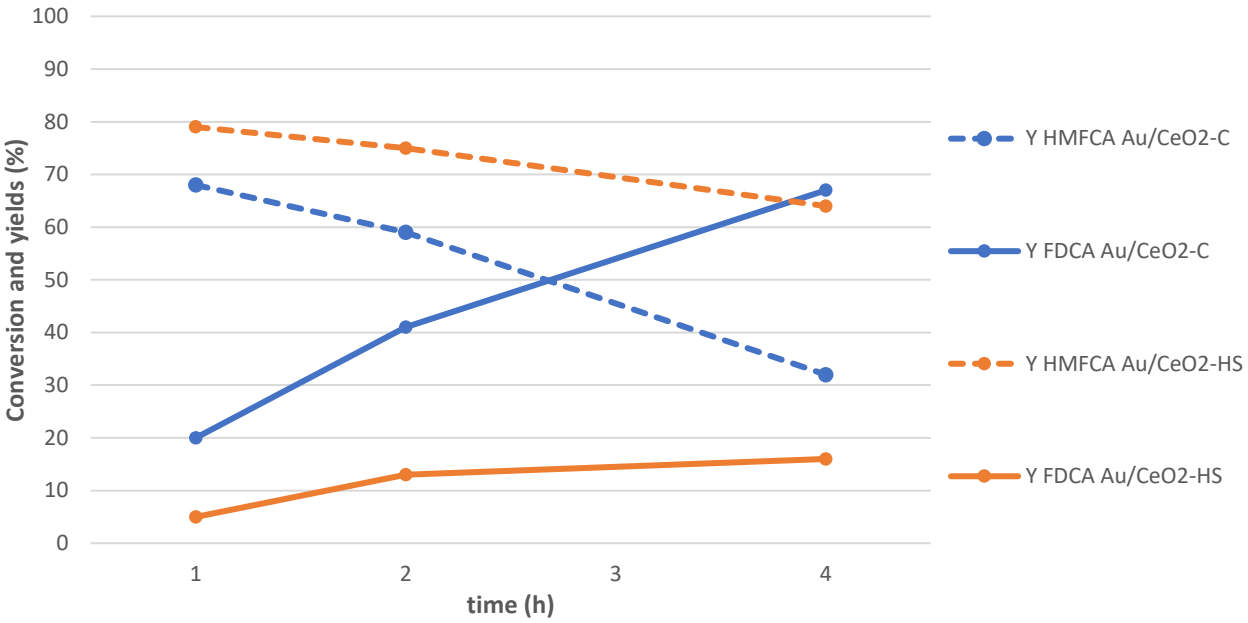

Figure 107: Comparison of conversion and products yields of the commercial catalysts over time, T=70 °C

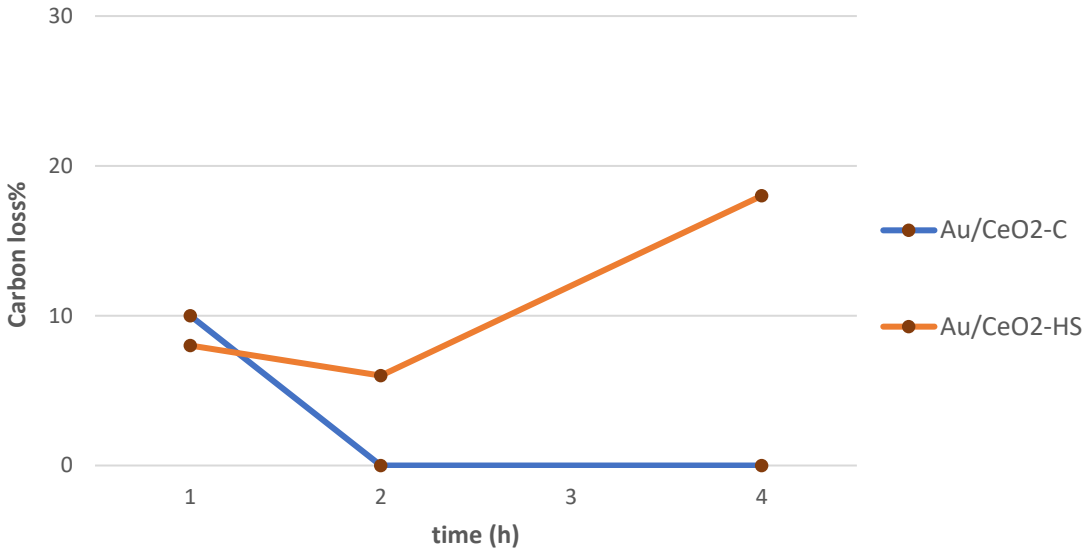

Figure 108: Carbon loss at 70°C, comparison over time of the commercial catalysts

The samples Au/CeO_2-C and Au/CeO_2-NF_300 are the catalysts supported on commercial ceria and spun nanofibers that give the best results in the oxidation of the HMF respectively. Both catalysts are selective for the oxidation of HMF, which is confirmed by the low carbon loss which became almost null after two or more hours of reaction time. The yields in the intermediate products, HMFCA and FFCA, decrease over time, while the yield in FDCA

increases with it. In particular, the Au/CeO_2-C catalyst is more active than the sample in nanofibers, after four hours of reaction at 80°C it reached the 96% yield in FDCA, while the other catalyst, in the same conditions, managed to produce the 60%.

Catalyst	**T (°C)**	**Reaction time (h)**	**Y HMFCA (%)**	**Y FFCA (%)**	**Y FDCA (%)**	**Carbon Loss (%)**
blank	70	4	28	6	4	**57**
Au/CeO_2-C	70	1	68	2	20	10
		2	59	0	41	0
		4	32	1	67	0
Au/CeO_2 - NF_300	70	1	77	3	4	16
		2	67	2	28	3
		4	47	0	53	0
Au/CeO_2-C	80	1	70	2	18	10
		2	35	0	65	0
		4	3	0	96	1
Au/CeO_2 - NF_300	80	1	61	4	25	10
		2	42	2	54	2
		4	44	1	55	0

Table 22: Comparison of the performance of the catalysts Au/CeO_2-C and Au/CeO_2 -NF_300

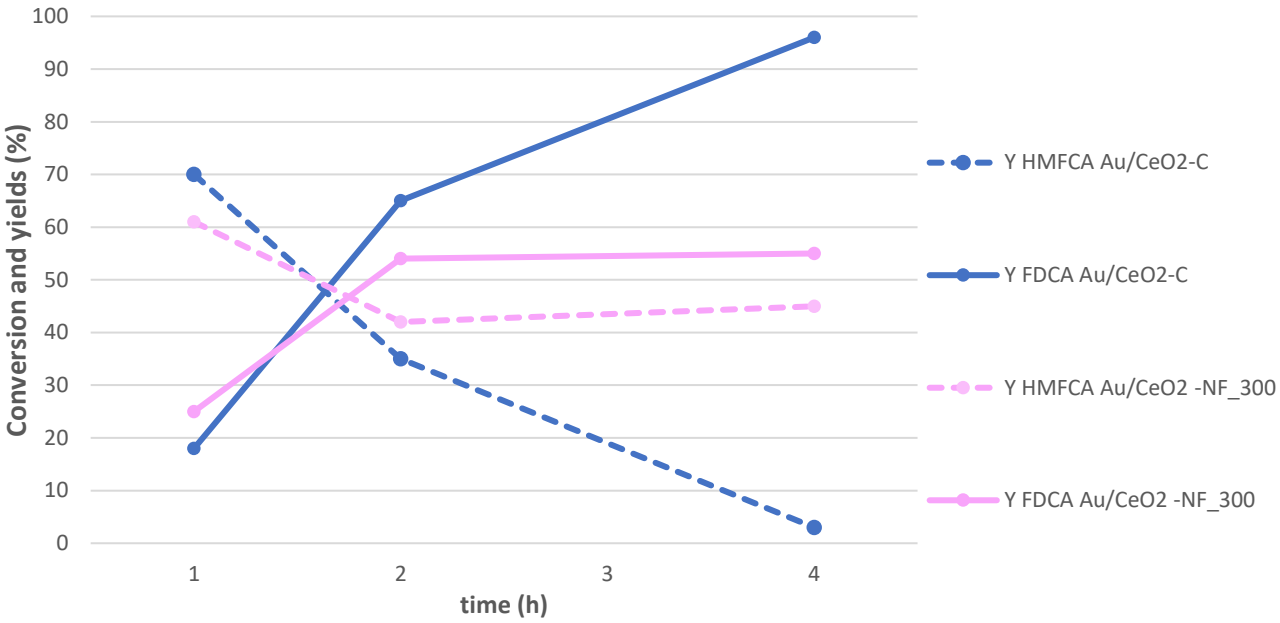

Figure 109: Comparison of conversion and products yields of the catalysts Au/CeO_2-C and Au/CeO_2 -NF_300 over time, T=80 °C

3.5 References

1. Gibbons, W. T., Liu, T. H., Gaskell, K. J. & Jackson, G. S. Characterization of palladium/copper/ceria electrospun fibers for water–gas shift catalysis. *Applied Catalysis B: Environmental* **160–161**, 465–479 (2014).

2. Lucarelli, C. *et al.* Efficient and ecofriendly route for the solvent-free synthesis of piperonal and aromatic aldehydes using Au/CeO2 catalyst. *Applied Catalysis B: Environmental* **203**, 314–323 (2017).

3. Gritschneder, S. & Reichling, M. Structural elements of CeO2(111) surfaces. *Nanotechnology* **18**, 044024 (2006).

4. Polychronopoulou, K. & Jaoudé, M. A. Nano-architectural advancement of CeO2-driven catalysis via electrospinning. *Surface and Coatings Technology* **350**, 245–280 (2018).

5. Zhang, D., Du, X., Shi, L. & Gao, R. Shape-controlled synthesis and catalytic application of ceria nanomaterials. *Dalton Transactions* **41**, 14455–14475 (2012).

6. Sol-immobilized vs deposited-precipitated Au nanoparticles supported on CeO2 for furfural oxidative esterification.pdf.

7. Chemistry of the Elements - 2nd Edition. https://www.elsevier.com/books/chemistry-of-the-elements/greenwood/978-0-7506-3365-9.

8. Hameed, S., Lin, L., Wang, A. & Luo, W. Recent Developments in Metal-Based Catalysts for the Catalytic Aerobic Oxidation of 5-Hydroxymethyl-Furfural to 2,5-Furandicarboxylic Acid. *Catalysts* **10**, 120 (2020).

9. Study of high pressure structural stability of CeO2 nanoparticles - IOPscience. https://iopscience.iop.org/article/10.1088/1674-1137/37/9/098003/meta?casa_token=MNh_ve93gCcAAAAA:ex9vo8e5mURD5IiiyaFW7z3U13H498mtbzOLiSPvaWxhBIl9qU9Ib2EVH2rdyDUwrsnhkVQz6Ng.

10. Lolli, A. *et al.* Hard-template preparation of Au/CeO2 mesostructured catalysts and their activity for the selective oxidation of 5-hydroxymethylfurfural to 2,5-furandicarboxylic acid. *Microporous and Mesoporous Materials* **226**, 466–475 (2016).

11. Centeno, M., Paulis, M., Montes, M. & Odriozola, J. Catalytic combustion of volatile organic compounds on Au/CeO2/Al2O3 and Au/Al2O3 catalysts. *Applied Catalysis A: General* **234**, 65–78 (2002).

12. Zhang, W., Niu, X., Chen, L., Yuan, F. & Zhu, Y. Soot Combustion over Nanostructured Ceria with Different Morphologies. *Scientific Reports* **6**, 29062 (2016).

13. Jing, G. *et al.* Comparison of Au–Ce and Au–Cu interaction over Au/CeO $_2$ –CuO catalysts for preferential CO oxidation. *CrystEngComm* **21**, 363–371 (2019).

14. Wu, Z., Li, M., Howe, J., Meyer, H. M. & Overbury, S. H. Probing Defect Sites on CeO2 Nanocrystals with Well-Defined Surface Planes by Raman Spectroscopy and O2 Adsorption. *Langmuir* **26**, 16595–16606 (2010).

15. Anandkumar, M., Ramamurthy, C. H., Thirunavukkarasu, C. & Babu, K. S. Influence of age on the free-radical scavenging ability of CeO2 and Au/CeO2 nanoparticles. *J Mater Sci* **50**, 2522–2531 (2015).

16. Taniguchi, T. *et al.* Identifying Defects in Ceria-Based Nanocrystals by UV Resonance Raman Spectroscopy. *J. Phys. Chem. C* **113**, 19789–19793 (2009).

17. Li, S. *et al.* Catalytic Performance of Gold Supported on Mn, Fe and Ni Doped Ceria in the Preferential Oxidation of CO in H2-Rich Stream. *Catalysts* **8**, 469 (2018).

18. Size controlled and bio-directed synthesis of ceria nanopowders and their in vitro cytotoxicity.pdf.

19. Bharali, P., Saikia, P. & Reddy, B. M. Large-scale synthesis of ceria-based nano-oxides with high CO oxidation activity. *Catal. Sci. Technol.* **2**, 931–933 (2012).

20. The catalysts of three-dimensionally ordered macroporous Ce1-xZrxO2 supported gold nanoparticles for soot combustion The metal–support interaction.pdf.

21. Ceria on silica and alumina catalysts dispersion and surface acid-base properties as probed by X-ray diffractometry UV-Vis diffuse reflectance and diffuse reflectance and in situ IR absorption stud.pdf.

22. Ait Rass, H., Essayem, N. & Besson, M. Selective aqueous phase oxidation of 5-hydroxymethylfurfural to 2,5-furandicarboxylic acid over Pt/C catalysts: influence of the base and effect of bismuth promotion. *Green Chem.* **15**, 2240 (2013).

23. Casanova, O., Iborra, S. & Corma, A. Biomass into chemicals: aerobic oxidation of 5-hydroxymethyl-2-furfural into 2,5-furandicarboxylic acid with gold nanoparticle catalysts. *ChemSusChem* **2**, 1138–1144 (2009).

24. Schilling, C., Hofmann, A., Hess, C. & Ganduglia-Pirovano, M. V. Raman Spectra of Polycrystalline CeO $_2$: A Density Functional Theory Study. *J. Phys. Chem. C* **121**, 20834–20849 (2017).

25. Wu, Z., Li, M. & Overbury, S. On the structure dependence of CO oxidation over CeO 2 nanocrystals with well-defined surface planes. *Journal of Catalysis - J CATAL* **285**, 61–73 (2012).

26. Kumar, S. & Ojha, A. K. Ni, Co and Ni–Co codoping induced modification in shape, optical band gap and enhanced photocatalytic activity of CeO2 nanostructures for photodegradation of methylene blue dye under visible light irradiation. *RSC Adv.* **6**, 8651–8660 (2016).

27. Guzman, J., Carrettin, S. & Corma, A. Spectroscopic Evidence for the Supply of Reactive Oxygen during CO Oxidation Catalyzed by Gold Supported on Nanocrystalline CeO $_2$. *J. Am. Chem. Soc.* **127**, 3286–3287 (2005).

28. Lohrenscheit, M. & Hess, C. Direct Evidence for the Participation of Oxygen Vacancies in the Oxidation of Carbon Monoxide over Ceria-Supported Gold Catalysts by using Operando Raman Spectroscopy. *ChemCatChem* **8**, 523–526 (2016).

29. Liu, Y., Chen, H.-S., Li, J. & Yang, P. Morphology adjustment of one dimensional CeO2 nanostructures via calcination and their composite with Au nanoparticles towards enhanced catalysis. *RSC Adv.* **5**, 37585–37591 (2015).

30. Zhang, Z. *et al.* Synthesis of monodisperse silver nanoparticles for ink-jet printed flexible electronics. *Nanotechnology* **22**, 425601 (2011).

31. Phoka, S. *et al.* Synthesis, structural and optical properties of CeO2 nanoparticles synthesized by a simple polyvinyl pyrrolidone (PVP) solution route. *Materials Chemistry and Physics* **115**, 423–428 (2009).

32. Loridant, S. Raman spectroscopy as a powerful tool to characterize ceria-based catalysts. *Catalysis Today* S0920586120301668 (2020) doi:10.1016/j.cattod.2020.03.044.

33. Alahmad, A., Eleoui, M., Falah, A. & Alghoraibi, I. Preparation of colloidal silver nanoparticles and structural characterization. *Physical Sciences Research International* **1**, 89–96 (2013).

4 Conclusions

It is known that ceria could be used as support or catalyst itself, its properties are related to the number of defects on the surface, which depend on the surface area, the morphology and the reticular planes exposed in the material. In this work, we have prepared 1D structures of cerium(IV) oxide through electrospinning with the purpose of synthesising gold on ceria catalyst to study the effect of the preparation method on the final morphologies and the catalytic properties of the material.

Electrospinning was used to spin both the precursor structures for the supports and the catalysts themselves. The spun precursors of the support have been calcined at different temperatures (300°C and 550°C) in air atmosphere to eliminate the polymeric templating agent (PVP) and obtain pure CeO_2 nanofibers. Then, gold nanoparticles were loaded by deposition precipitation (DP) on the surface of the prepared cerium oxide.

Two more catalysts have been prepared by mixing directly in the spinning solution the precursor of the gold nanoparticles ($HAuCl_4$) to obtain them during the following heat treatments. In this case, the main problem to solve was to succeed in the elimination of PVP, because the exothermic reaction could lead to the undesired growing of the metal species. One sample has been prepared via direct calcination of the fibres in a muffle; the other one has been first heated under N_2 flow and then calcined in air.

These samples have been characterized through SEM, TEM, TGA, XRD, ATR, RAMAN and DRUV-Vis analyses and have been tested on the selective oxidation of HMF to FDCA.

A scheme of the different preparation has been reported in Figure 110, two SEM images of the morphology obtained after spinning are shown in Figure 111:

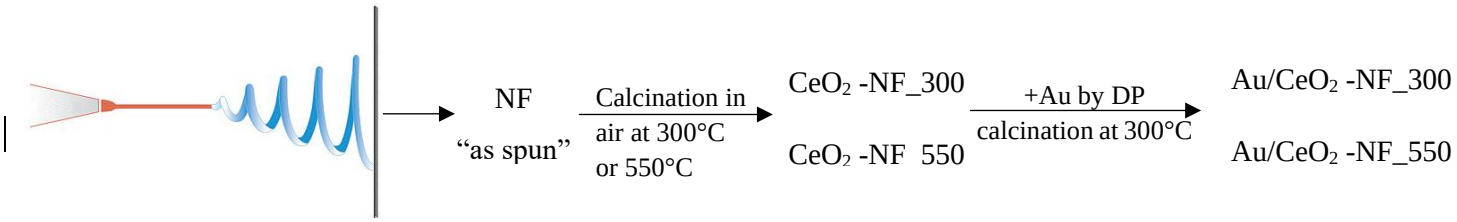

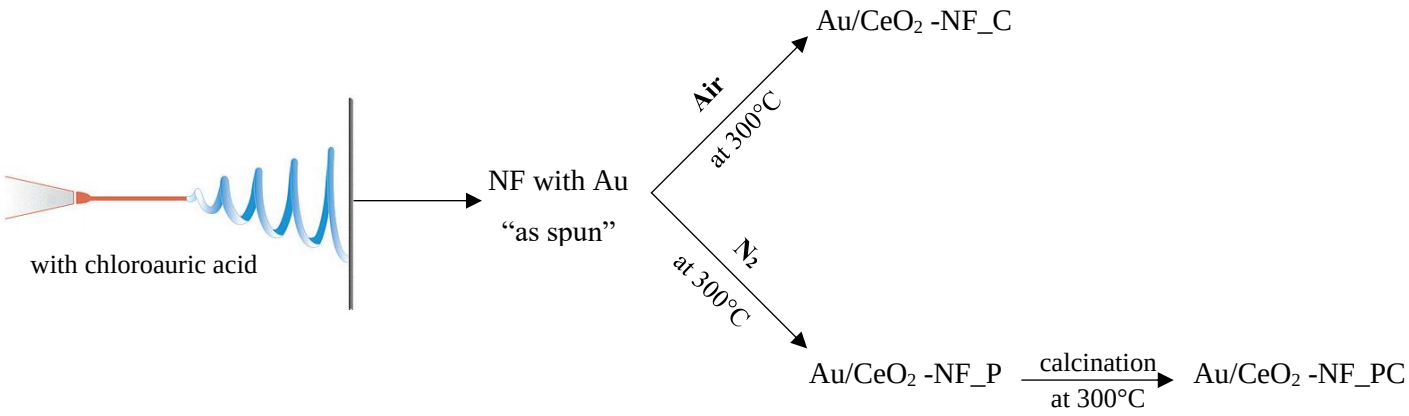

Figure 110: Resume of the preparations of the catalysts

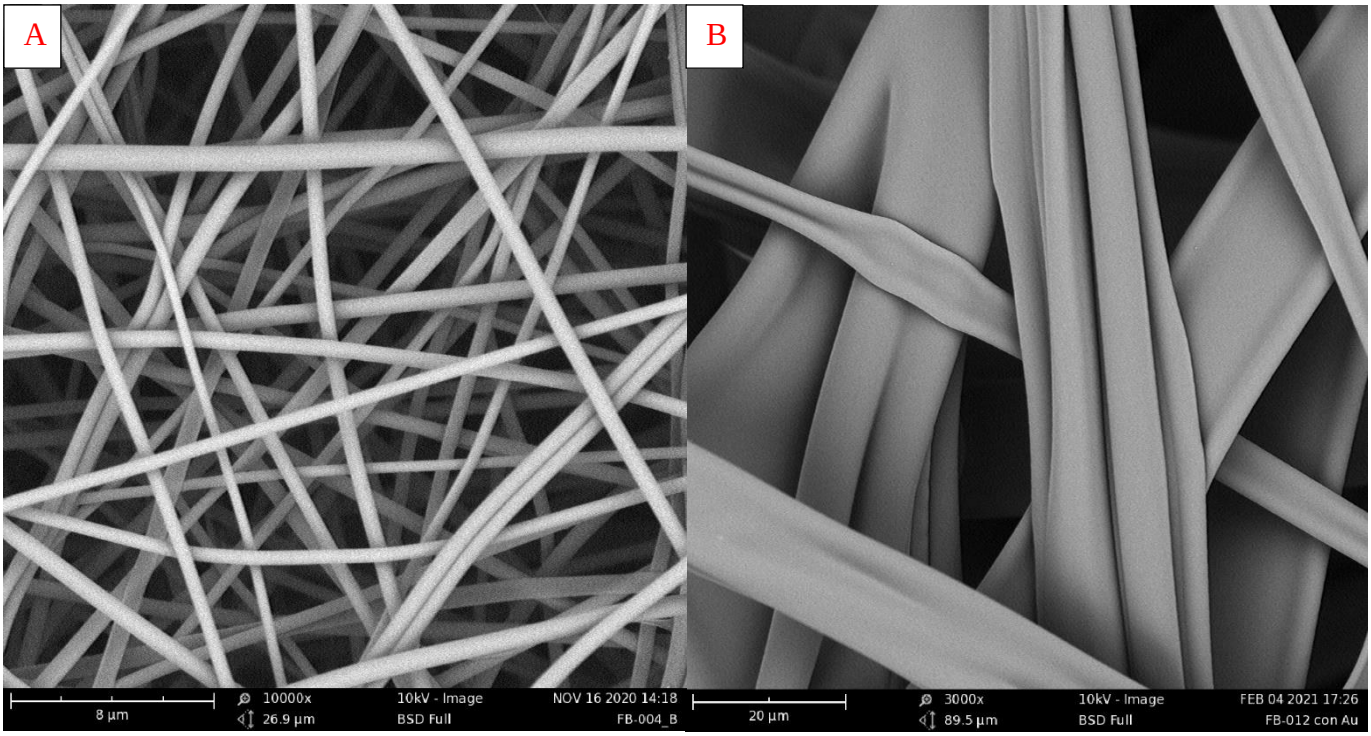

Figure 111: SEM images of nanofibers morphology of the sample NF "as-spun" without gold (A), and SEM images of the nanofibers belt-like of the sample NF with Au "as-spun" (B)

In Table 23 is possible to notice the strong influence of the calcination temperature on the surface area of the spun supports, the samples CeO_2 -NF_300 and CeO_2 -NF_550 have been calcined at 300°C and 550°C respectively and they show a significant difference in the surface area of 83 m^2/g and 21 m^2/g.

No significant differences have been detected between the surface area of the samples of calcined nanofibers without gold at 300°C (CeO_2 -NF_300°C and Au/CeO_2-NF_300°C) and the sample of nanofibers spun with gold and then calcined (Au/CeO_2NF_C). On the other end, there is a remarkable gap between those samples and the sample prepared via two heat treatments (Au/CeO_2NF_PC) one in N_2 flow and the other in a muffle.

Support	**Sample**	**Surface area [m^2/g]**	**Notes:**
Electrospun nanofibers	CeO_2 -NF_300	83	Ceria nanofiber support, calcined at 300°C
	CeO_2 -NF_550	21	Ceria nanofiber support, calcined at 550°C
	Au/CeO_2-NF_300	77	Au supported on nanofiber support calcined at 300°C, synthesised via DP
	Au/CeO_2-NF_550	29	Au supported on nanofiber support calcined at 550°C, synthesised via DP
Electrospun nanofibers (spun with chloroauric acid)	Au/CeO_2 -NF_C	76	Prepared by electrospinning using a solution containing HAuCl4 and calcinating the fibres at 300°C in air
	Au/CeO_2-NF_P	N/A	Prepared by electrospinning using a solution containing $HAuCl_4$ followed by thermal treatment at 300°C in N_2
	Au/CeO_2-NF_PC	96	Prepared by electrospinning using a solution containing $HAuCl_4$ followed by thermal treatment at 300°C in N_2 and calcination in air at 300°C

Table 23: sample prepared and respective surface areas

The Scherrer equation has been used on the XRD analysis of the sample to calculate the average dimension of the crystallites. The effect of the preparation method clearly influenced the dimension of the final ceria crystallites, and the dimension of the crystallites are related to the surface area of the samples (Table 24). The prepared samples showed a small dimension of the crystallites, the main difference could be observed between the samples of supports in NF

calcined at different temperatures and the respective catalyst prepared by DP. The support calcined at higher temperature shows bigger crystallites due to the Ostwald ripening. The two-steps removal of PVP to prepare the sample Au/CeO_2-NF _PC managed to form small crystallites of 4 nm, which gave the highest surface area of the synthesized samples.

Sample	Average dimension of the ceria crystallites (nm)	Surface area (m^2/g)
CeO_2-NF_300	7	83
CeO_2-NF _550	12	21
Au/CeO_2-NF_300	8	77
Au/CeO_2-NF _550	12	29
Au/CeO_2-NF _C	7	76
Au/CeO_2-NF _P	4	N/A
Au/CeO_2-NF _PC	4	96

Table 24: Average dimension of the ceria crystallites and BET surface areas of the samples

The preferential exposure of the reticular plane has been verified using a tabulated reference (reference code: 00-043-1002), no remarkable differences have been highlighted, except for a slight under-exposure of the reticular planes, probably due to a little over-exposure of the face (111) used as reference (Figure 112).

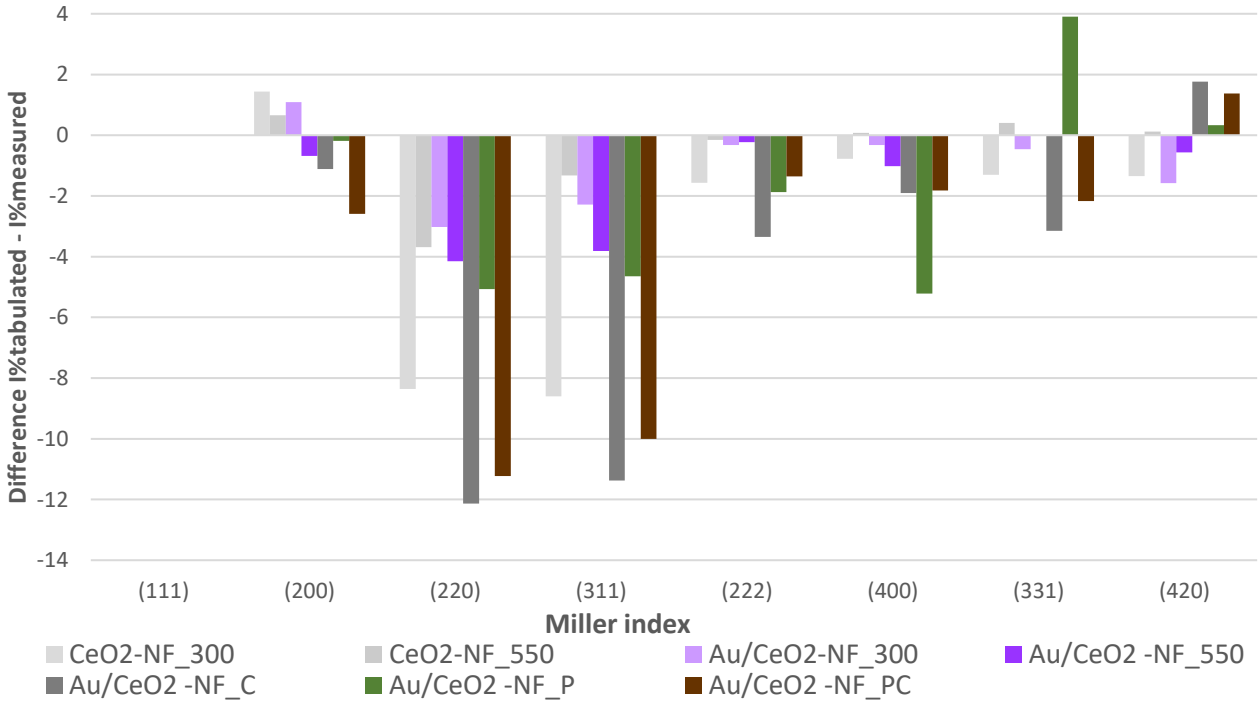

Figure 112: Differences between intensities tabulated and measured for samples CeO2-NF spun without chloroauric acid (tabulated intensities reference code: 00-043-1002)

One of the main goals of the preparation was to form nanoparticles as small as possible. The XRD of the peaks (111) of gold supported ion the prepared catalysts in nanofibers are reported in Figure 113 while the average dimension of the gold crystallites have been calculated through the Scherrer equation and are reported in Table 25. As is possible to notice the preparation method influenced the size of the gold nanoparticles on the catalysts. The catalyst prepared via DP process showed small nanoparticles that do not exceed 8nm. The samples prepared via one or two heat treatments on the fibres spun with $HAuCl_4$ present larger nanoparticles of 20 and 24nm. This has been caused by the strong exothermic degradation of PVP in the nanofibers during heat treatment. Despite the TGA analysis of the samples to better understand the phenomenon and the slow heating rate used during the heat treatments to prevent excessive growth of the metal phase.

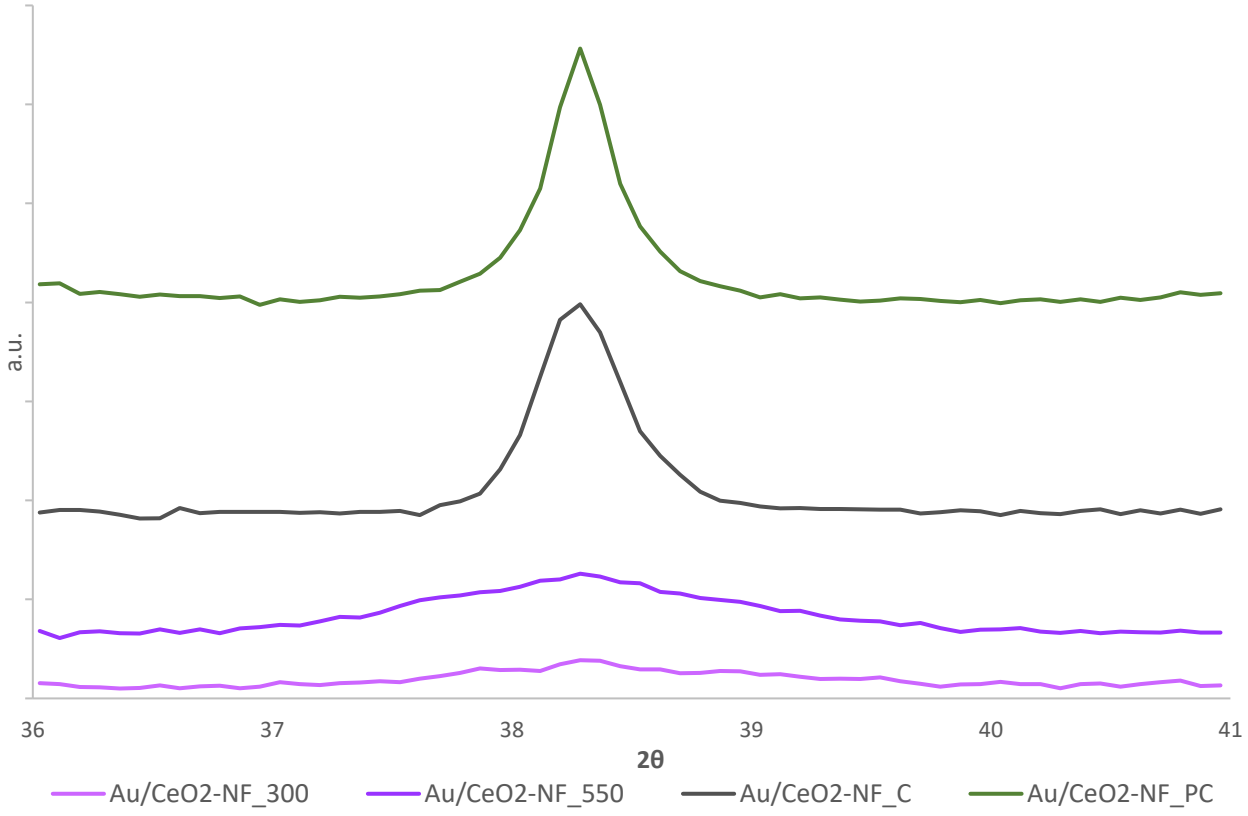

Figure 113: XRD of the peak (111) of the gold nanoparticles supported on the ceria catalyst samples

Catalyst	Average dimension of the gold crystallites (nm)	Preparation method
Au/CeO_2-NF_300	7	DP on cerium oxide nanofiber
Au/CeO_2-NF _550	8	DP on cerium oxide nanofiber
Au/CeO_2-NF _C	20	Calcination of nanofibers spun with $HAuCl_4$
Au/CeO_2-NF _PC	24	Heat treatment under N_2 flow and calcination of nanofibers spun with $HAuCl_4$

Table 25: Average dimension of the gold crystallites

The results of the catalytic tests using the catalysts in nanofibers on the oxidation reaction of HMF to FDCA have been compared in the following Figure 114.

Is possible to notice the strong dependence of the nanoparticle size on the final catalytic results, the sample Au/CeO_2-NF_300 have shown to be selective in the desired reaction, with good yields in the desired oxidation products and almost 0% of carbon loss. A similar pattern has been recorded for the sample Au/CeO_2-NF_550, the main difference in these two samples prepared via DP on the nanofibers is that the second gave a carbon loss of 13%, this lower selectivity has probably been caused by the greater size of its gold nanoparticles.

The two samples prepare via direct spinning of the fibres with $HAuCl_4$ showed similar performance, with high carbon losses and lower yields in the desired oxidation products.

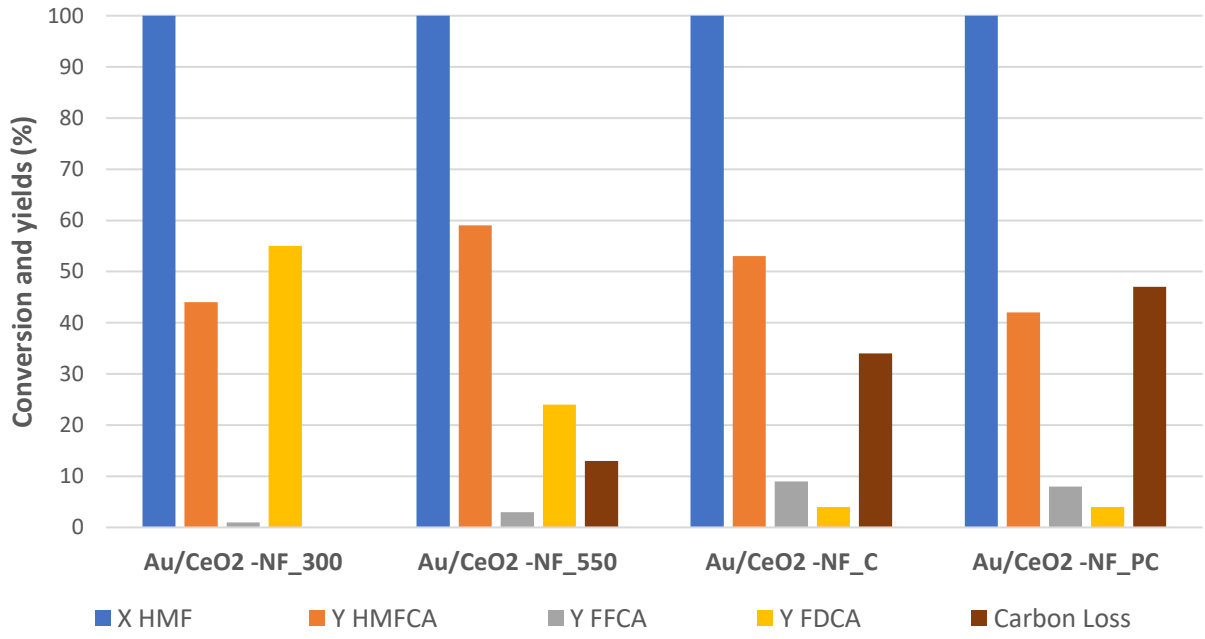

Figure 114: Catalytic test results of the HMF oxidation, reaction conditions: HMF: NaOH 1:4, t= 4h, T= 80°C

The electrospinning technique showed to be reliable in the production of 1D structure with possible application for catalysis purposes. The catalysts tested suggest that a wise preparation procedure could lead to good activity and selectivity in the desired reaction. The preparation method of the catalyst proved to influence the final morphology of the material, in particular, the crystallites dimensions and the surface area could be positively tuned during the production process. The removal of the soft templating agent used during the electrospinning, such as PVP, must be carefully studied to exploit the great influence on the final surface area of the material avoiding hot spots and possible undesired growing of the metal active phase during these operations, the nucleation and the crystal growth of the metal proved to be crucial for the preparation of good catalysts.